ANALYSIS AND VALIDATION OF THE FIELD COUPLED THROUGH AN APERTURE IN AN AVIONICS ENCLOSURE

By

RAHUL BAKORE

Bachelor of Engineering in Electronics and Communication
University of Rajasthan
Jaipur, Rajasthan, India
2008

Master of Science in Electrical Engineering
Oklahoma State University
Stillwater, OK
2012

Submitted to the Faculty of the
Graduate College of the
Oklahoma State University
in partial fulfillment of
the requirements for
the Degree of
DOCTOR OF PHILOSOPHY
May, 2017

ANALYSIS AND VALIDATION OF THE FIELD

COUPLED THROUGH AN APERTURE IN

AN AVIONICS ENCLOSURE

Dissertation Approved:

Dr. James C. West

Dissertation Adviser

Dr. Charles F. Bunting

Dr. George Scheets

Dr. Satya Nandi

ACKNOWLEDGEMENTS

I would like to dedicate this dissertation to my grandfather, Late Dr. G. V. Bakore, who was the First Professor and Head of the Chemistry Department at Mohanlal Sukhadia University, Udaipur, India.

Firstly, I would like to thank my Ph.D. advisor, Dr. James C. West, for his guidance and help throughout my Ph.D. degree program. Without his encouragement and support, this Ph.D. dissertation would not have been possible.

I would also like to thank Dr. Charles F. Bunting for being my committee member and for providing all valuable suggestions, guidance, help and support throughout my Ph.D. work.

My Sincere thanks to Dr. George Scheets and Dr. Satya Nandi for being my committee member and for providing feedback on my Ph.D. work.

I also thank Dr. Vignesh Rajamani, my labmates Neda Nourshamsi, Jacob Dixon, Dipen Das and Nick Oswald, Dr. Sovanlal Mukherjee, and Dr. Ponlakit Jariyatantiwait, for their help and support, especially Jacob and Neda for their help in my experimental work.

Last but not the least, I would like to thank my parents, Sudhir and Rupa Bakore, my elder brother, Dhananjay, and sister-in-law, Anushree, for their support and encouragement through this degree program.

This work was funded in part by the US Air Force Research Laboratory STTR Contract FA9451-15-M-0502, primary contractor ANDRO Computational Systems, LLC.

Name: RAHUL BAKORE

Date of Degree: MAY, 2017

Title of Study: ANALYSIS AND VALIDATION OF THE FIELD COUPLED THROUGH AN APERTURE IN AN AVIONICS ENCLOSURE

Major Field: ELECTRICAL ENGINEERING

Abstract: This work focused on accurately predicting the current response of an equipment under test (EUT) to a random electromagnetic field representing a threat source to model radio frequency directed energy weapons (RFDEWs). The modeled EUT consists of a single wire attached to the interior wall of a shielding enclosure that includes an aperture on one face. An in-house computational electromagnetic (CEM) code based on method of moments (MOM) and accelerated by the multi-level fast multipole algorithm (MLFMA), was enhanced through the implementation of first order vector basis functions that approximates the EUT surface current. The electric field integral equation (EFIE) is solved using MOM/MLFMA. Use of first-order basis functions gives a large savings in computational time over the previous implementation with zero-order Rao-Wilton-Glisson basis functions. A sample EUT was fabricated and tested within an anechoic chamber and a reverberation chamber over a wide frequency band. In the anechoic chamber measurements, the current response on the wire within the EUT due to a single uniform plane wave was found and compared with the numerical simulations. In the reverberation chamber measurements, the mean current magnitude excited on the wire within the EUT by a mechanically stirred random field was measured and compared with the numerical simulations. The measured scattering parameter between the source antenna and the EUT measurement port was used to derive the current response on the wire in both chambers. The numerically simulated currents agree very well with the measurements in both the anechoic and reverberation chambers over the measured frequency band, confirming the validity of the numerical approach for calculating EUT response due to a random field.

An artificial neural network (ANN) was trained that can rapidly provide the mean induced current response of an EUT due to a random field under different aperture configurations arbitrarily placed on one face of an EUT. However, ANN proved no better than simple linear interpolation in approximating the induced currents on EUTs that give strong resonances and nulls in the response.

TABLE OF CONTENTS

LIST OF TABLES

LIST OF FIGURES

Figure Page

CHAPTER 1

INTRODUCTION

Over the past few decades the use of electronics in aviation has increased at a staggering rate. Although this has led to significant increases in aircraft stability and safety, it has also made aircraft susceptible to radio frequency directed energy weapons (RFDEWs). RFDEWs are a growing concern for the survivability of an aircraft. This weapon system generates high power electromagnetic radiation which can destroy or disable the electronic devices and navigation systems inside the aircraft.

For these reasons, electronic devices are enclosed in metallic enclosures for protection against the electromagnetic interference (EMI) from the threat source. These metallic enclosures must have apertures on at least one wall for ventilation and interconnecting cabling, compromising the shielding effectiveness of the metallic enclosure. Such high external electromagnetic fields coupled into the electronic devices through the aperture can induce excessive current on the interconnecting cables and the devices inside the enclosure. When the induced current in electronic device exceeds its threshold current level, that device could be damaged or fail to work.

In order to predict the harmful effects on the aircraft due to RFDEWs, the U.S. Army Research Laboratory and U.S. Air Force Philips Laboratory jointly developed the Directed RF Energy Assessment Model (DREAM) software package [1] [2] in 1995 for estimating the failure of critical electronic components within targets. DREAM relies on certain user inputs such as transmission loss which must be provided manually. This severely limits the application of the tool in predicting failures.

Significant advancement has been made in computational electromagnetic (CEM) techniques over the last 20 years, which performs large-scale simulation for modeling such real-world problems. Hence a calculated failure prediction using this numerical technique, which unlike DREAM does not depend on arbitrary transmission loss, will be more accurate than the DREAM tool.

This research builds upon the work done in [3]. An in-house CEM code developed in REFTAS laboratory at Oklahoma State University, USA, was used in [3] for modeling the effects of external electromagnetic fields within a modeled avionics compartment. The primary goal of this research is to improve DREAM by accurately predicting the distribution of the threat-source electromagnetic field within a modeled enclosure when coupled through an aperture, as required for the failure predictions. This goal was approached by enhancing the in-house CEM code to perform accurate calculations in reduced computational time. Measurements were then performed in on-site electromagnetic anechoic and reverberation chambers to validate the CEM code simulation results. Finally, an artificial neural network (ANN) was trained to completely remove the need of repeating the CEM code simulations under different configurations and positions of an aperture on one of its wall of the enclosure and at changing excitation frequencies.

1.1. Directed RF Energy Assessment Model (DREAM)

1.1.1. Overview of DREAM

DREAM [1] [2] is a graphical user-interface software tool for describing the effects of EMI on mobile targets like aircraft. This tool does not require geometrical details of the target and RFDEWs. The probability of failure of the critical component in a subsystem is computed as a function of power density at the target (or the distance between the target and RFDEWs). Typically, the critical component is an electronic component (mixer, linear IC, operational amplifier, diode, etc.). The port of entry could be seams, cracks or any opening in the aircraft system that allows RF energy from the threat source to enter. The RF energy from the threat source is coupled into the port of entry and finds its way to expose the critical component resulting in failure of the component as shown in Figure 1.1.

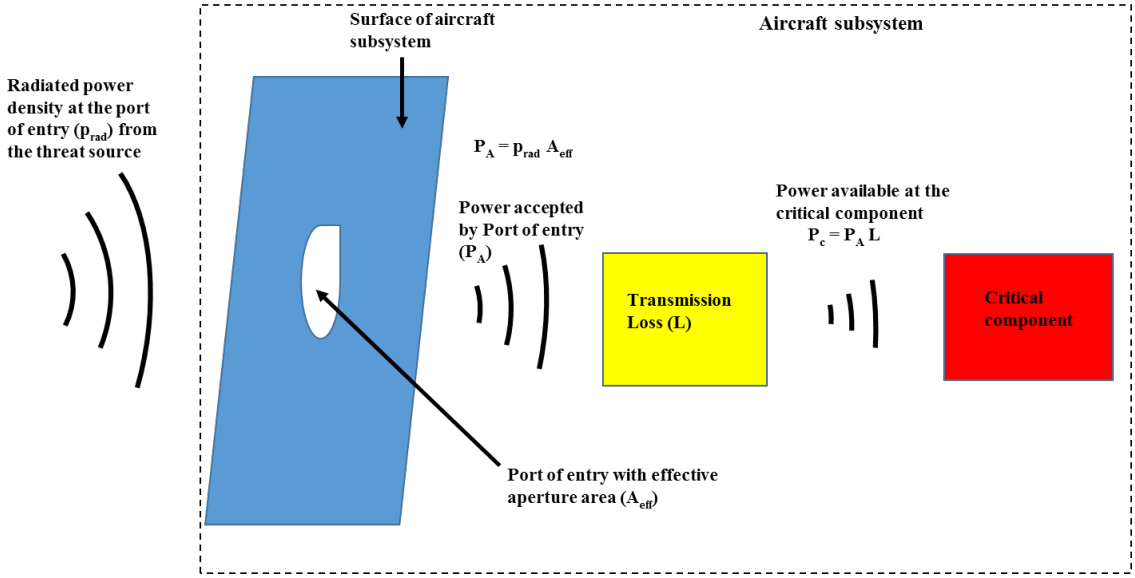

Figure 1.1. Power available at the critical component from the threat source

The power available at the critical component is calculated in DREAM using Friis transmission equation, given by [4]

$$P_d = \frac{P_s G_s}{4\pi r^2} A_e L = P_A L\,, \tag{1.1}$$

where P_s is source power, G_s is source antenna gain, r is the range between the source and the target, A_e is the effective aperture area of the subsystem, P_A is the power coupled through the aperture due to source power P_s, and L is the transmission loss between the port of entry and the critical component. DREAM generates a cumulative distribution function (CDF) that represents a statistical distribution of effective aperture area, formed under the assumption of an electromagnetic field that is randomly coupled over a uniformly distributed angle of incidence, from the threat source. When the power at the critical component exceeds its threshold power level, that component could be damaged or stop working, resulting in the failure of the aircraft subsystem.

1.1.2. Limitation of DREAM

As discussed, DREAM uses Frii's transmission equation for determining the power at critical components due to a threat source. The power available at the critical component depends on the transmission loss. However, the transmission loss has to be given as a user input, rather than being calculated directly, in DREAM. Incomplete knowledge of the transmission loss poses a severe limitation in predicting the failure of the critical component. Susceptibility of the critical component calculated by DREAM is strongly dependent on this parameter [1].

Considerable work performed in the past by various researchers has been focused on estimating the shielding effectiveness (SE) of a rectangular enclosure containing one or more apertures. The SE at the calculation or measurement point within the enclosure is defined as the ratio of field strength at the measurement point in the absence of the enclosure to the field strength at the same location in the presence of the enclosure. As noted, this parameter is strongly related to the transmission loss parameter in DREAM. Hence, a detailed discussion of the work performed in calculating SE is given in Chapter 2. Additionally, the relationship between the transmission loss and the SE is also given.

1.2. Methodology for improving DREAM

The calculation of failure prediction in DREAM can be improved by a combination of a computational electromagnetic approach and measurement within an electromagnetic reverberation chamber, as discussed below.

1.2.1. Computational electromagnetic (CEM) technique

Computational electromagnetics (CEM) has advanced considerably over past few decades, fully utilizing improvements in computer speed and storage to solve complex problems, as well as implementing new algorithms that accelerate the solution. These numerical techniques have the advantage of numerically modeling a complex structure that include all geometrical details. CEM techniques based on the method of moments (MOM) [5] [6] discretize the computational domain into several small subdomains. Maxwell's equations are solved in each subdomain. The CEM technique uses basis functions, known polynomial functions, for representing the induced current on the structure subdomains. The induced current or the power available at the critical component, due to an external electromagnetic field, can be directly calculated using this technique, without having any dependencies on arbitrary transmission loss. Thus, the limitations of the DREAM tool can be overcome.

The challenges in numerically modeling such problems is that this technique requires exact details of an electronic equipment such as its enclosure shape and size, location of the wire, and other geometrical details as suggested by Olyslager [7], which are not known due to the manufacturing tolerances or arbitrary placement of equipment. Small changes in any of these parameters can create different electromagnetic environments within the enclosure. Therefore, a statistical representation of coupled electromagnetic field is required. The electromagnetic field distribution obtained within the enclosure can be analyzed as a random variable due to the changes in the above parameters. Therefore, the detailed geometrical information has been ignored and the focus is on a single wire attached to the interior wall of the cavity, considered as an equipment under test (EUT).

1.2.2. Statistical field by reverberation chamber technique

The critical system component or electronic device is operated in a complex and overmoded cavity environment. A cavity is considered as overmoded at a given frequency when the number of existing cavity modes are greater than 60 [8]. A cockpit of an aircraft is typically sufficiently overmoded above approximately 400 MHz [9]. For creating the statistical electromagnetic environment within such complex and overmoded cavity, measurement in reverberation chambers has been widely used. Freyer *et al.* [9] [10] showed that the statistical distribution of the electromagnetic environment operating at 1 GHz in an aircraft cavity (avionics bay, aircraft cockpit or aircraft cabin) are similar to that in a reverberation chamber. Bunting *et al.* [11] [12] suggested that testing within a reverberation chamber may provide a deep intuitive understanding of the shielding effectiveness of an EUT through a statistical analysis. A reverberation chamber is a large metallic cavity resonating with a higher quality factor. It consists of a transmitting antenna, EUT, and tuner, as shown in Figure 1.2. A large number of cavity modes inside the chamber are excited by the power transmitted into a chamber (P_t) from the transmitting antenna.

The quality factor of an aircraft cavity may range from 10 to 1000 due to absorbing material and apertures whereas a low loss reverberation chamber quality factor ranges from 10,000 to 200,000 [9]. Rajamani *et al.* [13] measured the quality factor of the unloaded SMART^{TM} 80 reverberation chamber using frequency domain and time domain measurement techniques. For 1 GHz centered frequency band with 200 MHz bandwidth, the quality factor was measured as 44.63 dB (29,040) and 45.44 dB (34,994) using frequency domain and one-port time domain techniques, respectively. Holloway *et al.* [14] suggested that such discrepancies in measured results are due to the antenna mismatch efficiency which was not taken into an account while performing the measurement in the the frequency domain.

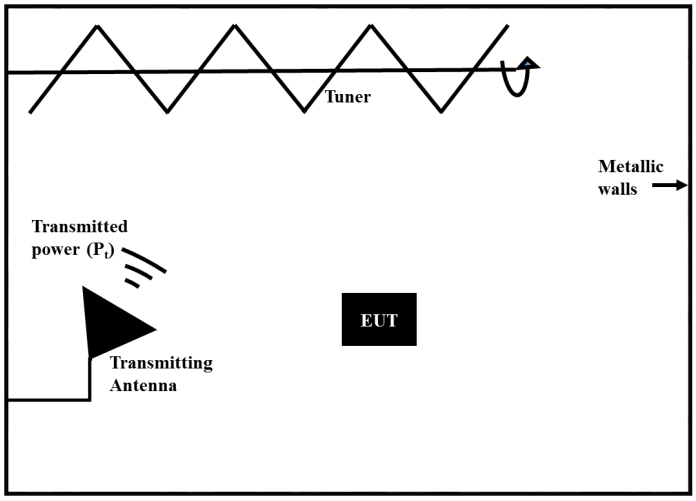

Figure 1.2. Reverberation chamber technique for susceptibility testing of EUT

The statistical field distribution inside the reverberation chamber can be obtained by changing the boundary condition of the electromagnetic fields inside the chamber. Mechanical stirring is one of the options to obtain such statistical distribution. A tuner is an electrically large conducting structure that occupies a considerable portion of the cavity volume. The boundary conditions are modified by changing the position of tuner using a stepper motor. For an ideally stirred chamber, the field distribution inside the chamber is statistically uniform and randomly polarized [15] [16]. Hill [15] showed that the magnitude of the current induced on the test object due to an ideally random, mechanically stirred reverberation chamber field follows the Rayleigh distribution. The response on the EUT due to the transmitting antenna can be obtained for each tuner position. Therefore, a failure prediction of critical component (or electronic equipment) can be made based on the ensemble average of the response of EUT calculated over all the tuner position.

Numerically modeling an entire reverberation chamber to simulate the random field within a chamber is computationally expensive. Hill [15] shows that such a random field can be represented by a superposition of plane waves, with random phase and polarization, propagating from the far field. Using a CEM technique, such plane waves can be modeled as a field source, eliminating the need to model

the chamber walls and tuner structure. Only the EUT needs to be modeled. This random field can be represented by the integration of a continuous spectrum of uniform plane waves [15]. Musso *et al.* [17] approximate this integration by considering a finite number of random plane waves (as low as 20). The random field was then obtained by a superposition of a finite number of plane waves with unity magnitude and randomly determined propagation direction, polarization and phase. Moglie *et al.* [18] shows that the field statistics within the chamber can be improved by increasing the number of plane waves. Numerical simulation using finite difference time domain (FDTD) was performed with 100 plane waves in [18] to calculate the response of EUT within the chamber. Each simulation was repeated 200 times (analyzed as 200 positions of the tuner) to acquire a set of 200 randomly generated field at any point within the chamber. However, this gives a total number of 20,000 simulations that must be performed, and hence gives a large computational time.

West *et al*. [19] shows an alternate technique for discretizing the integration of the continuous plane wave spectrum by using fixed directions of plane waves rigorously determined by Legendre/uniform sampling over the sphere. Two orthogonally polarized plane waves were considered for each propagation direction. The statistical properties were then achieved by assigning unique, randomly generated complex number to the coefficient of each plane wave. As fixed plane wave directions were used, the response of EUT due to two plane waves at each propagation direction need only be found once. Hence, the simulation need not be repeated for each plane wave to obtain the distribution of a randomly generated field at any point within the chamber, giving a large saving in computational time compared to the approach used by Musso *et al.* [17] and Moglie *et al.* [18]. By exploiting the principle of reciprocity [20], the simulation needs to be run only one time, hence considerably reduces the computational time.

1.3. Advantage of susceptibility testing in a reverberation chamber over anechoic chamber

The anechoic chamber was also considered to perform susceptibility testing of the EUT by Rajamani *et al.* [21], Freyer *et al.* [22] and Gradoni *et al*. [23]. An anechoic chamber is a room with its wall covered with absorbing material to minimize the reflection of electromagnetic waves. Hence, the EUT receives electromagnetic waves only from the transmitting antenna. The transmitting antenna was placed in the far field region of the EUT so that a uniform plane wave is incident on the face of the EUT containing the aperture. However, only a limited number of plane wave aspect angles can be used for susceptibility testing in an anechoic chamber. According to Rajamani *et al.* [21] and Freyer *et al.* [22], the susceptibility (or emission) testing of EUT in an anechoic chamber is typically performed with four plane-wave aspect angles, each with two polarizations. Gradoni *et al.* [23] used plane-wave directions, normal and parallel to the face containing the aperture, each with one polarization. So, the electromagnetic environment obtained, due to a limited number of aspect angles, is not expected to approach a random field. Hence, susceptibility testing in an anechoic chamber is less rigorous than that in a reverberation chamber.

1.4. Literature survey

A numerical simulation of EUT response due to a random field within an ideally stirred reverberation chamber was first performed at REFTAS laboratory by Assefa *et al.* [20]. The numerical simulation was performed using the in-house CEM code over the frequency range from 300 MHz to 8.5 GHz. The discrete plane-wave spectral model given by West *et al.* [19] was used to represent the random field reverberation chamber field. The EUT considered was a wire attached to the floor of a cavity that has a large aperture on one of its face. The current induced at the base of the wire due to a random field was considered as the response of EUT. A reciprocal approach was used to calculate the current induced on the wire; hence the numerical simulation was run only one time at each frequency. Statistical testing using the Anderson-Darling goodness-of-fit test [24] showed that the numerically simulated current

induced on the wire follows the Rayleigh distribution, as expected in an ideally stirred reverberation chamber. However, the measurement within the reverberation chamber was not performed in Assefa's work [20] to validate the numerically simulated current induced on the wire.

Measurements within an anechoic chamber was performed by Rajamani *et al.* [3] to validate the in-house CEM code simulated results. The electromagnetic illumination was limited to a single uniform plane wave normally incident on the aperture face over a frequency range from 300 MHz to 8.5 GHz. The wire probe was also limited to one position. Overall good agreement was achieved, but some differences were observed between the measurement and the in-house CEM code predictions. Rajamani *et al.* [3] suggested that an aperture resonance might contribute to some of the observed differences as the measurement was performed with a cavity having a finite wall thickness while the cavity wall was modeled as ideally thin in the computations. An additional concern was differences in the connection of the wire to the cavity wall. In the simulation, the wire was directly connected to the cavity wall while in reality it was connected through an SMA connector.

The authors in [3], as experienced researchers, viewed the comparison between the measurement and numerical simulation using in-house code as very good over most of the frequency range while acknowledging the amplitude differences from 3.5 GHz to 4.5 GHz. The conclusion made by the authors are based on their knowledge and experience with the measurement approach and the inherent geometrical differences between the fabricated prototype and an ideal numerical simulation model. However, an engineer or researcher unexperienced in this field or a third party may come to a different conclusion based on their personal experience when viewing such a comparison [25]. Feature Selective Validation (FSV) [25] [26] is a candidate validation tool that has been incorporated into the IEEE 1597.1 and 1597.2 standards [27] for use in validating computational electromagnetic (CEM) simulation. Therefore, an analysis using FSV that confirms the validity of the CEM results against measurement is desirable.

As discussed before, the electromagnetic environment generated within the cavity is highly sensitive to changes in the cavity or EUT geometry. It is also sensitive to changes in the excitation frequency of the cavity [16]. Hence, accurate prediction of responses on a critical component (or on the cables) is required within a highly resonant cavity environment. The accuracy of the numerical simulation technique is limited by the interpolation (basis) function used for approximating the induced current on the metallic surfaces. The in-house CEM code in [3] [20] discretizes the cavity walls into a triangular patches and used RWG vector basis functions [28], represented by the lowest order polynomial function (linear) [29] [30], to model the surface current for each triangular patch. The electric field integral equation (EFIE) was used to find the surface current. Fine discretization of the walls was used to capture the sharp resonances over a frequency range from 300 MHz to 8.5 GHz. The dimension of the triangular patches used in [3] was 0.075λ where λ is the wavelength in a free space. At higher frequencies, the simulation is computationally expensive due to a large number of triangular patches generated on the cavity walls and hence requiring a large number of unknowns to solve for the surface currents. Therefore, use of vector basis functions represented by higher order polynomial function [29] [30] is required to achieve the desired accuracy with less computational effort.

1.5. Dissertation objective

The objective of this dissertation is to accurately predict the current response on internal EUT wires due to the random electromagnetic field coupled through an aperture in the EUT enclosure. This objective can be approached by first enhancing an in-house CEM code for more efficient calculation. Then, the statistical response of EUT can be calculated due to a random field inside the chamber using the enhanced in-house code. The EUT considered in this work is derived from the earlier work in [3] [20]. Various aperture configurations and wire positions are also considered. The induced current at the attachment point between the wire and cavity wall is calculated to represent the response of EUT. The next section gives the overview of the steps performed to achieve this goal.

1.6. Steps for predicting the response of equipment under test (EUT)

The following steps were performed in this dissertation to predict the EUT response due to a random field within a reverberation chamber:

1.6.1. Validation of CEM results

FSV analysis has been performed between the measured and simulated results using the in-house CEM code (approximated with RWG basis function) presented in [3] to examine how closely its comparison matches the views of experienced researchers. Another numerical simulation tool, the commercially available CONCEPT II package [31], has also been used to numerically model the same problem, again keeping the cavity walls as ideally thin and the wire directly connected to the cavity walls as before. An FSV analysis was performed between the in-house code and the CONCEPT II results, with variability introduced in the positioning of current probe and the meshing itself of the numerically modeled cavity. Finally, an FSV analysis is performed again using the same current probe locations in both simulation tools, but still allowing differences in the mesh model of the problem.

1.6.2. Enhancement of in-house CEM code

The in-house CEM code has been enhanced by implementing higher order vector basis function of linear normal / quadratic tangent (LN/QT) variety [29] [32]. Such higher order basis function gives a smoother representation of surface current, resulting in better accuracy for the same mesh.

1.6.3. Measurement in the anechoic chamber

The validity of the enhanced in-house code calculations needs to be verified through comparison with the measurement before using it to model the response of EUT inside the reverberation chamber. The test case considered here is to expose the EUT to a single uniform plane wave normally incident on the face containing the aperture. The induced current is calculated at the attachment point between the wire and cavity wall. To confirm whether aperture resonance was responsible for the discrepancies between

the measured and simulated currents in the frequency range from 3.5 GHz to 4.5 GHz in [3], aperture face in EUT is replaced by its thinner aluminum thickness. The anechoic chamber is then used to perform the measurement of that induced current with modified EUT.

1.6.4. Numerical modeling and measurement of EUT within reverberation chamber

After validating the enhanced in- house CEM code results against the measurement in the anechoic chamber, the enhanced in-house code can be used for numerically calculating the response of EUT due to a random field within a reverberation chamber. Such a random field can be represented by the superposition of plane waves with random phase, as discussed in Section 1.2.2. Hence the response on EUT due to a random field can be obtained by the superposition of its responses due to each plane wave found by solving the electric field integral equation (EFIE) using the method of moments (MOM). A measurement of the response of the EUT to a random field was performed in the SMART^{TM} 80 reverberation chamber, located at the facility of Oklahoma State University, USA, to validate the numerical simulation results.

1.6.5. Neural network approach of estimating EUT response

Once the validity of numerical simulations has been confirmed against the measurement within the reverberation chamber, the numerical simulation tool can be used to accurately predict the EUT response of a random field for any specific set of geometrical parameters such as aperture shape, size, wire position, etc. However, there is a need to predict the sharp resonant peaks in the EUT response which cause failure in electronic devices. The magnitude and the frequencies of these sharp resonant peaks are often changed when the EUT geometry is slightly modified. Hence, changes in various geometrical parameters must be considered. Repeating the numerical simulations for any arbitrary combination of geometrical parameters that may be encountered is computationally expensive. Hence, there is a need to model the transfer function that gives a relationship between the geometrical parameters of the EUT as inputs and the EUT response as the output. Therefore, the use of artificial

neural network (ANN) was considered in this dissertation to model such a transfer function. An ANN is a system which is trained to model the response of the EUT under various geometrical parameter by providing it with a fixed set of input and output data. ANN modeling could therefore potentially detect the sharp resonances and nulls in the EUT responses due to its ability of recognizing patterns in the output parameters for various input parameters. Thus, once the ANN is trained, the EUT response for any geometrical parameters can be predicted nearly instantly, and thus serving as an alternative to direct numerical simulation.

1.7. Dissertation organization

This dissertation is organized into seven chapters. Chapter 2 gives an overview of the work done by various researchers in evaluating the shielding effectiveness of a rectangular cavity with apertures. The limitations of their work are also discussed. As both the in-house and CONCEPT II CEM codes are based on the method of moments (MOM), Chapter 2 also gives an overview of MOM and its implementation for solving the EFIE. Chapter 3 discusses an FSV analysis of the agreement between the measured and the simulated current responses of an EUT including a highly resonant cavity environment. FSV was then used to assess the agreement between the currents predicted by the in-house and CONCEPT-II numerical approaches.

A demonstration of the use of LN/QT basis functions in moment-method calculations is given in Chapter 4. The following test cases are considered to demonstrate the performance of LN/QT basis function over the RWG basis function in terms of both accuracy and computational time:

a) The induced current distribution on a perfectly conducting square plate [28] [29] [33] due to a normal incident uniform plane wave is calculated. The radar cross section of this plate as a function of illumination incident angle is also calculated.
b) The radar cross section of a perfectly conducting cube as a function of uniform plane wave incident angle is computed.

c) This test case considers a wire attached to the floor of a cavity that has a large aperture on one of its faces, same as was considered in [3]. A single uniform plane wave is normally incident on the cavity face that includes the aperture. The induced current is calculated at a point on the wire very close to the attachment point of the wire and the cavity wall over a frequency range from 300 MHz to 1 GHz.

In Chapter 5, the measured and simulated EUT responses when the EUT was illuminated by a single uniform plane wave normally incident on the aperture face are presented. The EUT in this case has an aperture face made of thinner aluminum than was used in [3]. The numerical calculations are validated against measurements performed in an anechoic chamber. Three different wire positions with the EUT are considered. An FSV analysis was performed to assess the agreement of the measured and simulated currents for each wire position.

After validating, the response of the same EUT to a random field within a reverberation chamber is considered in Chapter 6. The discrete spectrum of plane wave model of [19] is used to represent the random chamber field. This chapter also introduces a method to extract the EUT current response from the scattering parameter between the transmitting antenna and the EUT measurement port (S_{21}) measured using a vector network analyzer, the chamber quality factor, and transmitting antenna's free space reflection coefficient, allowing a direct comparison with the simulations. The three different wire positions used in Chapter 5 are again considered. An FSV analysis is again performed assess the agreement between measurements and simulation for each wire positions.

In Chapter 7, an ANN is trained to calculate the EUT response to a random field at three different wire positions when differently shaped apertures are arbitrarily placed on the EUT front face. Training datasets are obtained by using the enhanced in-house CEM code to calculate the EUT response for different aperture shapes, areas, and positions, and for different wire positions. The ANN and numerical

simulation results are then compared at aperture positions that were not used in training. Once the ANN results are validated, the ANN is then used to study the dependence of the EUT response on the aperture position, shape, and area. Linear interpolation method is also used to calculate the response of the EUT. Finally, the performance of the ANN is compared with that obtained by linear interpolation. A summary of the work and a discussion of potential direction for future work are given in Chapter 8.

CHAPTER 2

BACKGROUND

As discussed in Chapter 1, DREAM relies on a transmission loss parameter that must be given as a user input, rather than being calculated directly. Incomplete knowledge of the transmission loss poses a severe limitation in predicting the failure of electronic devices operating within an enclosure. It was also noted that this parameter is strongly related to the shielding effectiveness (SE) of the enclosure. Considerable work has been performed by various researchers to determine the SE of a rectangular enclosure containing one or more apertures. In this chapter, a review of their work, including techniques to determine the SE of a rectangular enclosure, their limitations, and relation to the transmission loss parameter, is given. Also, the in-house CEM code and CONCEPT II numerical simulation tools are directly based on the method of moments (MOM) technique. Hence, an overview of MOM is also included in this chapter.

2.1. Relationship between transmission loss and shielding effectiveness

The electric shielding effectiveness at test point q within an enclosure is given by

$$SE_q = \frac{\left|E_q^{\,inc}\right|}{\left|E_q^{\,total}\right|}, \tag{2.1a}$$

$$SE_q(\text{in dB}) = 20\times\log_{10}\left(\frac{\left|E_q^{\,inc}\right|}{\left|E_q^{\,total}\right|}\right), \tag{2.1b}$$

where E_q^{total} is the total electric field computed at the test point q within the enclosure, and E_q^{inc} is the incident electric field computed at the same location in the absence of the enclosure. The transmission loss at test point q in DREAM can be written using equation (1.1) as

$$L_q = \frac{P_q}{P_A}, \tag{2.2}$$

where P_q is the power coupled at the test point q within the enclosure and P_A is the power coupled at the aperture of the enclosure due to an external electromagnetic field. As, $P_q \propto \left|E_q^{total}\right|^2$ and $P_A \propto \left|E_q^{inc}\right|^2$, from equation (2.1) and (2.2),

$$L_q \propto \frac{1}{SE_q{}^2}. \tag{2.3}$$

Hence, the greater the shielding effectiveness, the lower the transmission loss at a given test point and the lower the strength of the field penetrating the aperture into the cavity.

2.2. Literature survey in shielding effectiveness

2.2.1. Analytical method

Following are the analytical techniques used for predicting the shielding effectiveness (SE) of a rectangular enclosure with apertures.

2.2.1.1. Transmission line approach

Robinson *et al.* [34] developed an analytical formulation of calculating SE of a rectangular enclosure with an aperture. In this work, the enclosure was taken as a rectangular waveguide short-circuited on one end and the aperture modeled as a length of coplanar-strip transmission line shorted at both ends. Transmission line theory was then applied to calculate the current and voltage at a given point, giving the electric and magnetic SE at that point. The electric and magnetic shielding was defined as a function of aperture dimensions, enclosure dimensions, and the excitation frequency. However, this formulation is restricted to an empty rectangular cavity with a narrow

aperture, and the SE can be calculated only at a point in front of the aperture. Only a single mode of propagation (TE_{10}) in a waveguide was considered in this work, which limits the accuracy of the solution to lower frequencies or electrically small enclosures dimension where the TE_{10} mode is dominant within the cavity.

2.2.1.2. Power balance approach

Hill [35] developed a power-balance approach for calculating the shielding effectiveness of a cavity with an aperture and loading. The SE of a cavity was derived by matching the transmitted power into a cavity through an aperture with the total power dissipated within the cavity. The total power dissipated is the sum of the power dissipated due to loading, cavity wall losses, aperture leakage, and antenna power loss. The power dissipation due to each loss mechanism was discussed in detail. The SE can be calculated for an arbitrary angle of plane wave incidence. Measurement within a reverberation chamber was also performed to validate the results of this analytical technique. However, this approach is limited to a circular shape aperture. Thus, it is not valid for long and narrow apertures which have strong resonances. Moreover, an approximately 20 dB difference between the measured and power-balance SE is observed near the frequencies where the cavity dimension is not electrically large. Hill [35] suggests that additional cavity losses must be included in the theoretical analysis to compensate the differences between it and the measurements.

2.2.2. Challenges in numerically modeling a rectangular enclosure

Moerloose [36] reviewed the challenges of using the finite difference time domain (FDTD) [6] and method of moments (MOM) [5] [6] numerical methods for calculating SE of a metallic enclosure. A uniform plane wave incident normally on the face of the enclosure containing the aperture was used as the source of excitation. The SE was calculated at the center of the enclosure. The shielding effectiveness given by FDTD and MOM was validated by measurements in a semi-anechoic chamber. The uniform plane wave illumination in the measurement was obtained by a vertically

polarized antenna which was placed 3 m from the aperture face of the shielded enclosure. The numerically simulated SE found using both FDTD and MOM agreed with the measured SE to within 5 dB below the first resonance of the enclosure cavity. However, both simulation methods suffered from high computational cost. With MOM, a very dense surface mesh was required near the electromagnetically narrow aperture to accurately calculate the weak internal fields within the enclosure, leading to a large interaction matrix that must be filled and solved. Similarly, the time-domain FDTD required a large computational time to prevent undesirable late-time oscillations resulting from resonances in the shielded enclosure.

Olyslager [7] also performed a numerical study of the SE of a rectangular enclosure. The radiating source was located inside the enclosure and SE was obtained by calculating the field outside the enclosure at a distance of 3 m from the aperture face. Due to reciprocity, this problem is equivalent to calculating the SE at the location of the radiating source, when the enclosure is illuminated by a uniform plane wave normally incident on the aperture face. The SE was calculated for various test-configuration aspects such as the number of apertures, position of the radiating source, and the presence of metal plates and absorbing materials. Olyslager [7] suggests that detailed information about the geometry of the enclosure such as the position of a radiating source and large internal metal objects within the enclosure are required to accurately characterized the SE. Olyslager [7] further suggests that a simple design rule for estimating shielding effectiveness is virtually impossible due to the extreme complexity of test equipment and the large computational resources needed to perform the calculations.

2.2.3. Statistical study of aperture shielding effectiveness within the 2-D reverberation chamber

Bunting *et al*. [11] simulated a 2-D reverberation chamber using the finite element method (FEM) [6]. The field distribution within a chamber was calculated at a frequency that supported either

transverse electric (TE) and transverse magnetic (TM) resonant modes. An aperture was placed in a wall divided the chamber into two regions, a source region and a shielded region. The source region included a mode-stirring tuner and an excitation source, and the shielded region was empty. The numerical simulation found the field distribution in both regions. 225 different tuner positions were used to estimate the statistics of the field within the shielded region chamber. For the TE case, the statistics of the field were constant over 100 random positions within a source and a shielded region, as expected in an over-moded reverberation chamber. In [11], the maximum field level at a particular position within a chamber is represented by the maximum field magnitude over all tuner positions. Then, the shielding effectiveness (SE) at j^{th} position within a shielded region is defined as the ratio of the maximum of the maximum field levels obtained at 100 random positions in source region to the maximum field level calculated at j^{th} position in shielded region. Some of the positions showed a negative SE in dB which indicates that the field magnitude is actually greater in the shielded region than in source region. For the TM case, the field statistics in the two regions were similar, but did not match that expected in a reverberation chamber. Bunting *et al.* [11] showed that the field followed the Johnson SU distribution, and is consistent with the Hill's results [37] when the operational frequency is too low to give over-moded operation. Bunting *et al.* [11] suggested that testing within a reverberation chamber environment may provide a deep intuitive understanding of shielding effectiveness through a statistical analysis.

2.2.4. Analysis using Modal MOM

Another statistical analysis of the SE of a rectangular enclosure was presented by Bunting *et al*. [12]. The statistical distribution within the box was obtained by varying the source frequency of a single uniform plane wave, giving a frequency-stirred reverberation chamber field. The modal method-of-moments (modal-MOM) [38] technique was used to find the field distribution within a rectangular enclosure that included rectangular apertures. In this technique, each aperture is represented by an equivalent magnetic current. Then, the fields outside the enclosure (the external

fields) are found using the free space Green's function with the magnetic current as the radiating source. Similarly, the fields within an enclosure (internal fields) are found using the cavity Green's functions. The internal and external fields are matched at the aperture face, giving an integro-differential equation to be solved for the unknown magnetic currents using the method of moments. Only a single component of electric field within the enclosure was used for evaluating SE. The SE was shown to be normally distributed at a single point within the enclosure when varying the source frequency from 4 GHz to 5 GHz. The statistics of the field were constant over 100 random points within a test region of the enclosure, thus showing characteristics similar to an over-moded, mechanically stirred reverberation chamber.

The Modal MOM used in [12] was only applicable for a vertically polarized uniform plane wave normally incident on the aperture face as the excitation source. Khan [39] improved the Modal MOM technique by incorporating an obliquely incident uniform plane wave of arbitrary polarization as the excitation source. A normally incident plane wave is usually used to determine the SE, under the assumption that this excitation gives maximum field coupling. However, Khan [39] showed that maximum field coupling into the enclosure is not always maximized with normal incidence when multiple apertures are present. It was suggested that the interaction between the radiation patterns of different apertures may lead to larger enhancement of field with an obliquely incident plane wave.

The advantage of Modal MOM technique is that it allows more than one aperture on both the front and rear faces of the rectangular enclosure. Another advantage is that the computational time is smaller than other numerical techniques such as FDTD, MOM, and FEM. However, this method is only applicable for a lossless empty cavity and rectangular shaped apertures that are small compared to the wall size. Moreover, Modal MOM assumes no diffraction of fields at the cavity edges. Hence, the equivalent magnetic current in the aperture is radiated in an infinite ground plane.

Rajamani *et al.* [40] showed that this technique cannot predict the SE for plane-wave excitation at large angles of incidence.

2.2.5. Field coupling through various aperture shapes

Siah *et al.* [41] used MOM accelerated by the multi-level fast multipole method (MLFMM) to determine the SE of an enclosure. Single apertures with various shapes such as rectangle, square and circle on one face of the rectangular enclosure were considered. They found that square and circular shape apertures give better shielding performance than rectangular apertures of similar area at lower frequencies. Siah *et al.* [41] suggested that the higher SE at lower frequencies may be due a shifting of aperture resonances from lower to higher frequencies when a rectangular aperture is replaced by square or circular aperture. They also showed that similar shielding performance can be achieved with either a circular or a square aperture of the same area.

2.3. Overview of method of moments (MOM)

The method of moments (MOM) is one of the oldest computational electromagnetic methods used to solve radiation and scattering problems. This technique converts an integral equation derived from Maxwell's equations in the frequency domain into a linear system that can be numerically solved. The Sommerfeld radiation boundary condition [5] is used, so an open region problem can be solved. Thus, it does not require discretizing the medium surrounded by the cavity; only the surface of cavity walls and any wires within or attached to the enclosure must be discretized. This section gives a brief overview of solving the electric field integral equation (EFIE) using MOM.

2.3.1. EFIE formulation

The electric field integral equation (EFIE) matches the tangential component of the incident electric field on conducting boundary surfaces. It can be written as [5]

$$\mathbf{E}^{i}_{tan}(\mathbf{r}) = j\omega\mathbf{A}(\mathbf{r}) + \nabla\Phi_e(\mathbf{r})|_{tan}\,, \tag{2.4}$$

where $\mathbf{E}^{i}_{tan}(\mathbf{r})$ is the tangential component of the incident electric field at the conducting surface and $\mathbf{A}(\mathbf{r})$ and $\Phi_e(\mathbf{r})$ are the magnetic vector and the electric scalar potentials, respectively given by

$$\mathbf{A}(\mathbf{r}) = \frac{\mu}{4\pi}\int_{s'}\mathbf{J}(\mathbf{r}')\frac{e^{-jkR}}{R}ds'\,, \tag{2.5}$$

$$\Phi_e(\mathbf{r}) = \frac{j}{4\pi\omega\varepsilon}\int_{s'}\nabla'.\mathbf{J}(\mathbf{r}')\frac{e^{-jkR}}{R}ds'\,, \tag{2.6}$$

where $\mathbf{r}$ and $\mathbf{r}'$ are the observation points and the source points, respectively, $\mathbf{J}(\mathbf{r}')$ is the unknown current density at the $\mathbf{r}'$ to be found, and R is the distance between the source point $(\mathbf{r}')$ and the observation point $(\mathbf{r})$. Using equation (2.5) and (2.6), equation (2.4) can be written as

$$\mathbf{E}^{i}_{tan}(\mathbf{r}) = \frac{j\omega\mu}{4\pi}\int_{s'}\mathbf{J}(\mathbf{r}')\frac{e^{-jkR}}{R}ds' + \frac{j}{4\pi\omega\varepsilon}\nabla\int_{s'}\nabla'.\mathbf{J}(\mathbf{r}')\frac{e^{-jkR}}{R}ds'. \tag{2.7}$$

In the moment-method solution, the unknown current density is expanded into a sum of N vector basis function, given by

$$\mathbf{J}(\mathbf{r}') = \sum_{n=1}^{N} I_n\mathbf{b_n}(\mathbf{r}')\,, \tag{2.8}$$

where I_n is the unknown coefficient to be found and $\mathbf{b_n}(\mathbf{r}')$ is the n^{th} vector basis function. Substituting equation (2.8) in (2.7), equation (2.7) can be written as

$$\mathbf{E}^{i}_{tan}(\mathbf{r}) = \sum_{n=1}^{N} I_n\left[j\omega\mu\int_{s'}\mathbf{b_n}(\mathbf{r}')\,G(\mathbf{r},\mathbf{r}')ds' + \frac{j}{\omega\varepsilon}\nabla\int_{s'}\nabla'.\mathbf{b_n}(\mathbf{r}')\,G(\mathbf{r},\mathbf{r}')ds'\right], \tag{2.9}$$

where G $(\mathbf{r},\mathbf{r}')$ is the free space greens function [5], [6] defined as

$$G(\mathbf{r},\mathbf{r}') = \frac{e^{-jkR}}{4\pi R}\,, \tag{2.10}$$

where $\mathbf{R} = |\mathbf{r} - \mathbf{r}'|$. To obtain a set of N linear equations with N unknowns, testing functions $\mathbf{t_m(r)}$ are defined. Taking the inner product of both sides of Equation (2.9) with the testing functions gives

$$\langle \mathbf{E}^{i}_{tan}(\mathbf{r}), \mathbf{t_m}(\mathbf{r}) \rangle = \sum_{n=1}^{N} I_n \left[j\omega\mu \left\langle \int_{s'} \mathbf{b_n}(\mathbf{r}')\ G(\mathbf{r},\mathbf{r}')\, ds', \mathbf{t_m}(\mathbf{r}) \right\rangle + \left\langle \frac{j}{\omega\varepsilon} \nabla \int_{s'} \nabla'.\mathbf{b_n}(\mathbf{r}')\, G(\mathbf{r},\mathbf{r}')\, ds', \mathbf{t_m}(\mathbf{r}) \right\rangle \right], \tag{2.11}$$

where $\mathbf{t_m}(\mathbf{r})$ is the m^{th} testing function. Using Galerkin testing, where the basis and testing functions are identical, Equation (2.11) can be written as

$$\langle \mathbf{E}^{i}_{tan}(\mathbf{r}), \mathbf{b_m}(\mathbf{r}) \rangle = \sum_{n=1}^{N} I_n \left[j\omega\mu \left\langle \int_{s'} \mathbf{b_n}(\mathbf{r}')\ G(\mathbf{r},\mathbf{r}')\, ds', \mathbf{b_m}(\mathbf{r}) \right\rangle + \left\langle \frac{j}{\omega\varepsilon} \nabla \int_{s'} \nabla'.\mathbf{b_n}(\mathbf{r}')\, G(\mathbf{r},\mathbf{r}')\, ds', \mathbf{b_m}(\mathbf{r}) \right\rangle \right], \tag{2.12}$$

Equation (2.12) can be written as a matrix equations as

$$\underbrace{\begin{bmatrix} V_1 \\ V_2 \\ \vdots \\ V_N \end{bmatrix}}_{V} = \underbrace{\begin{bmatrix} Z_{11} & Z_{12} & \dots & Z_{1N} \\ Z_{21} & Z_{22} & \dots & Z_{2N} \\ \vdots & \vdots & \ddots & \vdots \\ Z_{N1} & Z_{N2} & \dots & Z_{NN} \end{bmatrix}}_{Z} \underbrace{\begin{bmatrix} I_1 \\ I_2 \\ \vdots \\ I_N \end{bmatrix}}_{I}. \tag{2.13}$$

The divergence operator in Equation (2.12) leads to a development of fictitious charge at the common edge shared by cells if the normal component of the surface current across that edge is not continuous. However, normal continuity in surface current can be maintained across the cell interfaces by using divergence-conforming basis functions [29], [30]. With divergence-conforming basis functions, each term of the interaction matrix (Z) in Equation (2.13) can be written as

$$Z_{mn} = j\omega\mu \int_s \int_{s'} \mathbf{b_m}(\mathbf{r}).\mathbf{b_n}(\mathbf{r}')\, G(\mathbf{r},\mathbf{r}') ds' ds - \frac{j}{\omega\varepsilon} \int_s \int_{s'} \left(\nabla.\mathbf{b_m}(\mathbf{r})\right)\left(\nabla'.\mathbf{b_n}(\mathbf{r}')\right) G(\mathbf{r},\mathbf{r}') ds' ds\,, \tag{2.14}$$

and the left hand side vector of Equation (2.13) can be written as

$$V_m = \int_s \mathbf{E}^{i}_{tan}(\mathbf{r}).\mathbf{b_m}(\mathbf{r}) ds\,. \tag{2.15}$$

The sets of the N unknown coefficients $\{I_N\}$ can be obtained by inverting the interaction matrix using LU decomposition and then multiplying with vector V. However, this requires large computational time with electromagnetically large devices, as the interaction matrix is complex and densely filled and increases in order with the size of the modeled device. Two computational packages are available that implement the multi-level fast multipole algorithm (MLFMA) solver to significantly reduce both the storage and CPU time requirements over that needed by LU decomposition, the CONCEPT-II package [31] developed at the Hamburg University of Technology, Germany and a second package developed in-house at Oklahoma State University, USA. The integrand in (2.14) is singular when the source and observation points are same. The approach of Khayat *et al.* [42] is used to treat the singularity in the in-house package.

CHAPTER 3

PERFORMANCE OF FSV IN A HIGHLY RESONANT ENVIRONMENT

In this chapter, the performance of Feature Selective Validation (FSV) was evaluated by considering a single wire attached to the cavity and calculating the current at the base of the wire due to an external electromagnetic field. An FSV analysis is performed between the measurements and in-house code results of the same problem presented in [3] to examine how closely its evaluation matches with the opinion of experienced researchers. Another numerical simulation tool, CONCEPT II, is then used to numerically model the same problem, again keeping the cavity walls as ideally thin and the wire directly connected to the cavity walls as before. An FSV analysis is performed between the in-house code and the CONCEPT II results while introducing the variability in the positioning of current probe and the mesh structure of the numerically modeled problem. Finally, an FSV analysis is performed again using the same current probe locations in both simulation tools but still allowing differences in the mesh model of the problem.

3.1. Problem setup

3.1.1. Measurement setup

The measurement was performed in an anechoic chamber exposing the EUT with a vertically polarized field created by a transmit antenna positioned 1 m away from the front face of the cavity incident at a normal angle to the face containing aperture. A log-periodic antenna and a dual-ridged horn antenna were used as transmitters in the measurements to cover the wide band. Due to the operational frequency ranges, measurement was performed with an 8753ES VNA in the frequency range from 300 MHz to 8.5 GHz using log periodic antenna for frequencies below 1.5 GHz and dual-ridged horn antenna for frequencies above 1.5 GHz, as described in [3].

3.1.2. CONCEPT II and in-house code simulation setup

The equipment under test (EUT) is shown in Figure 3.1. The EUT consists of a thin-walled perfectly conducting cavity with a 15 x 6 cm aperture on its front face. The cavity dimension is 29.5 cm × 30 cm × 12 cm, matching the internal dimension of the cavity in [3], as better agreement can be seen between the simulation and the measurement when internal cavity dimension was used in the simulation [3]. The wire probe of length 10.4 cm, 0.41 mm radius wire, shown in Figure 3.1, is attached to the bottom of the box. The wire is 12 cm from both the front and the right faces of the box. In both in-house code and CONCEPT II simulation, the wire probe was modeled as a thin strip with a width of four times the physical wire radius as described in [43]. The induced current was computed at the test point due to a vertically polarized plane wave of 1 V/m magnitude, incident on the test box normal to the face with aperture. CONCEPT II does not allow a test point directly at the base of the strip. Hence, the test point was intentionally placed at 5.2 mm above the base of the wire in CONCEPT II.

The frequency range considered is from 300 MHz - 8.5 GHz, sampled at 20 MHz, giving a total of 411 frequency samples. Galerkin testing using a 6-point Gaussian quadrature was used to perform

the numerical integration in CONCEPT II. The maximum dimension of the triangular elements forming the mesh model of the cavity walls was 0.075 λ, where λ is the electromagnetic wavelength at the test frequency. Both the in-house numerical code and CONCEPT II are accelerated by the multi-level fast multipole algorithm (MLFMA). The primary differences between them are meshing tool used to generate the triangular patches that model the cavity walls and strip model of the wire probe. CONCEPT II uses GMSH [44] while the in-house code calculations were performed using BAMG [45]. The different meshes give slight differences in the numerical errors of the simulations that provide an interesting test case for FSV.

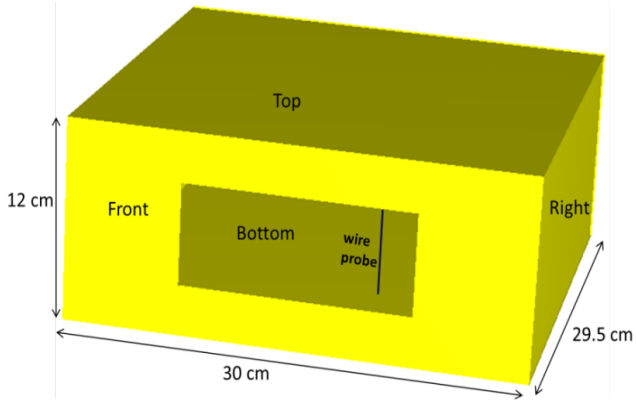

Figure 3.1. Cavity having aperture size of 15 x 6 cm used in [3].

3.2.Feature Selective Validation (FSV)

As discussed, FSV is an automated validation tool incorporated into the IEEE 1597.1 and 1597.2 standards [27] for use in validating computational electromagnetic (CEM) simulation. This validation tool reads two different data files which needs to be compared and then interpolate the comparison over a common frequency range. The validation it performs is based on amplitude differences and the feature differences occurred between the two data sets. The FSV measures are

i. Amplitude difference measure (ADM): This gives the comparison of overall shape between the two data sets.

ii. Feature difference measure (FDM): This gives the comparison of the rapidly changing data account for sharp peaks and troughs between the two data sets.

iii. Global difference measure (GDM): This combines the ADM and FDM to give the overall goodness of fit measure.

Table 3.1. FSV interpretation scale [25] [26]

FSV interpretation	FSV range
Excellent (EX)	$0 \leq$ FSV value < 0.1
Very Good (VG)	$0.1 \leq$ FSV value < 0.2
Good (G)	$0.2 \leq$ FSV value < 0.4
Fair (F)	$0.4 \leq$ FSV value < 0.8
Poor (P)	$0.8 \leq$ FSV value < 1.6
Very Poor (VP)	FSV value > 1.6

ADM, FDM and GDM are quantified at each frequency using the FSV value. Each FSV value is categorized into six natural language descriptors: excellent, very good, good, fair, poor and very poor as shown in Table 3.1 [25] [26]. The final decision of each measures in FSV is based on the average of all FSV value quantified at a particular frequency. Additional details on FSV are given in [25] [26].

3.3. Comparison between the measurement and in-house code results

Figure 3.2 shows the induced current at the base of the wire obtained by using the in-house code and the measurement, first presented in [3]. A seasoned researcher, well acquainted with the measurement approach and the inherent geometrical differences between a fabricated prototype and an ideal numerical model, would likely consider this very good agreement over most of the

frequency range while acknowledging amplitude differences from 3.5 to 4.5 GHz. The overall amplitude trends for the two curves are very similar overall. Possible reasons for the differences are the finite thickness in physical cavity walls, the method of attachment of the wire to the cavity base, and the general tolerances of the fabrication of the physical prototype used in the measurements.

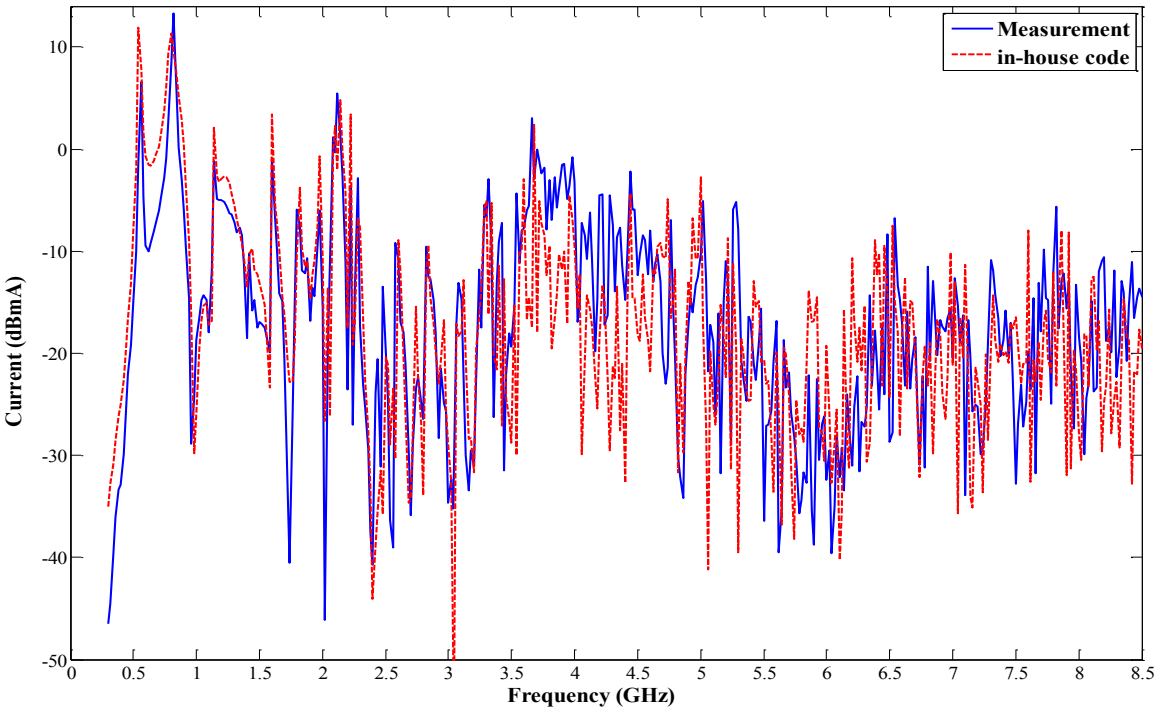

Figure 3.2. Induced current obtained by Measurement and in-house code stepping with 20 MHz frequency stepping.

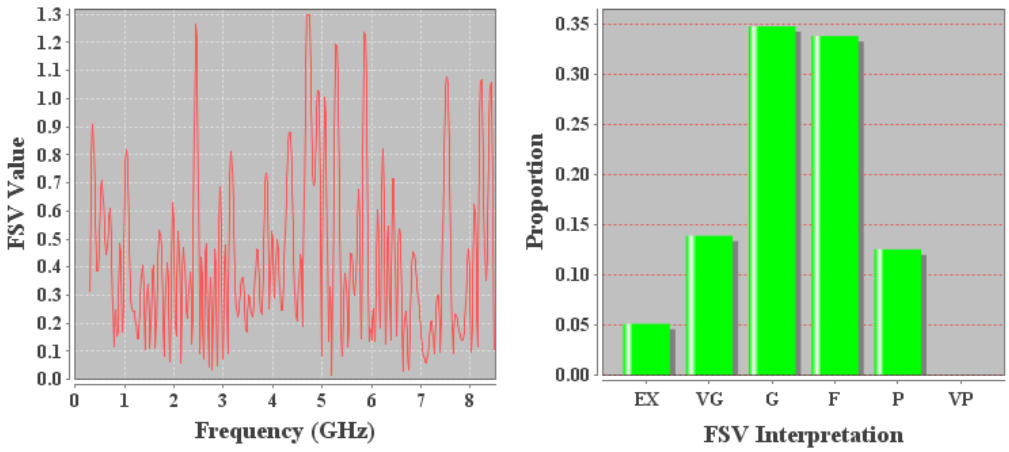

(a)

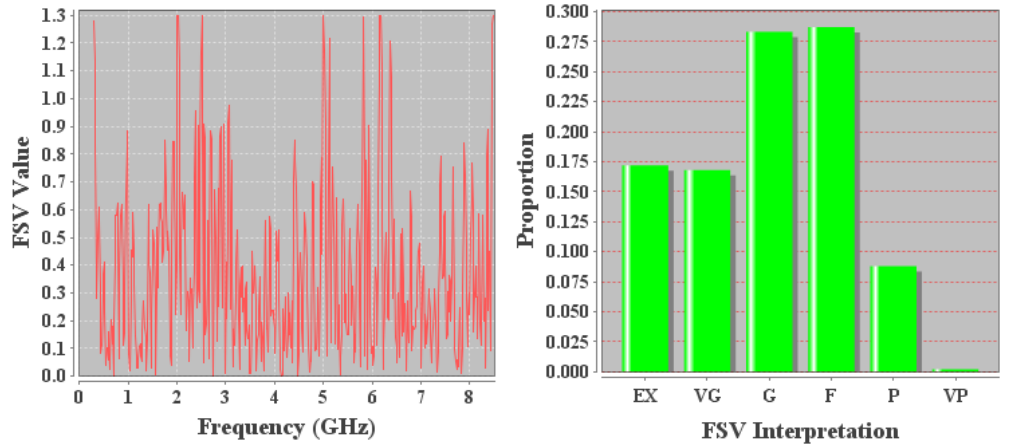

(b)

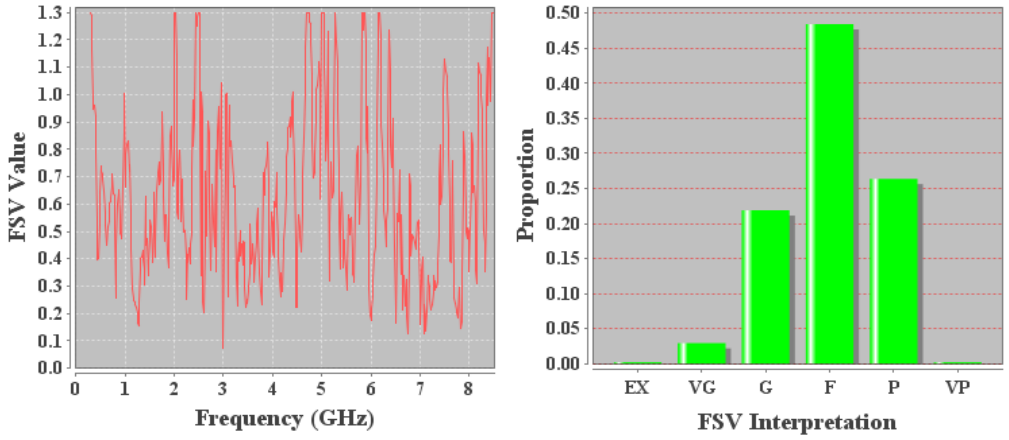

(c)

Figure 3.3. FSV analysis for comparison between measurement and in-house code results in terms of (a) ADM, (b) FDM and (c) GDM.

An FSV analysis of the measured and the simulated data of Figure 3.2 is shown in Figure 3.3. ADM shows 12.5 % and FDM shows 9% of the frequency samples are in poor agreement. FSV views the differences in terms of amplitude and feature difference and rates this as poor agreement without having prior knowledge on what condition the simulation and measurement was performed. Table 3.2 shows the overall assessment of the FSV analysis. Overall, fair agreement between the measurement and simulated results was analyzed by FSV.

Table 3.2. Overall assessment of comparison between Measurement and in-house code using FSV

ADM	0.4372 (Fair)
FDM	0.3754 (Good)
GDM	0.6336 (Fair)

3.4. Comparison results between in-house code and CONCEPT II

To overcome the differences seen between the measured and simulated results, same problem was also simulated using CONCEPT II. The physical dimensions of the wire and cavity combination were identical to those used with the in-house code presented above. Comparison was made first when there is an offset of sample point on the wire in both CONCEPT II and in-house code. Then the comparison was again made after keeping the sample point in both the simulation model at the same position.

3.4.1. Offset in the position of sample point

The sample point of the current was placed on the wire probe 5.2 mm above the point where the probe connects to the base (approximately 0.15 wavelengths at 8.5 GHz), giving an intentional

small physical difference in the modeled problem used to test FSV. The calculated currents are shown with the in-house code currents in Figure 3.4. The agreement is excellent overall, although the magnitudes of the resonances and nulls are slightly different. Figure 3.5 shows the FSV analysis on the responses in Figure 4. ADM, FDM and GDM gives very good agreement between in-house code and CONCEPT II as shown in Table 3.3. Excellent agreement was in fact expected from FSV based on the visual assessment of Figure 3.4. The observed differences can be expected from slight changes in the positioning of test point and different numerical mesh structures.

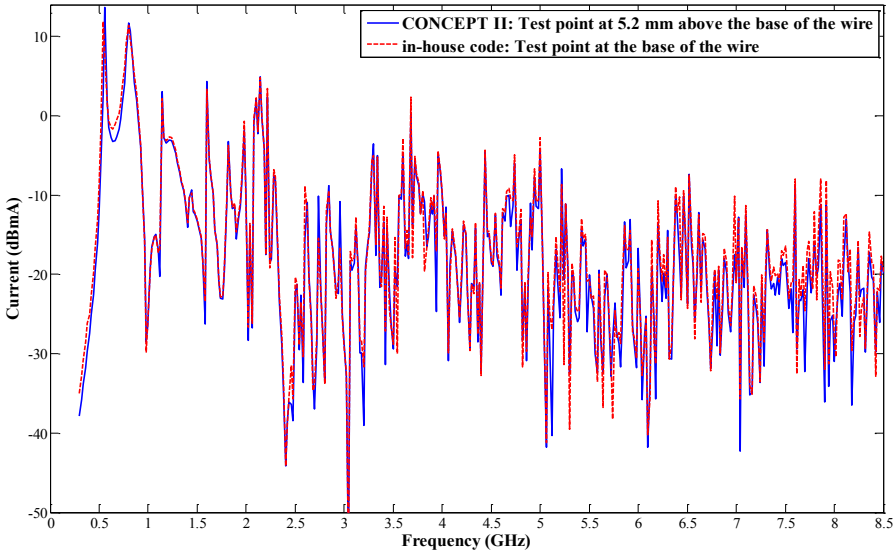

Figure 3.4. Induced current obtained by CONCEPT II at 5.2 mm above the base of the wire and in-house code at the base of the wire.

Table 3.3. Overall FSV assessment of comparison between CONCEPT II and in-house code results in Figure 3.4.

ADM	0.1066 (Very Good)
FDM	0.1201 (Very Good)
GDM	0.158 (Very Good)

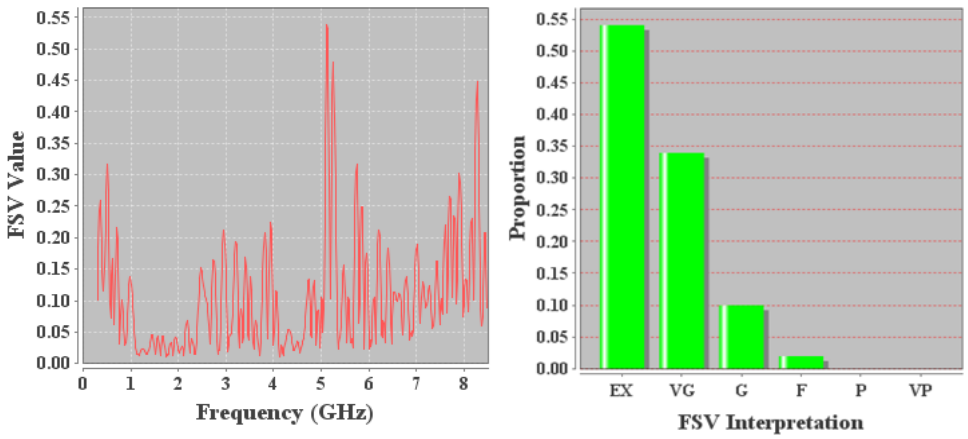

(a)

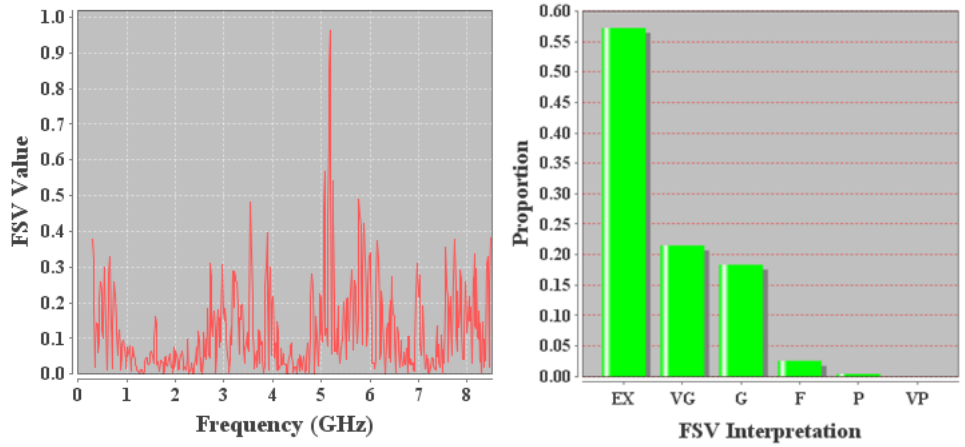

(b)

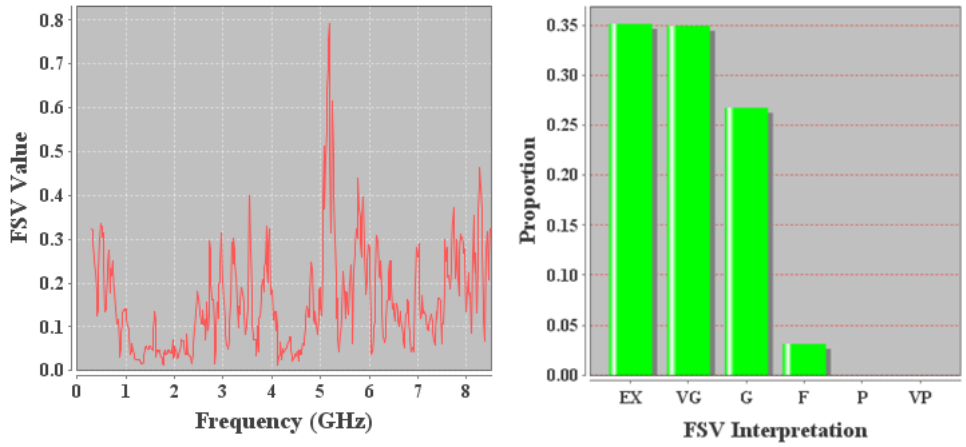

(c)

Figure 3.5. FSV analysis of CONCEPT II and in-house code results shown in Figure 3.4 in terms of (a) ADM, (b) FDM and (c) GDM.

3.4.2. Sample point at same position

To remove another variable, the in-house code simulation was repeated after placing the test point at 5.2 mm above the base of the wire and then compared with CONCEPT II. The only remaining difference between the numerically modeled problems is the wall mesh used in the MLFMA calculations. The results are shown in Figure 3.6. There are still minor differences in the calculated resonance and null depths. The FSV analysis for this comparison is shown in Figure 3.7 and summarized in Table 3.4. ADM assigns excellent agreement, agreeing with visual evaluation. FDM, however, only gives very good agreement. From Figure 3.7, FDM gives a higher (poorer) agreement assessment than ADM and GDM overall, but especially in the frequency range from 5.05 GHz to 5.23 GHz. FDM gives only fair agreement on that frequency range.

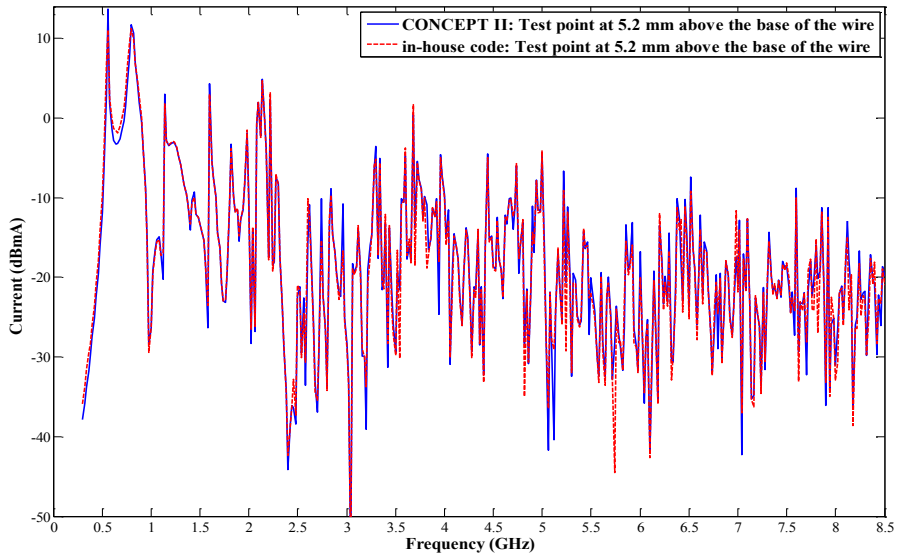

Figure 3.6. Induced current obtained by CONCEPT II at 5.2 mm above the base of the wire and in-house code at 5.2 mm above the base of the wire.

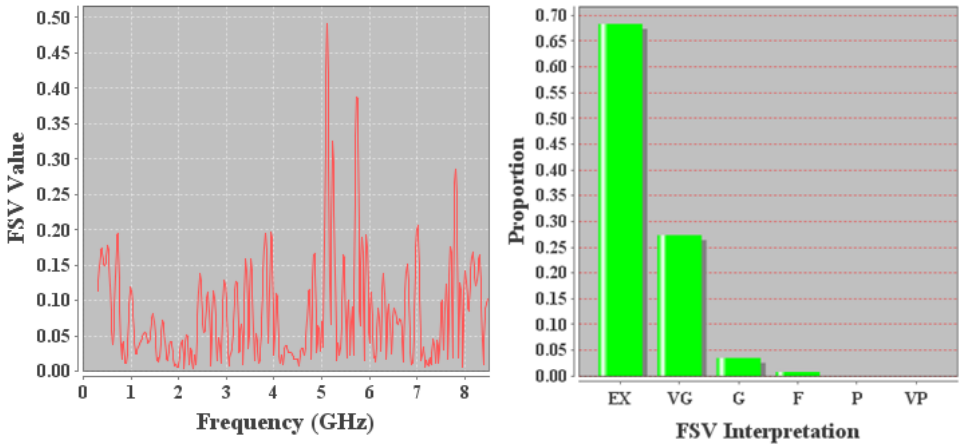

(a)

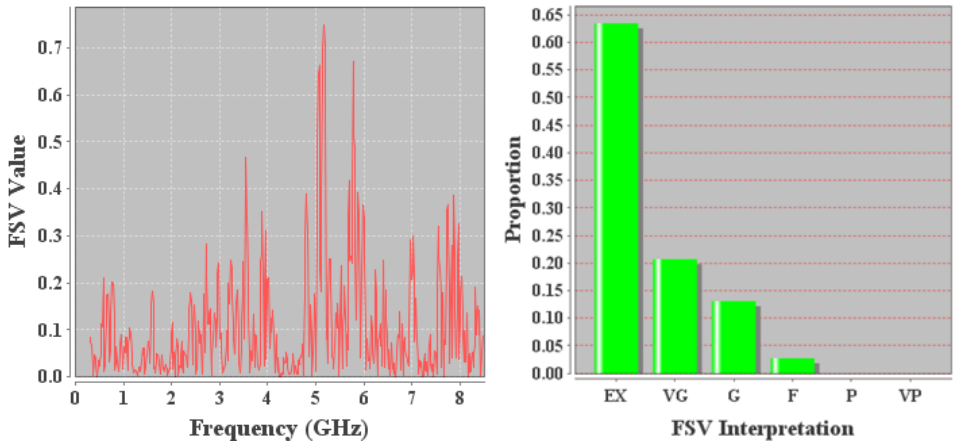

(b)

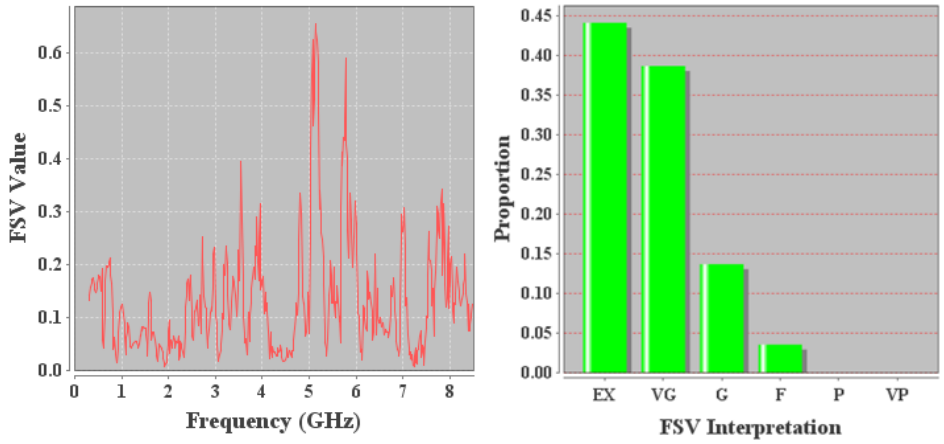

(c)

Figure 3.7. FSV analysis of CONCEPT II and in-house code results shown in Figure 3.6 in terms of (a) ADM, (b) FDM and (c) GDM.

Table 3.4. Overall FSV assessment of comparison between CONCEPT II and in-house code results in Figure 3.6.

ADM	0.0824 (Excellent)
FDM	0.1076 (Very Good)
GDM	0.1327 (Very Good)

Figure 9 in [3] suggested that there are very narrow resonances occurring more frequently that the 20 MHz sampling rate used in the numerical simulation in the frequency range from 5.05 GHz to 5.23 GHz. It is therefore possible that the magnitudes of some resonances were not fully detected or that resonances were completely missed in both numerical analyses. Hence, the simulations were repeated over this frequency range using both codes with a 1 MHz sampling rate. (Sampling at this rate across the entire frequency range is computationally prohibitive.) The induced currents obtained with both 1 MHz and 20 MHz sampling are shown in Figure 3.8.

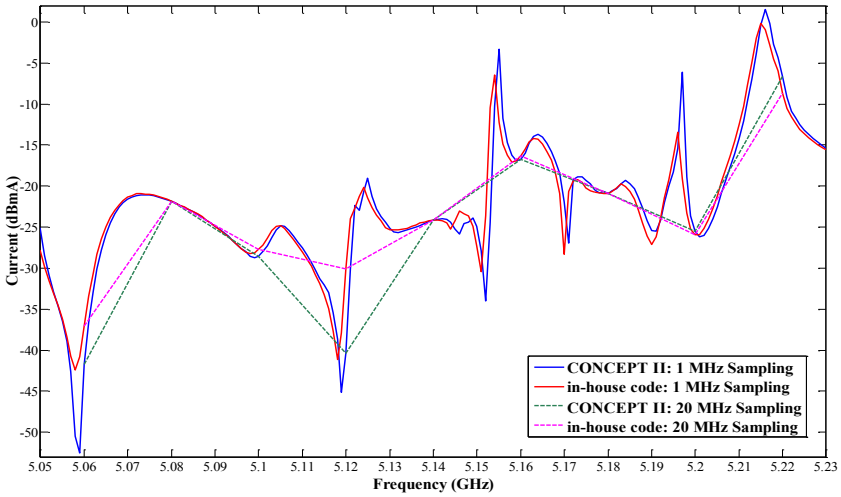

Figure 3.8. Induced current at 5.2 mm above the base of the wire in 5.05 GHz - 5.23 GHz.

Several resonances and nulls were indeed entirely missed at the 20 MHz sampling rate. The primary difference between the 20 MHz sampled CONCEPT II and in-house results occurs at 5.12 GHz, where the in-house code value is more than 10 dB below the CONCEPT II value. The 1 MHz

sampling of Figure 3.8 shows that this is because a very narrow null occurs near this frequency that is very slightly offset in frequency between the two codes, due to the different meshing. An FSV analysis was performed on the limited frequency range of Figure 3.8 with the 20 MHz sampling (only 9 points included in each curve). The full validation results are shown in Figure 3.9 and the overall assessments given in Table 3.5. FDM shows very good agreement while ADM shows a good agreement overall. The FSV analysis was repeated on the same frequency range but with the 1 MHz sampling (181 points). Figure 3.10 and Table 3.6 show the validation results. ADM gave very good agreement overall while FDM gave good agreement. Comparing Tables 3.5 and 3.6 shows that FSV assigns better agreement at 1 MHz sampling compared to 20 MHz sampling.

Table 3.5. Overall FSV assessment of comparison of the results in Figure 3.8 with 20 MHz sampling.

ADM	0.249 (Good)
FDM	0.1833 (Very Good)
GDM	0.329 (Good)

Table 3.6. Overall FSV assessment of comparison of the results in Figure 3.8 with 1 MHz sampling.

ADM	0.1307 (Very Good)
FDM	0.2403 (Good)
GDM	0.2695 (Good)

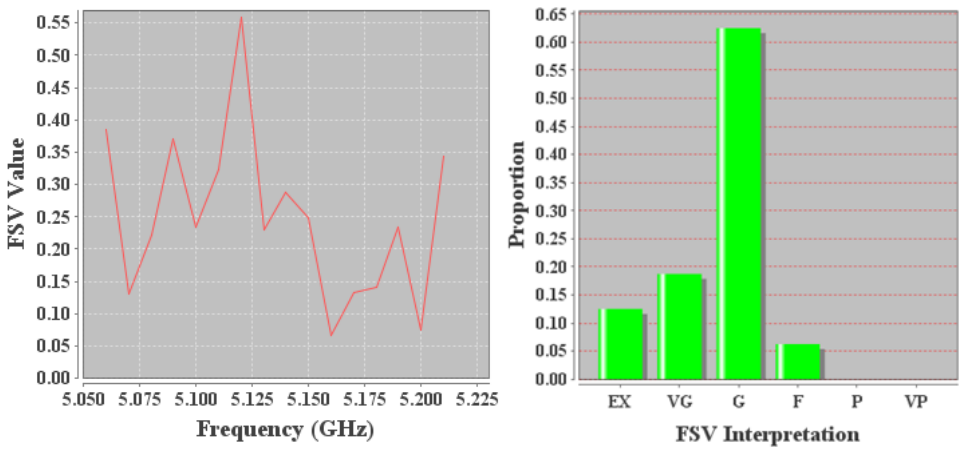

(a)

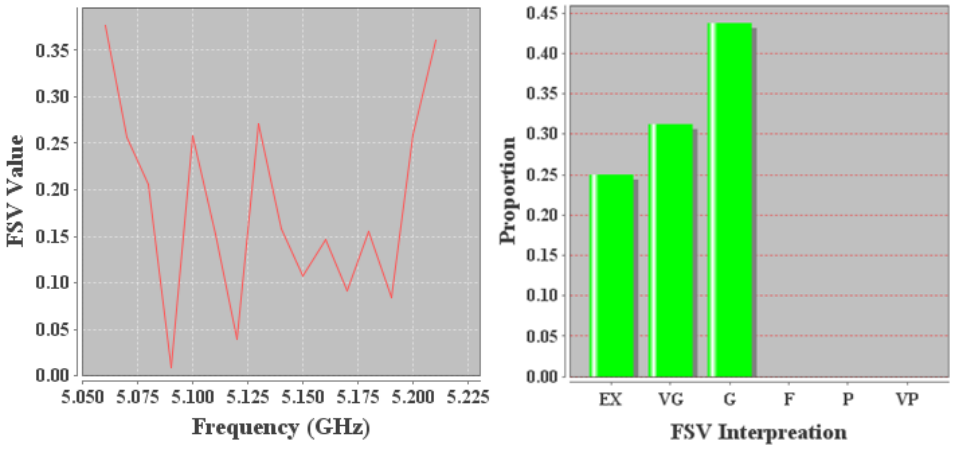

(b)

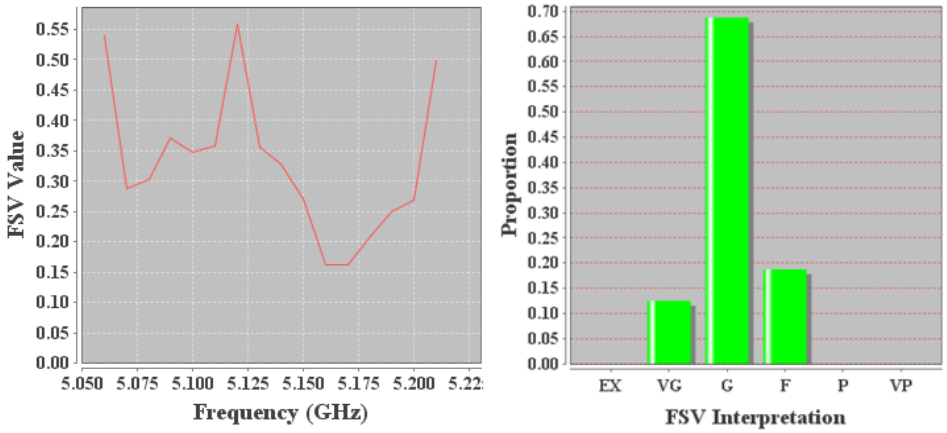

(c)

Figure 3.9. FSV analysis of CONCEPT II and in-house code results with 20 MHz sampling in terms of (a) ADM, (b) FDM and (c) GDM.

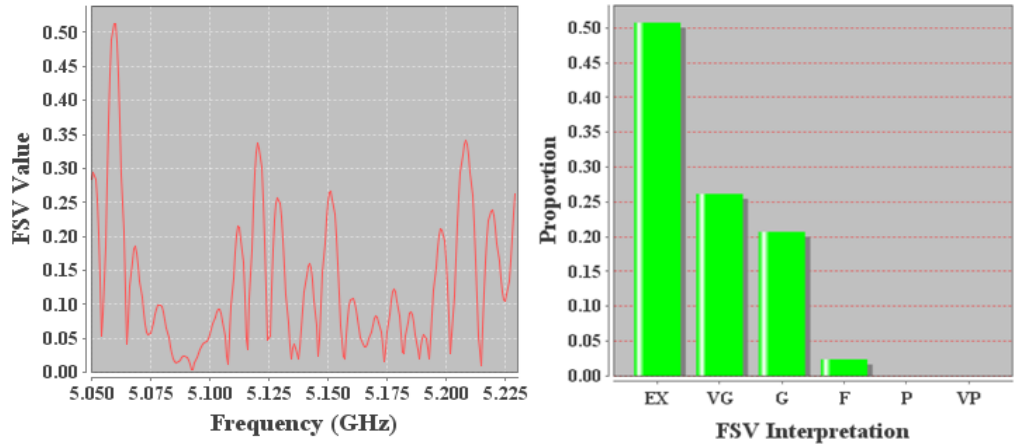

(a)

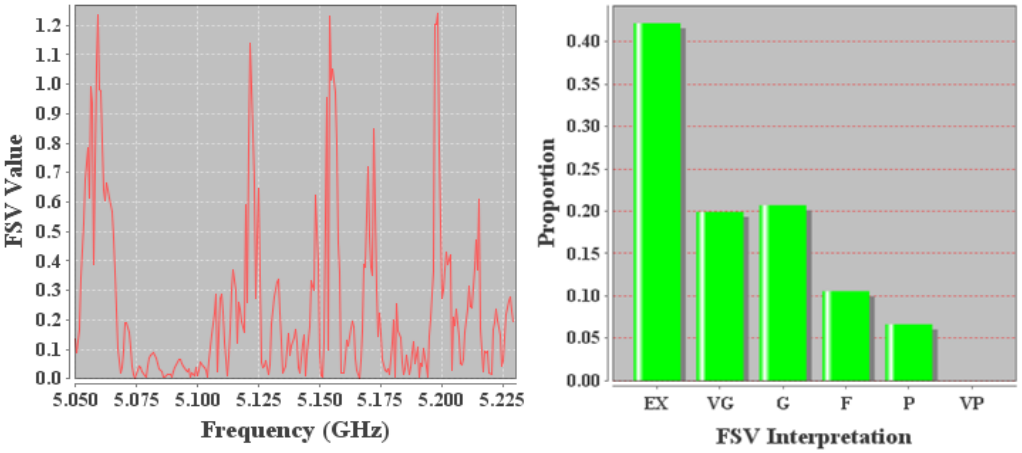

(b)

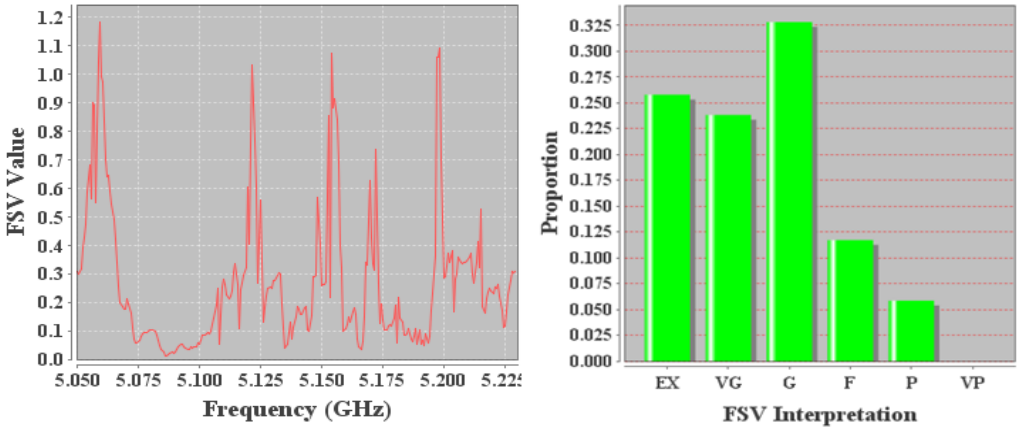

(c)

Figure 3.10. FSV analysis of CONCEPT II and in-house code results for 1 MHz sampling in terms of (a) ADM, (b) FDM and (c) GDM.

As shown in Table 3.4 and 3.6, the overall FSV value given by FDM increased from 0.1076 to 0.2403 when changing the frequency range of 300 MHz - 8.5 GHz sampled at 20 MHz to the frequency range of 5.05 GHz - 5.23 GHz sampled at 1 MHz. This corresponds to a reduction in the overall agreement from very good (almost excellent) to good. Figures 3.8 and 3.10 show that FSV interprets the poorest agreement in regions where there are offsets in the positions of resonant peaks and nulls predicted by the numerical codes, as well as the depths of the nulls. In particular, FDM gives poor agreement near frequencies where resonant peaks or nulls were offset by 1 MHz. This offset in the resonant frequencies is due the different mesh structure used in the simulations tool. A visual inspection of Figure 3.8 suggests that there should be excellent agreement as the strength and positions of extremely narrow nulls or resonances can be highly affected by even with very slight changes in geometry of the resonant structure. It was expected that both numerical simulation tools will not give the identical results due to a difference in the mesh structure. However, as per our visual inspection of Figure 3.8, better agreement was in fact expected from FDM than ADM, as all the resonant peaks and nulls predicted by both the tools occur almost at the same frequency (although slightly offset by 1 MHz) while large differences in amplitude of resonant peaks and nulls was observed.

3.5. Conclusion

The ability of the Feature Selective Validation (FSV) tool to evaluate the agreement between measured and numerically simulated currents in a highly resonant environment has been considered. FSV assigns fair agreement when comparing measured and simulated results that an experienced researcher would likely consider to be very good. The numerical computations were then repeated using a different simulation tool with intentional differences in the current sample point and/or numerical mesh. The FSV analysis proved highly sensitive to changes in the magnitudes and frequencies of resonances and nulls that are introduced by both small changes in

the geometry or numerical mesh of the sampled problem. Similar behavior was observed with the null differences in antenna far field pattern plotted in dB by Johnson *et al*. [46]. Overall, the results show that great care must be used when applying an automated validation tool to the induced currents or fields in a highly resonant environment.

CHAPTER 4

IMPLEMENTATION OF HIGHER ORDER BASIS FUNCTION

The previous chapter shows the numerical simulation results in a highly resonant environment obtained by both CONCEPT II and an in-house CEM code. Both simulation tools used Rao-Wilton-Glisson (RWG) basis functions for approximating currents on the triangular patches of the metallic surfaces. An RWG basis function is defined on a pair of two triangles each sharing a common edge. The surface current represented by this basis function gives a constant-normal current at the joint edge and a linear tangential component along the unshared patch edges as shown in Figure 4.1. The RWG basis function is therefore often referred to as CN/LT. RWG is a divergence conforming basis function, basis function that maintains the continuity of its normal component across the cell boundaries to prevent the accumulation of fictitious charge at the common edge shared by two triangular patches. The RWG basis function is the lowest order member among the family of divergence conforming basis functions [29] [30]. As discussed before in Chapter 1, finer cell size results in large computational times at higher frequencies. Therefore, the use of higher order divergence conforming basis function can achieve the required accuracy with less computational efforts. In this chapter, linear normal / quadratic tangent (LN/QT) basis function, proposed by Peterson *et al.* [29] [32] is considered. This basis function represents first-order divergence conforming basis functions, one order above RWG basis functions [29] [30] [32].

Three different test cases are considered to analyze the performance of LN/QT basis functions against RWG basis functions. All test cases solve the electric field integral equation (EFIE) using MLFMA calculations.

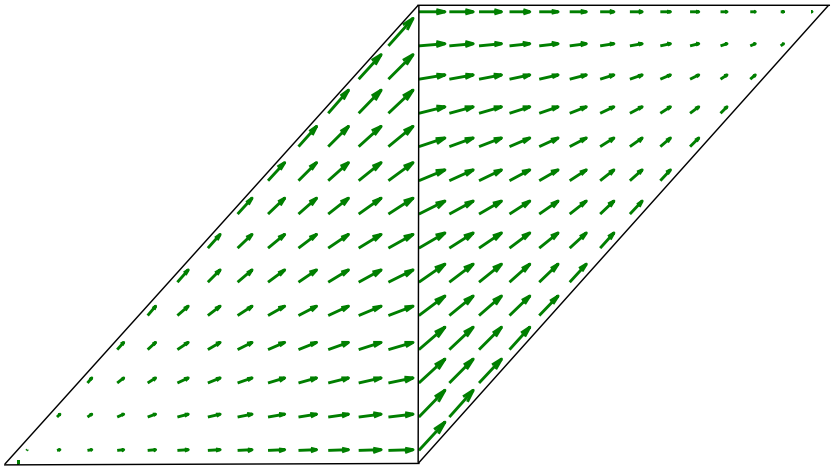

Figure 4.1. RWG basis function associated with a pair of two triangular cell

4.1. Linear Normal/Quadratic Tangent (LN/QT) basis function

Like RWG basis function, the LN/QT basis function is also defined on a pair of two triangular cells, each sharing a common edge. Sample LN/QT basis functions are shown in Figure 4.2. Two basis function are associated with the shared edge, giving a linear normal component across that edge. Additionally, two basis functions are assigned to each triangular cell that gives a quadratic tangential component and zero normal component along all three edges of the cell. So, there are eight LN/QT basis functions for each triangular cell with all three edges not located on a target boundary. These basis functions are defined in terms of simplex coordinates [29] [30]. Appendix A gives the mathematical representation of the LN/QT basis function.

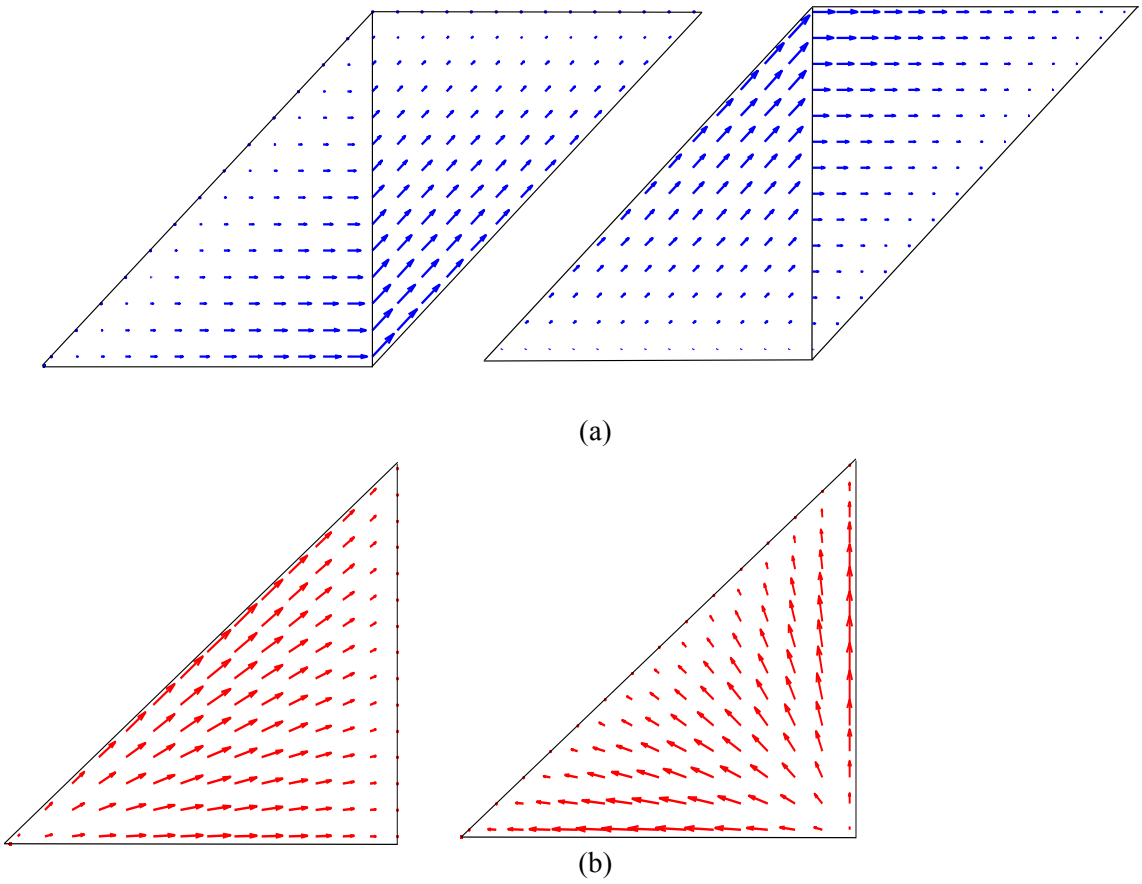

Figure 4.2. Four LN/QT basis function with (a) two edge-based basis function and (b) two cell-based basis function.

4.2. Computational time

The total computational time for solving EFIE is the sum of MLFMA solver time and the fill time in the in-house CEM code. In an in-house code, green functions due to all possible combinations of source and observation points are calculated. These calculated values are then stored in a hash table with the labels of source and observation points. Fill time is the total time required for calculating and storing all calculated greens functions on the hash table library. Each calculated value using RWG basis function can be reused 9 times whereas LN/QT basis function can reuse 64 times.

4.3. Test cases

4.3.1. Perfectly conducting (PEC) square plate

Figure 4.3 shows the perfectly conducting flat plate having a dimension of 1λ × 1λ, where λ is the wavelength, lying in x-y plane. The equivalent surface currents induced on a plate due to a normally incident plane wave is computed by using the EFIE formulation described in Section 2.3.1. The electric field component (E_{inc}) of the plane wave is in the direction parallel to the plate as shown in Figure 4.3. This plate is divided into 128 triangular cells, leading to 176 non-boundary edges. This gives a total of 608 LN/QT basis functions and 176 RWG basis functions for representing surface current density with same cell size.

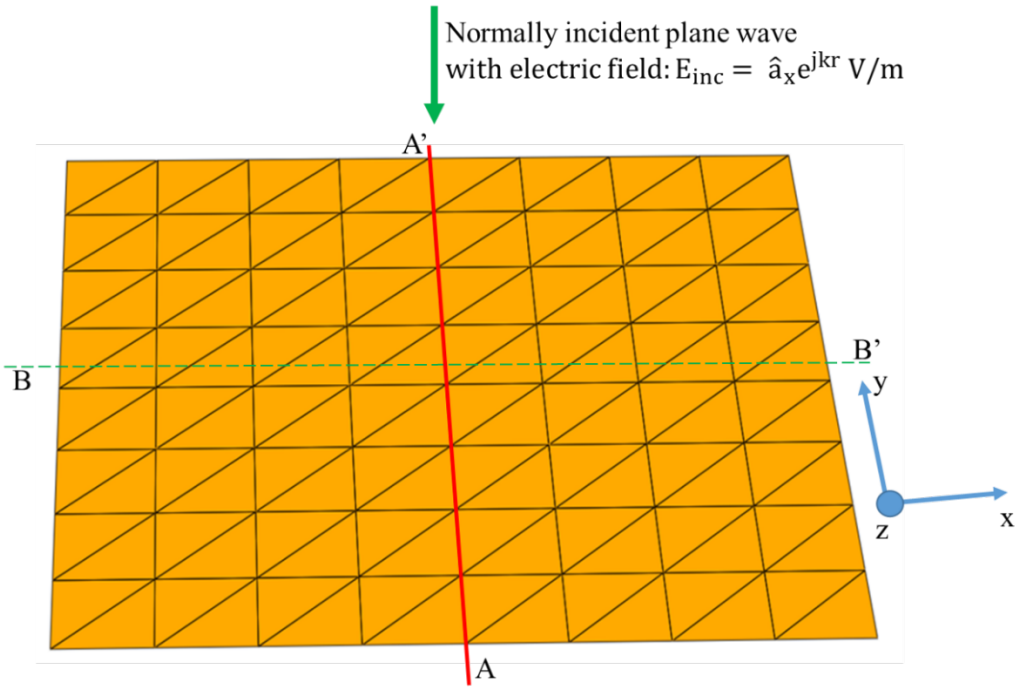

Figure 4.3. Flat plate of dimension 1λ × 1λ discretized into 128 triangular cells.

Aberegg *et al.* [33] show that for the same number of unknowns or basis functions, LN/QT results are more accurate compared to CN/LT results for the square cells. So, a larger cell size can be used with LN/QT basis functions compared to the CN/LT basis function (or RWG basis function for the

triangular cell) to achieve the same level of accuracy. Figure 4.4 shows the plot of dominant component of induced current density obtained along BB' cut and AA' cut on the flat conducting plate.

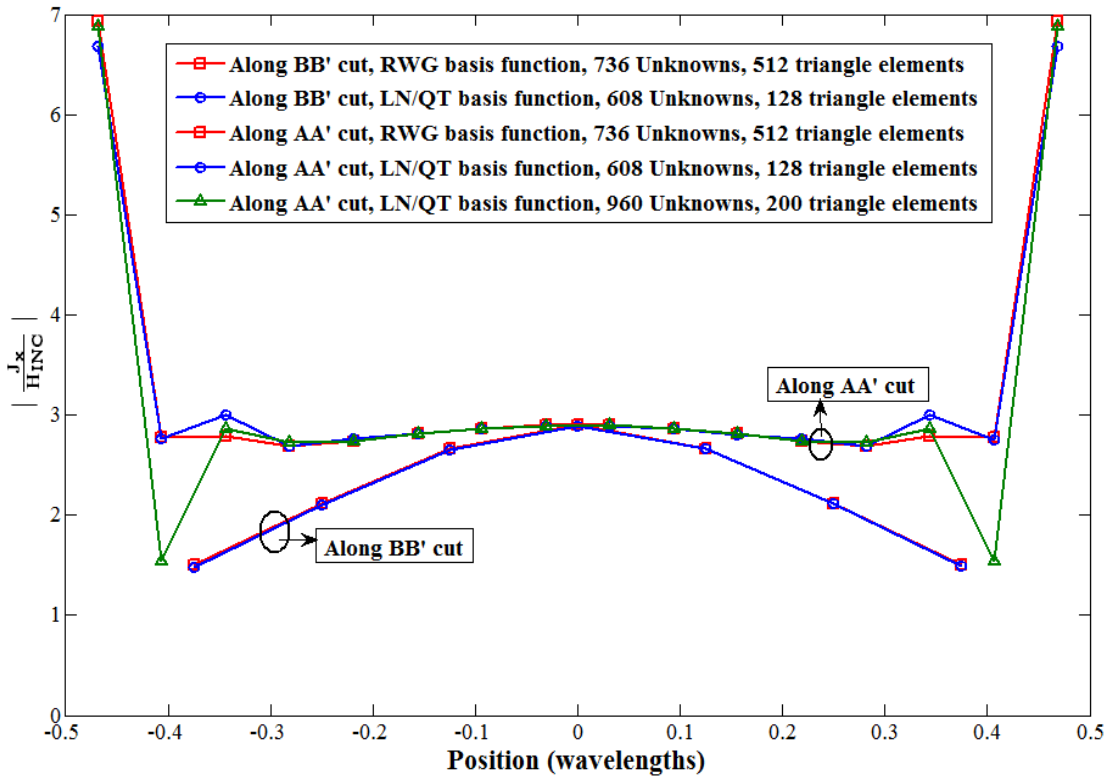

Figure 4.4. Distribution of dominant component of induced current density on the flat plate

It shows that the result represented by 608 LN/QT basis function matched with the result as obtained by using 736 RWG basis functions. However, a sharp dip in the surface current density result is observed near the edges of the plate using 960 LN/QT basis functions as shown in Figure 4.4. Similar behavior was reported in [47] when using the piecewise linear basis function at the edge of an infinite strip in TM scattering. The reason mentioned in [47] for this sharp dip are due to a basis function not incorporating the edge singularity near the edge of the flat plate. Both results using RWG and LN/QT basis function showing discontinuities near the plate edges. Hence, it is difficult to make the comparison between LN/QT and RWG results near the plate edges. But, same

results can be obtained except near the plate edges using LN/QT basis function as with RWG basis function with even less computational time. Table 4.1 shows the computational statistics both for using RWG and LN/QT basis functions.

Table 4.1. Simulation statistics of induced current density results shown in Figure 4.4.

Number of elements	Basis function type	Number of unknowns	Cell size (in wavelengths)	Fil time (in seconds)	Total computational time (in seconds)
512	RWG	736	0.0625	5.03	5.51
128	LN/QT	608	0.125	1.27	1.59
200	LN/QT	960	0.1	2.88	4.49

Also, the monostatic radar cross section of flat conducting plate is also considered for the various incident angle of a plane wave (α). This cross section (σ) is given by

$$\sigma = \lim_{r \to \infty} 4\pi r^2 \left| \frac{E_{scat}}{E_{inc}} \right|^2, \tag{4.1}$$

where E_{inc} is the incident electric field measured at the flat plate and E_{scat} is the scattered electric field at a distance r from the flat plate. Figure 4.5 shows the monostatic radar cross section results using both RWG and LN/QT basis functions.

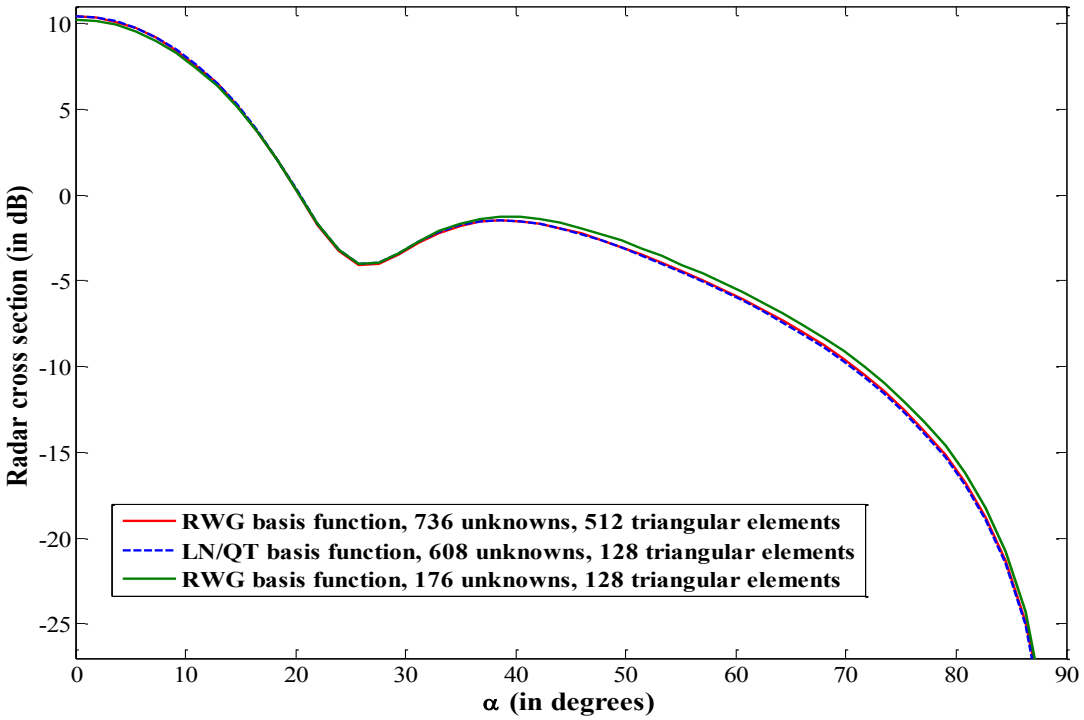

Figure 4.5. Monostatic radar cross section of the PEC flat plate

Table 4.2 shows the statistics of the numerical simulation used for obtaining the radar cross section results. It shows that same level of accuracy with less computational time can be obtained by using LN/QT basis function with less number of unknowns compared to RWG basis function.

Table 4.2. Simulation statistics of radar cross section results in Figure 4.5.

Number of elements	Basis function type	Number of unknowns	Cell size (in wavelengths)	Fill time (in seconds)	Total computational time (in seconds)
128	RWG	176	0.125	0.36	0.7
512	RWG	736	0.0625	4.41	6.34
128	LN/QT	608	0.125	1.32	3.06

4.3.2. Perfectly conducting (PEC) cube

Second test case considered is to calculate the monostatic radar cross section of the perfectly conducting cube having a dimension of 1λ × 1λ × 1λ, where λ is the wavelength, as shown in Figure 4.6. Figure 4.7 shows the monostatic radar cross-section results using both RWG and LN/QT basis functions, when $\phi = \pi/8$. It shows that RWG basis function compared to LN/QT basis function is slightly inaccurate for the same mesh. Table 4.3 shows the statistics of the numerical simulation. It shows that LN/QT basis function compared to RWG basis function reduces the total computational time by a factor of 1.76 to obtain a similar accuracy in the simulated results. Figure 4.8 shows the monostatic radar cross section results, when $\phi = 0$.

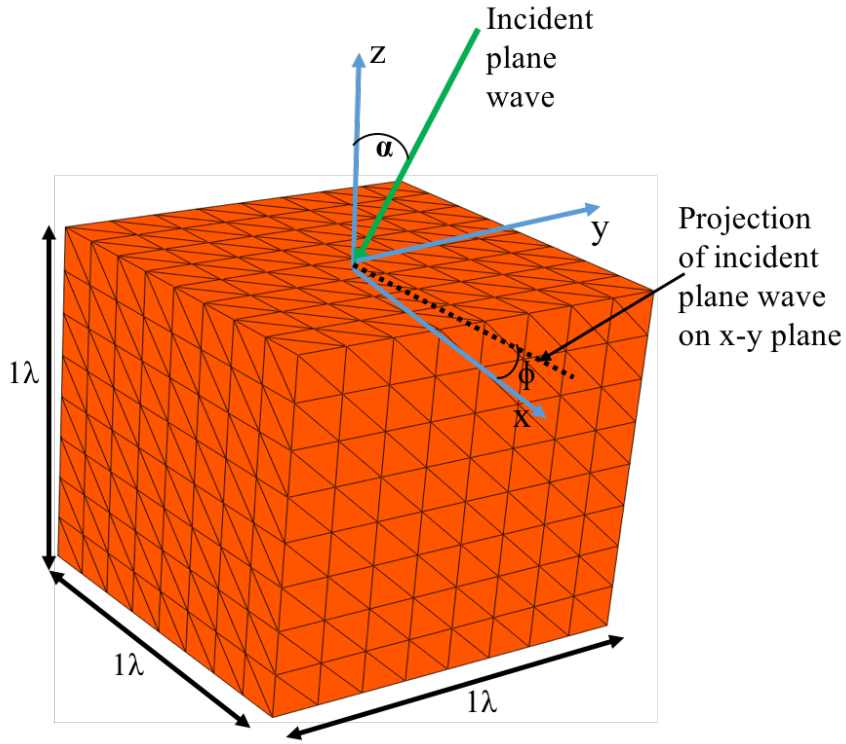

Figure 4.6. Plane wave scattering from PEC cube

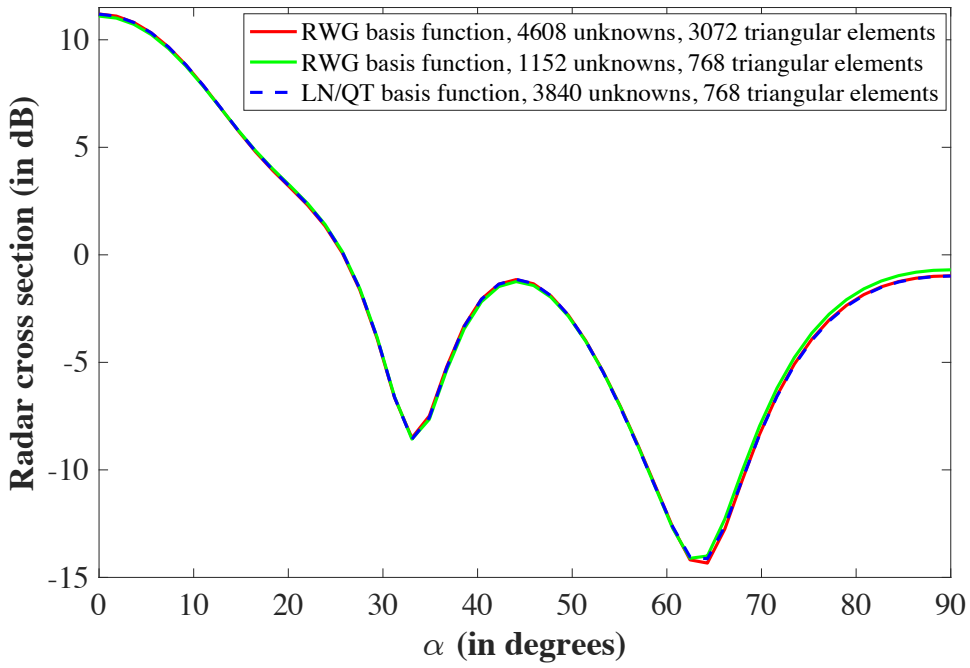

Figure 4.7. Monostatic radar cross section of the PEC cube when $\phi = \pi/8$.

Table 4.3. Simulation statistics of radar cross section results in Figure 4.7.

Number of elements	Basis function type	Number of unknowns	Cell size (in wavelengths)	Fill time (in seconds)	Total computational time (in seconds)
768	RWG	1152	0.125	4.02	19.7
3072	RWG	4608	0.0625	63.6	164.9
768	LN/QT	3840	0.125	14.98	93.7

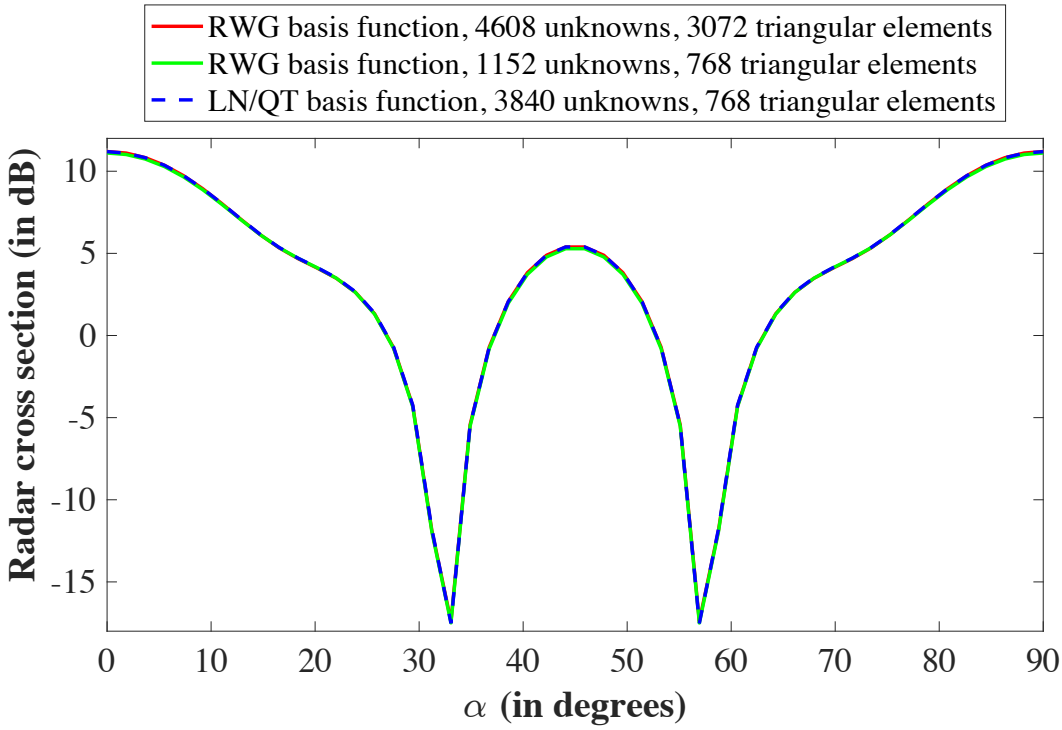

Figure 4.8. Monostatic radar cross section of the PEC cube, when ϕ = 0.

4.3.3. Wire inside a cavity with an aperture

Another test case considered is the wire inside the cavity contain aperture on its front face, as shown in Figure 3.1. The wire is modeled as a strip, as discussed in Chapter 3. Figure 4.9 shows the mesh generated from COMSOL [48]. Use of COMSOL as a mesh generator is found in [49]. The strip is aligned in x-z plane. The induced current is calculated at edge AB which is 5.2 mm above the base of the wire as shown in right side of Figure 4.9. Both RWG and LN/QT basis function are used to model the surface current on the triangular patches, accelerated by MLFMA. Total induced current using LN/QT basis function crossing the edge AB in Figure 4.9 can be obtained by

$$I = \int_{AB} J_z(x, y, z)\, dx\,, \tag{4.2}$$

where $J_z(x, y, z)$ is the normal component of induced current density at a point (x, y, z) on the edge AB. The integration is performed along the x direction, as the edge AB is aligned with the x-axis.

Induced current results are shown in Figure 4.10 obtained by using both LN/QT and RWG basis function in the frequency range from 300 MHz to 1 GHz. The top figure on the right side of Figure 4.10 shows the current response in frequency range from 600 MHz to 750 MHz. Similarly, the bottom figure on the right side of Figure 4.10 the current response in frequency range from 850 MHz to 925 MHz. Figure 4.10 shows that LN/QT basis functions modeled with 533 triangular patches gives the nearly identical result as with RWG basis function modeled with 2488 triangular patches and having more number of unknowns. This shows that RWG basis function with 1766 triangular patches gives slightly inaccurate results compared to LN/QT basis function with 533 triangular patches with same number of unknowns. Table 4.4 shows the statistics of numerical simulation to obtain the frequency response of the induced current density. It shows the reduction of total computational time by 5 times with LN/QT basis function to obtain a similar accuracy in the results as with RWG basis function.

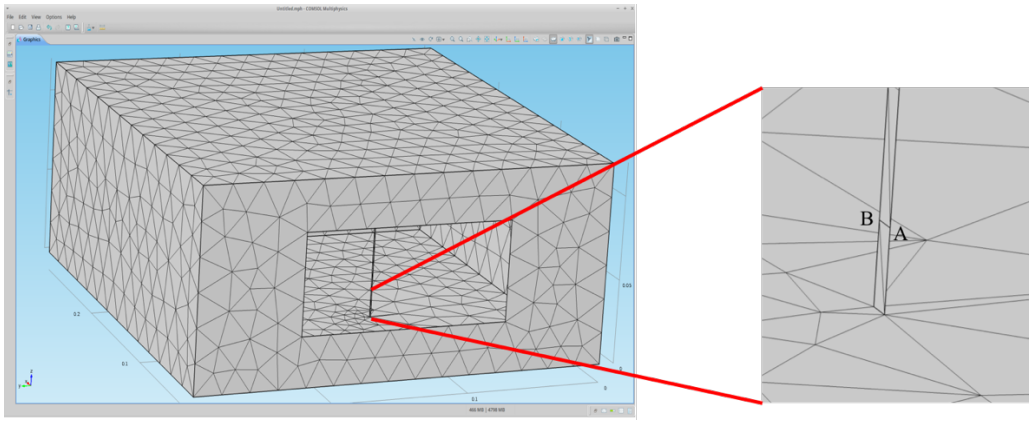

Figure 4.9. COMSOL mesh for cavity shown in Figure 3.1 discretized into 1766 triangular patch elements.

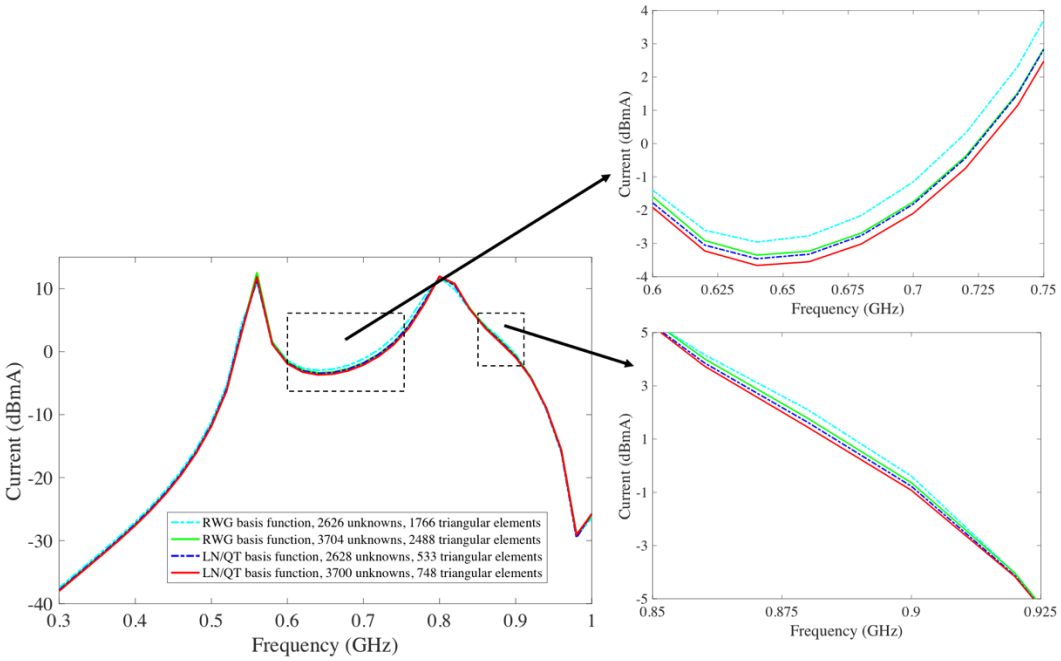

Figure 4.10. Induced current at 5.2 mm (edge AB in Figure 4.9) above the base of the wire

Table 4.4. Simulation statistics of induced current results shown in Figure 4.10.

Number of elements	Basis function type	Number of unknowns	Maximum cell size at 1GHz (in wavelengths)	Fill time (in seconds)	Total computational time (in seconds)
1766	RWG	2626	0.075	3204.04	3712.66
2488	RWG	3704	0.06	6673.24	7571.62
533	LN/QT	2628	0.17	883.47	1467.34
656	LN/QT	3240	0.15	1901.66	2671.87
748	LN/QT	3700	0.125	2140.83	3750

4.4. Conclusion

In this chapter, the in-house CEM code is enhanced by implementing LN/QT vector basis function for modeling the surface current for each triangular patch using EFIE. Three test cases were considered to demonstrate the performance of LN/QT vector basis function over RWG basis function, as discussed in Section 4.3. In all test cases, LN/QT basis function used less number of unknowns and hence larger dimensions of triangular patches compared to RWG basis function to achieve the same accuracy in the results. The total computational time using LN/QT is still less even solving EFIE with more number of unknowns compared to RWG basis functions.

CHAPTER 5

VALIDATION OF SIMULATED RESULTS AGAINST ANECHOIC CHAMBER MEASUREMENTS

Numerical simulation of radiation and scattering problems using first-order LN/QT basis functions was performed on three different test cases in the previous chapter. The test cases considered were:

(a) Calculation of the induced current density on a 1 $\lambda \times 1 \lambda$ perfectly conducting plate by a normally incident uniform plane, where λ is the wavelength in a medium.

(b) Calculation of the radar cross section of a 1 $\lambda \times 1 \lambda$ perfecting conducting plate and a 1 $\lambda \times 1 \lambda \times 1 \lambda$ cube as a function of uniform plane wave incident angle.

(c) Calculation of the response of a representative equipment under test (EUT) due to a vertically polarized uniform plane wave over a frequency range from 300 MHz to 1 GHz. The EUT consisted of a thin-walled perfectly conducting cavity with a 15 cm × 6 cm aperture on its front face. The uniform plane wave was normally incident on the face containing the aperture. The cavity dimension was 29.5 cm × 30 cm × 12 cm. The wire probe of length 10.4 cm, 0.41 mm radius wire, shown in Figure 3.1 of Chapter 3, was attached to the bottom of the box. The wire is 12 cm from both the front and the right faces of the box. The response of EUT is the induced current at 5.2 mm above the base of the wire.

It was found that the same accuracy in the numerical simulation as obtained with the commonly used RWG basis functions can be achieved with less computational effort using LN/QT basis functions. In this chapter, numerical simulation using LN/QT basis functions are validated against measurements of the current induced on the probe of the EUT of Fig. 3.1 performed within an anechoic chamber.

5.1. Overview of test case used for validation

The test case used for validating numerical simulation against the measurements is to expose the EUT to a single uniform plane wave with vertical polarization and a magnitude of 1 V/m and normally incident on the face containing the aperture. The induced current is then calculated at the attachment point between the wire and cavity wall over a frequency range from 300 MHz to 8.5 GHz. Measurements within the anechoic chamber and a numerical simulation using RWG basis functions of this problem were performed in [3].

In earlier work [3], the measurements were performed using an Agilent 8753ES vector network analyzer (VNA). The transmitting antenna was connected to port 1 of VNA and the wire inside the aperture box was connected to port 2 of VNA. The wire probe of length 10.4 cm was connected to the cavity wall through SMA connector. This SMA male connector was connected to an N-type male connector coaxial cable from VNA via adapter shown in Figure 5.1. The wire was located at 12 cm away from the aperture face (front face) and the right face of the cavity (position 7 in Fig. 2 [3]). Figure 5.2 shows the measurement setup that was used in the anechoic chamber by Rajamani *et al.* [3]. In this setup, the transmitting antenna was kept at 1 m away from the front face of the cavity. The transmitting antenna and the EUT were oriented so that a vertically polarized plane wave was normally incident the aperture face. Rajamani *et al.* [3] adjusted the VNA power using an E-field probe to achieve a field strength of 1 V/m at the aperture face. Figure 5.3 shows the

measured and simulated current induced through a 50 Ω load (representing the impedance of an SMA connector) at the base of the wire presented by Rajamani *et al.* [3].

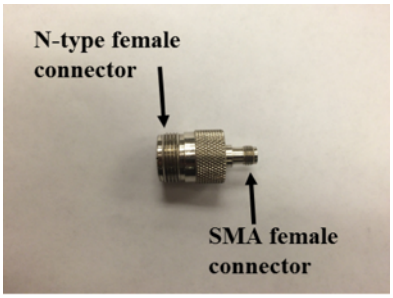

Figure 5.1. SMA female / N-type female adapter.

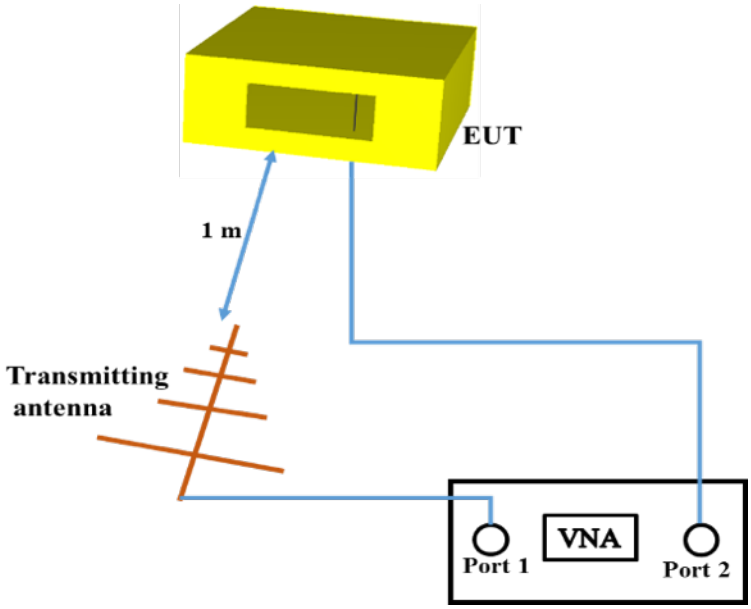

Figure 5.2. Measurement setup in the anechoic chamber used in [3].

The authors in [3], as experienced researchers, viewed the comparison between the measurement and numerical simulation as very good over most of the frequency range while acknowledging the amplitude differences from 3.5 GHz to 4.5 GHz. The measurement was performed with a cavity constructed from aluminum with wall thicknesses of 0.193 cm on the top, bottom, and side faces

and 0.635 cm on the front (containing the aperture) and back faces. In the simulation, however, the cavity walls were modeled as ideally thin, perfectly electric conducting (PEC) plates. It was suggested in [3] that aperture resonances, due to the finite thickness of aperture face in the cavity used in the measurements, might contribute the observed differences in the measured and simulated responses in Fig. 5.3 in the frequency range from 3.5 GHz to 4.5 GHz.

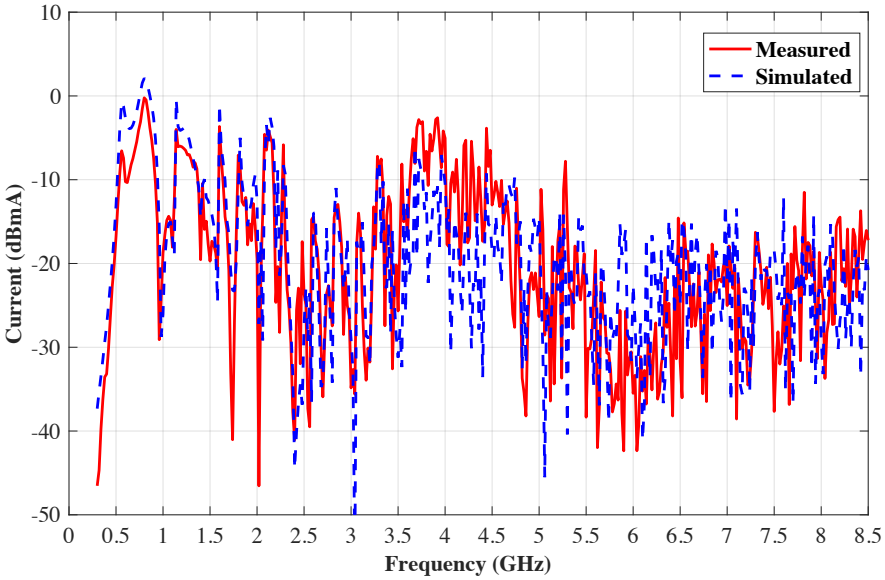

Figure 5.3. Measured and simulated induced current at the base of the wire through a 50 Ω load, as presented in [3].

In this chapter, additional measurements were performed to investigate if an aperture resonance was responsible for the discrepancies between the measured and simulated currents in Figure 5.3. The EUT cavity was modified to have an aperture face of thickness 0.193 cm and the measurements repeated. The thickness of back face of the cavity was not changed. Figure 5.4 shows the constructed cavity that was used in the measurements. Its internal dimensions are 30 cm × 30 cm × 12 cm. The finite wall thicknesses give external dimensions of 30.83 cm × 30.39 cm × 12.39 cm.

Figure 5.4. Fabricated EUT with modified aperture face of 1.93 mm aluminum thickness.

Additionally, Rajamani *et al.* [3] noted other differences between the physical EUT and the numerically simulated geometry. First, the 10.4 cm long wire probe was connected to the cavity wall through an SMA connector. Also, possible geometrical differences include uncertainties in the aperture position on the front face, the exact wire position on the cavity floor, the cavity dimensions, or the straightness of the wire probe of the fabricated EUT. Therefore, the measurements and the simulations were performed for the three different of wire probe locations within the EUT shown in Figure 5.5 (also shown in Table 5.1) to observe whether the same level of agreement is achieved for all probe locations. The measurement setup shown in Figure 5.2 was again used.

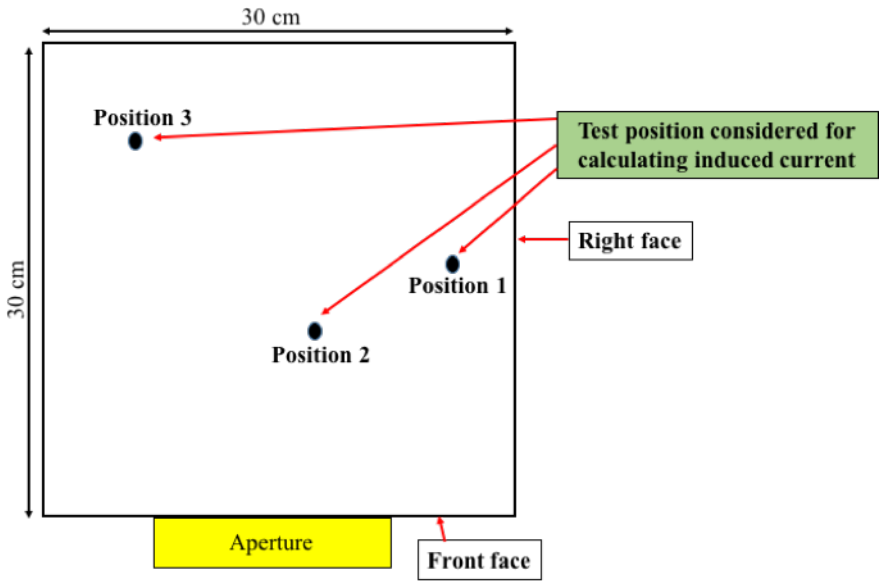

Figure 5.5. Positions of wire considered on the cavity floor.

Table 5.1. Coordinates of the wire positions considered on the cavity floor.

Location of wire	From front face (in cm)	From right face (in cm)
Position 1	15.6	4
Position 2 (same as position 7 in [3])	12.5	12
Position 3	24.5	24

5.2. Calculation of induced current on a wire using measured scattering parameters

There is a need to calculate the current induced at the base of the wire through an SMA connector (represented by 50 Ω load impedance) due to a 1 V/m incident field at the aperture face. This way the measured induced current can be directly compared with the simulated induced current with 1 V/m incident field. Such induced current at the attachment point between the wire and the cavity floor (with a 50 Ω to represent the internal impedance of the feed structure) can be obtained from measured scattering parameters. The voltage across the load impedance can be computed by

measuring the scattering parameter S_{21}. This parameter is equal to the ratio of the voltage wave received at port 2 due to voltage wave incident at port 1 [50]. This parameter is given by

$$S_{21} = \frac{V_L}{V_1}, \tag{5.1}$$

where V_1 is the voltage input at port 1 of VNA and V_L is the voltage across the 50 Ω load. V_1 can be obtained as [50]

$$V_1 = \sqrt{2Z_0P_{in}}, \tag{5.2}$$

where P_{in} is the power incident at port 1, and Z_0 is the characteristic impedance of the cable in VNA. Substituting equation (5.2) into (5.1), the load voltage can be calculated as [23]

$$V_L = S_{21}\sqrt{2Z_0P_{in}} = S_{21}\sqrt{Z_0P_{VNA}}, \tag{5.3}$$

where P_{VNA} is the power supplied from VNA. The induced current at the attachment point between the wire and the cavity floor with load impedance Z_L at the feed point can be written as

$$I_L = \frac{V_L}{Z_L} = \frac{S_{21}\sqrt{Z_0P_{VNA}}}{Z_L}, \tag{5.4}$$

The VNA power P_{VNA} that gives a desired electric field strength E at the aperture face is given by

$$P_{VNA} = \frac{4\pi r^2|E|^2}{\eta G_t}, \tag{5.5}$$

where r is the distance between the transmitting antenna and the EUT, G_t is the gain of a transmitting antenna, E is the electric field strength, η is the intrinsic impedance of a medium. For 1 V/m field strength at the aperture face of the EUT 1 m away from the transmitting antenna, equation (5.5) can be written as

$$P_{VNA} = \frac{4\pi}{\eta G_t}. \tag{5.6}$$

Substituting equation (5.6) into (5.4), the induced current I_L due to 1 V/m field strength at the aperture face can be obtained by

$$I_L = \frac{S_{21}}{Z_L}\sqrt{Z_0 \frac{4\pi}{\eta G_t}}. \quad (5.7)$$

5.3. Simulation setup

The constructed EUT shown in Figure 5.4 was modeled using in-house CEM code for simulating the experimental measurements. COMSOL [48] was used as a mesh generator for discretizing the EUT, including the wire probe (modeled as a thin strip). Figure 5.6 shows a meshed EUT discretized into triangular patches. The currents on these triangular patches were modeled with first-order LN/QT moment-method basis functions. The maximum dimension of the triangular elements forming the mesh model of the cavity walls was 0.15λ, where λ is the electromagnetic wavelength at the test frequency.

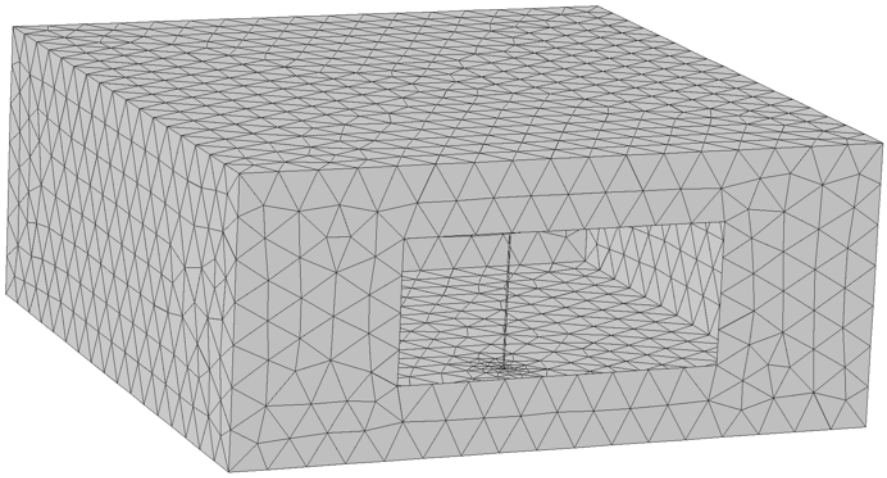

Figure 5.6. EUT triangular patch mesh used at frequencies from 1.75 GHz to 2 GHz.

The illumination was modeled as a single, vertically polarized uniform plane wave normally incident on the EUT face containing the aperture having a magnitude of 1 V/m. The induced current was calculated through a 50 Ω load joining the wire and the cavity floor. The accuracy in the numerical simulation will be more with the refined mesh than unrefined mesh, especially around the aperture face, but compromising the computational time. Figure 5.7 shows two sample meshes

at 1 GHz frequency with one mesh not refined and the other refined on the aperture face. Figure 5.8 shows the simulated result obtained with both the meshes. The maximum difference is 0.98 dB at 540 MHz, which is well within the uncertainty of the physical measurements. Therefore, a non-refined mesh is used on the aperture face hereafter to minimize the computational efforts of a numerical simulation. The frequency range considered is from 300 MHz - 8.5 GHz, sampled at 20 MHz to giving a total of 411 frequency samples.

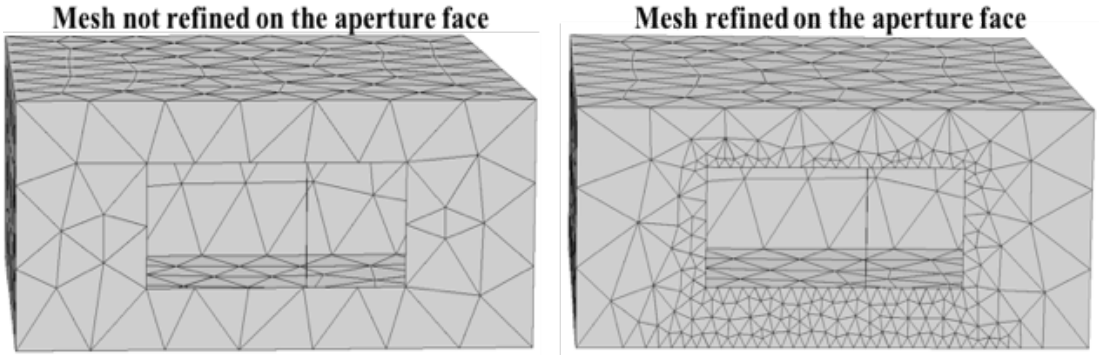

Figure 5.7: Sample COMSOL mesh with 0.15λ maximum dimensions of triangular patch at 1 GHz.

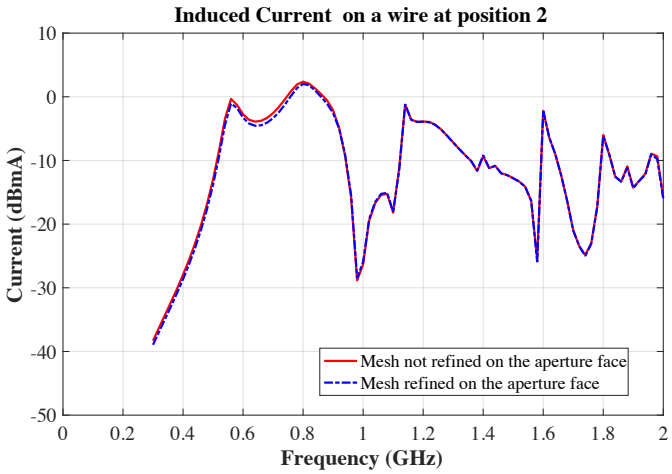

Figure 5.8. Simulated results obtained by using both refined and unrefined mesh on the aperture face.

5.4. Results

5.4.1. Effects of EUT internal dimensions

The modifications in the aperture face of the EUT changes the internal dimension of the cavity from 29.5 cm × 30 cm × 12 cm to 30 cm × 30 cm × 12 cm. This also changes the position of wire probe on the cavity floor from 12 cm to 12.5 cm from the aperture face. While the wire position from the right face of the cavity is still 12 cm. This leads to a change in the geometrical configuration from EUT 1 to EUT2, shown in Table 5.2. Both geometrical configurations have aperture position on the center of the front face and aperture dimension of 15 cm × 6 cm. The induced current at the base of the wire through 50 Ω load for both geometrical configurations of EUT were simulated. The simulated induced current for both EUT configurations are shown in Figure 5.9. Both simulated induced currents showed strong resonant responses.

Table 5.2. EUT geometrical configurations due to different aperture thickness.

Geometrical configuration	Internal cavity dimension	Location of wire position 2
EUT1 (due to thicker aperture face)	29.5 cm × 30 cm × 12 cm	12 cm from the aperture face and right face of the cavity
EUT2 (due to thinner aperture face)	30 cm × 30 cm × 12 cm	12.5 cm from the aperture face 12 cm from the right face of the cavity

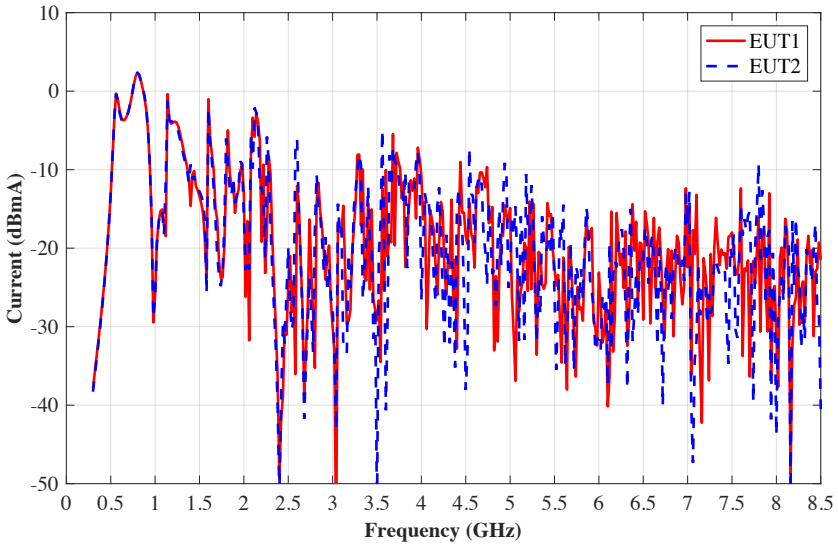

Figure 5.9. Simulated induced current at the base of the wire in both geometrical configuration of EUT.

There are various factors that might contribute these resonances. They are as follows

(a) Cavity formed by the EUT itself.

(b) Wire probe itself forms a monopole antenna and resonant at discrete frequencies.

(c) Aperture itself contributes the resonances.

The resonant frequencies of 29.5 cm × 30 cm × 12 cm cavity, 10.4 cm long wire probe and the aperture having 15 cm × 6 cm dimension, when considering each of them separately, are shown in Figure 5.10. The mutual interaction of the cavity, the wire probe, and the aperture perturb these resonances. For example, first resonance was observed at 707.1 MHz and 721.2 MHz for cavity and wire probe respectively. But the resonances in Figure 5.9 were observed at 560 MHz and 800 MHz.

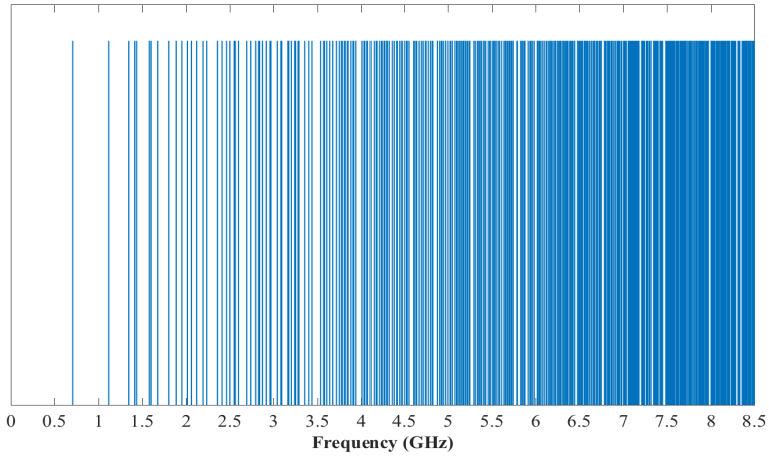

(a)

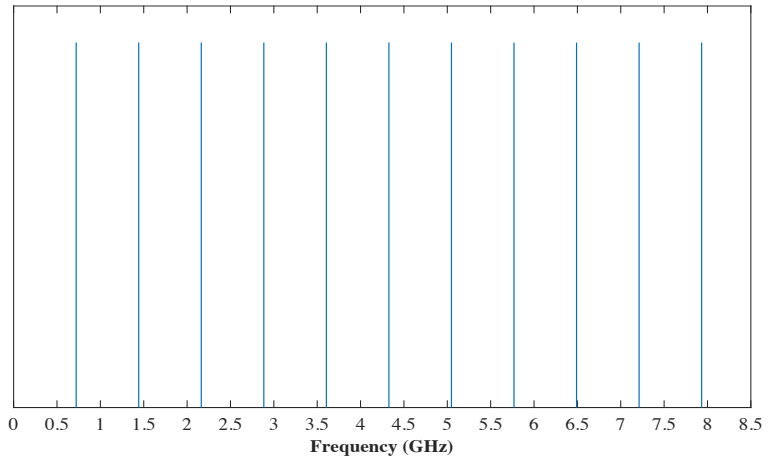

(b)

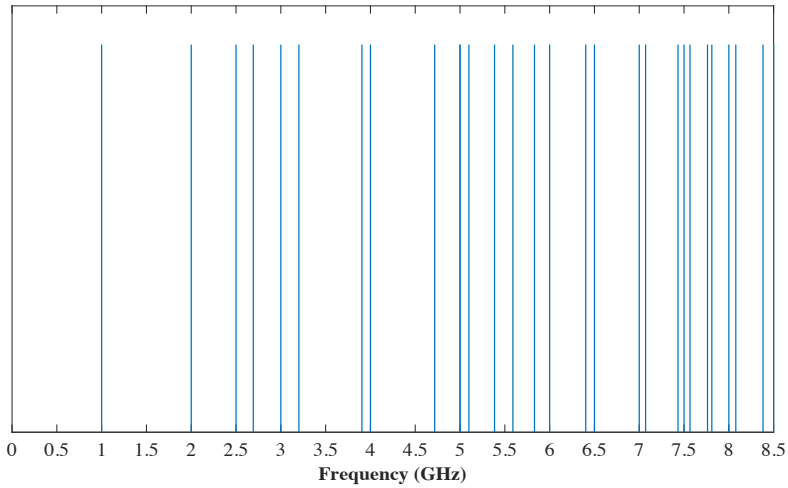

(c)

Figure 5.10. Resonant frequencies due to (a) 29.5 cm × 30 cm × 12 cm cavity, (b) 10.4 cm long wire probe, and (c) 15 cm × 6 cm aperture.

A large number of resonances were observed for the cavity, as shown in Figure 5.10 (a). The resonant frequency of the cavity is given by [51]

$$f_c = \frac{1}{2\pi\sqrt{\mu\varepsilon}}\sqrt{\left(\frac{m\pi}{a}\right)^2 + \left(\frac{n\pi}{b}\right)^2 + \left(\frac{p\pi}{d}\right)^2}, \quad (5.8)$$

where a, b, and d are the length, width and height of a cavity, respectively and μ and ε are the magnetic permeability and electric permittivity of the medium within the cavity, respectively. For TE (transverse electric) modes, m = 0, 1, 2, 3, ..., n = 0, 1, 2, 3, …., p = 1, 2, 3, …. where m = n ≠ 0. For TM (transverse magnetic) modes, m = 1, 2, 3, ..., n = 1, 2, 3, …., p = 0, 1, 2, 3, …. An increase of one of the cavity dimensions from 29.5 cm to 30 cm, therefore, decreases the resonant frequencies of the cavity. Hence, a slight change in a resonant frequency may cause large magnitude differences in the prediction of induced current.

5.4.2. Use of dual-ridge horn and log-periodic as transmitting antenna

The measured current induced through the 50 Ω load at the base of the wire at position 2 was calculated due to a transmitting antenna 1 m away from the EUT. Equation (5.7) was used to calculate the induced current from the measured S_{21}. The measurement was performed by using E5071C VNA. A single antenna was not available that could cover the full 300 MHz to 8.5 GHz frequency band considered in the comparison. Therefore, two different antennas were used. The low frequency range was covered by a log-periodic antenna that operates from 290 MHz to 2 GHz [52]. The upper frequency range was measured using a dual-ridged horn that operates from 700 MHz to 18 GHz [53]. The overlap of the operating bands of the two antennas allows the responses to be spliced together to yield a continuous measurement of the current induced on the EUT probe across the full frequency band. Figure 5.11 shows the frequency response of the antenna gain of log-periodic and dual ridge horn. The antenna gains were read from the manufacturer's datasheets.

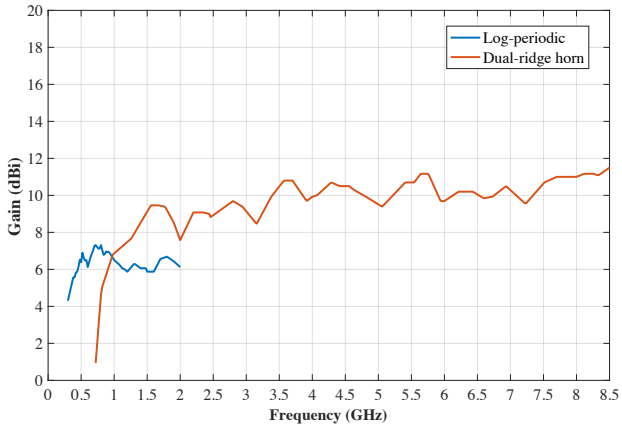

Figure 5.11. Frequency dependence of the test antenna gain as read from the manufacturer's data sheets [52] [53].

Figure 5.12 shows the current induced through the 50 Ω load at the base of the wire as measured using both the log-periodic and dual-ridge horn antennas. Very good agreement is observed in the frequency range from 900 MHz to 2 GHz where both antennas are operating within their design bandwidth. Therefore, the two measurements were spliced together at 1.5 GHz, using log-periodic antenna results below 1.5 GHz and the dual-ridged horn antenna results above 1.5 GHz.

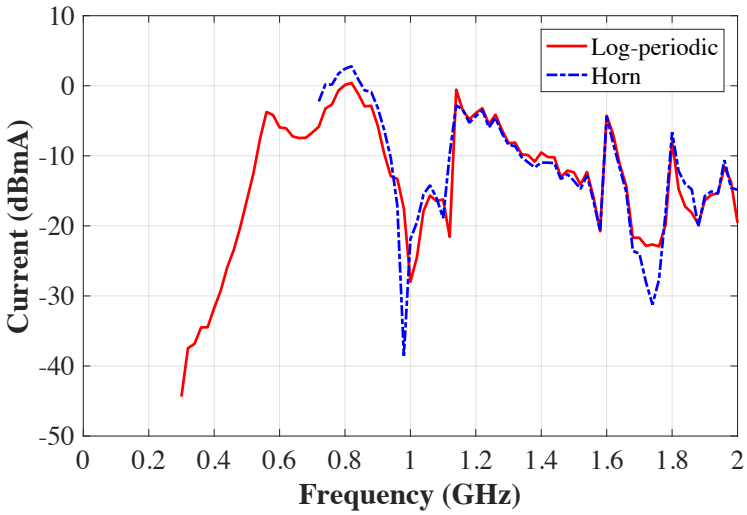

Figure 5.12. Induced current at the wire base derived from the measurements using two different antennas.

5.4.3. Comparison between measured and simulated results

5.4.3.1. Wire at position 2

Figure 5.13 compares measured and simulated currents at the wire base when the wire is at position 2, illustrated in Figure 5.5 and Table 5.1, through the 50 Ω load (to representing the load impedance of the VNA port connected between the wire and the cavity floor). The first resonance, observed at 560 MHz, appears 3.4 dB more strongly in the simulation than in the measurements. The EUT was only 1 m away from the transmitting antenna, and the wavelength at that frequency is 54 cm. Therefore, the difference in magnitude may be due to the antenna being less than two wavelengths from the EUT so that the far-field conditions were not met in the measurements, as discussed in [3].

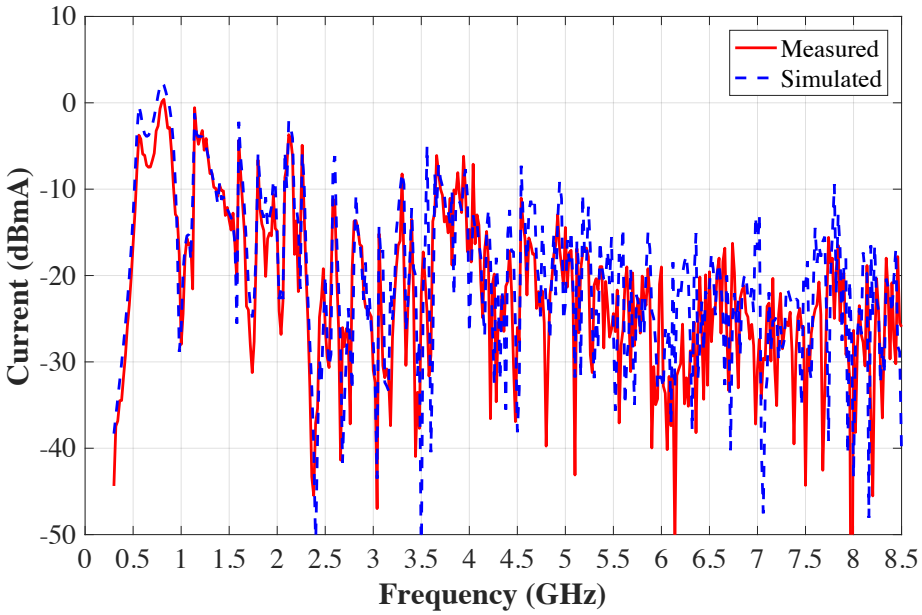

Figure 5.13. Induced current at the base of the wire at position 2.

The simulated and measured results in Figure 5.13 show very good agreement below 3.5 GHz. The resonances and nulls are aligned at the same frequency and the magnitudes of resonances are predicted to within 3.6 dB. Maximum errors in the resonance strengths occurred at 560 MHz, 800 MHz, 2.58 GHz and 2.82 GHz, with differences of 3.4 dB, 2.25 dB, 3.55 dB and 3.02 dB,

respectively. As observed above, resonance strengths are highly dependent on changes in the geometry of the EUT. The observed resonance-strength differences are therefore consistent with the unavoidable small differences between the physical and simulated EUT geometries. Better overall agreement between the measured and the simulated results over the 3.5 GHz - 4.5 GHz band is observed here than in Figure 5.3.

Figure 5.14 shows the feature selective validation (FSV) [25] comparison of the measured and the simulated results in Figure 5.13. The overall FSV assessment is shown in Table 5.3. The agreement in ADM and FDM is good, and fair in GDM. GDM (which combines both ADM and FDM) gives the greatest disagreement (higher FSV value) over the frequency range from 6.94 GHz to 7.12 GHz and 7.96 GHz to 8.06 GHz. Figure 5.10 suggested that there are very narrow resonances in that frequency range that occur more frequently than the 20 MHz sampling rate used in Figure 5.13. It is, therefore, possible that the magnitudes of some resonances were not fully detected or that resonances were completely missed in both numerical simulation and the measurements. Figure 5.15 [54] (same as Figure 3.8) shows the induced current at 5.2 mm above the base of the wire at position 2 within a cavity of internal dimension 29.5 cm × 30 cm × 12 cm. It shows that several resonances and nulls were indeed entirely missed at the 20 MHz sampling rate.

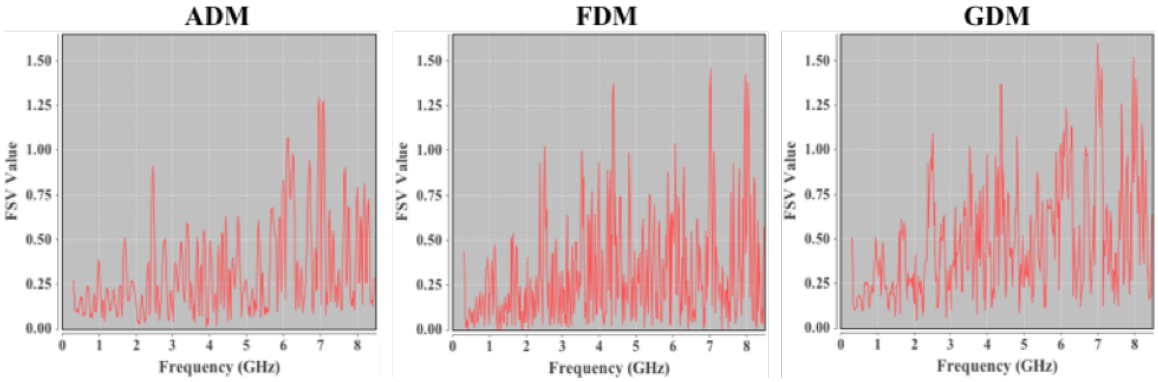

Figure 5.14. FSV analysis for the comparison between measured and the simulated results shown in Figure 5.13.

Table 5.3. FSV overall assessment for the comparison between measured and simulated results in Figure 5.13.

ADM	0.3208 (Good)
FDM	0.3171 (Good)
GDM	0.4921 (Fair)

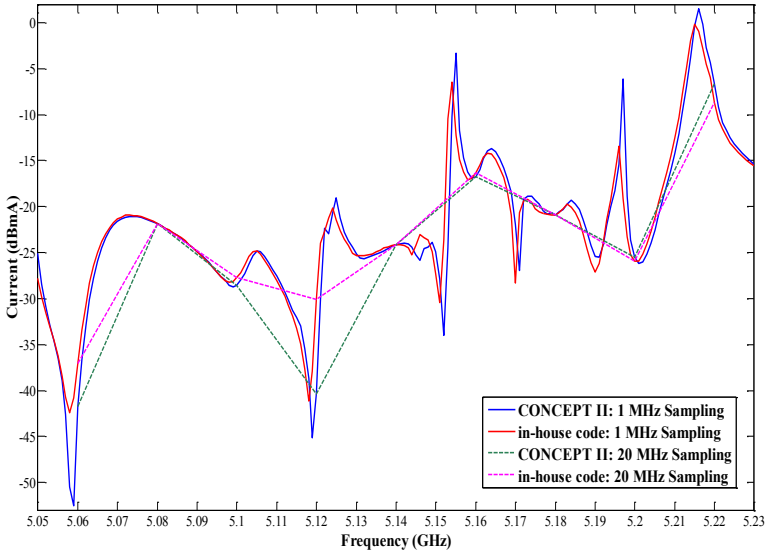

Figure 5.15. Induced current on the wire at position 2 within a cavity of internal dimensions 29.5 cm × 30 cm × 12 cm [54].

FSV overall assessment was also shown in Table 5.4 for the comparison between the measured and the simulated results in Figure 5.3. It was found that ADM score decreases from 0.4584 to 0.3208 and hence improve the ADM assessment from fair to good agreement. FDM and GDM score drops from 0.372 to 0.3171 and 0.6467 to 0.4921, respectively, which shows that there is some improvement in both FDM and GDM agreement as well. Therefore, FSV gives a better comparison between the measured and simulated results of Figure 5.13 than that of Figure 5.3. The improvement in the FSV agreement supports the conclusion that the thick aperture face used in [3]

introduces an aperture resonance that led to a poorer agreement between the measurements and simulations in 3.5 GHz to 4.5 GHz frequency range.

Table 5.4. FSV overall assessment for the comparison between measured and simulated results in Figure 5.3.

ADM	0.4584 (Fair)
FDM	0.372 (Good)
GDM	0.6467 (Fair)

5.4.3.2. Wire at other position

The induced current was also found for wire at position 1 and position 3 of Figure 5.5 using both measurement and numerical simulation. Comparisons between the measured and simulated results are shown in Figure 5.16 and Figure 5.17 for the wire at position 1 and 3, respectively. Similar agreement to that observed with wire position 2 are observed at both new wire positions across the entire frequency band. The FSV overall assessments for wire position 1 and wire position 3 are presented in Table 5.5 and Table 5.6, respectively.

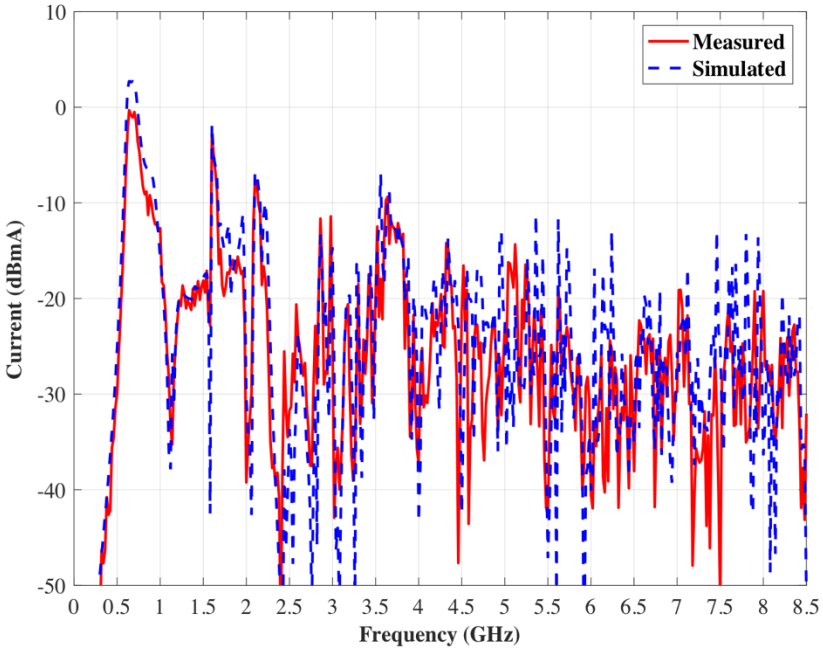

Figure 5.16. Induced current at the base of the wire at position 1.

Table 5.5. FSV overall assessment for the comparison between measured and simulated results in Figure 5.16

ADM	0.3223 (Good)
FDM	0.3477 (Good)
GDM	0.5212 (Fair)

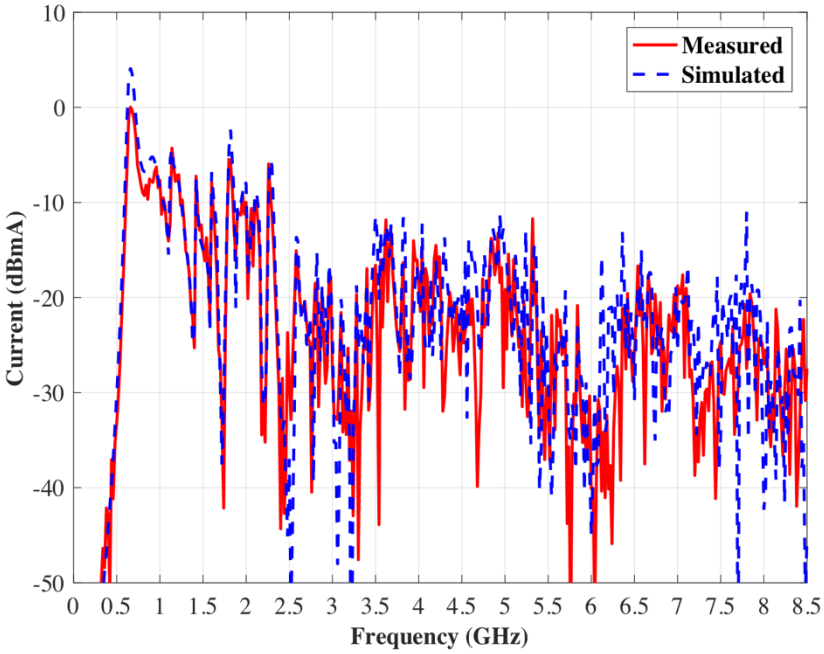

Figure 5.17. Induced current at the base of the wire at position 3.

Table 5.6. FSV overall assessment for the comparison between measured and simulated results in Figure 5.17.

ADM	0.3355 (Good)
FDM	0.3637 (Good)
GDM	0.5431 (Fair)

Tables 5.3, 5.5, and 5.6 show that the agreement between the measured and simulated currents is good in ADM and FDM, and fair in GDM for all wire positions. Therefore, the agreement between the measured and the simulated results are similar for all three wire positions. The similarity in the FSV agreement confirms that the differences in the measured and simulated results are due to the geometrical differences between the physical and simulation model, and the use of SMA connector in the measurements.

5.5. Conclusion

The induced currents on a wire probe found using an in-house MLFMA computational electromagnetics package enhanced to use first-order LN/QT basis functions to model the induced current has been validated against measurements performed within an anechoic chamber. Both simulated and measured currents were compared over a frequency range of 300 MHz to 8.5 GHz for three different wire positions within the cavity. Both ADM and FDM shows good agreement between the measured and simulated currents over the entire frequency range for all three wire locations. The validity of the numerically simulated results has been confirmed for the initial test case that exposes the EUT to a single uniform plane wave that is normally incident on the face of the EUT that contains the aperture. In the next chapter, the current induced at the base of the wire when the EUT is exposed to a random field is analyzed using numerical simulation with LN/QT basis functions. The calculated currents are again validated through comparison with measurements performed within a reverberation chamber that yields a random field.

CHAPTER 6

VALIDATION OF NUMERICAL SIMULATION APPROACH AGAINST REVERBERATION CHAMBER MEASUREMENTS

In the previous chapter, the enhancement of an electromagnetics package developed in-house to use first-order basis functions was validated by measurement within an anechoic chamber. The test case was the current induced at the attachment point between a wire and the floor of a partially shielding cavity that serves as an equipment under test (EUT) due to an external excitation source. The excitation source consisted of a single, vertically polarized uniform plane wave normally incident on the EUT face containing the aperture. The fabricated EUT is shown in Figure 5.4. Three different wire positions on the cavity floor were considered as shown in Figure 5.5. The Frequency Selective Validation (FSV) package [25] was used to assess the similarities between the measured and simulated induced currents. Both ADM and FDM showed good agreement between the measured and simulated currents over the entire frequency range from 300 MHz to 8.5 GHz for all three wire positions. Hence, Chapter 5 concluded with the validation of the numerically simulated results for this test case.

In this chapter, the same EUT is used to validate the numerical simulation of the EUT response within a reverberation chamber against measurement. The enhanced CEM code is again used to perform the numerical calculations. The current induced at the base of the EUT wire probe due to the random reverberation chamber field is again examined and the three wire positions on the cavity floor shown in Figure 5.5 are again considered. The random field within a chamber was numerically modeled using the discrete plane-wave spectral representation presented in [19].

6.1. Overview of test case used for validation

The validation of the numerical approach was performed by considering the induced probe current when the EUT was exposed to a random field within the reverberation chamber having an RMS level of 1 V/m. The frequency response of the EUT was found over a 300 MHz to 6 GHz band. Measurements were performed within a ETS-Lindgren SMART^{TM} 80 reverberation chamber. The test configuration is shown in Figure 6.1. Included are a transmitting antenna, the EUT, and two Z-shaped tuners (vertically and horizontally aligned) that are used to stir the random reverberation chamber field. The chamber has internal dimension of 6.15 m × 13.2 m × 4.95 m. The EUT was placed within the working volume of the chamber and with the aperture oriented away from the transmitting antenna. Mechanical stirring of the fields was achieved by rotating vertical tuner during the measurements, giving random independent samples of EUT response. The horizontal tuner was held at stationary. The transmitting antenna was pointed toward the static horizontal tuner to minimize the direct power coupling between the transmitting antenna and the EUT during testing. Figure 6.2 shows the experimental configuration within the reverberation chamber. Either a log-periodic (shown in Figure 6.2) or a dual-ridge horn may be used as a source antenna.

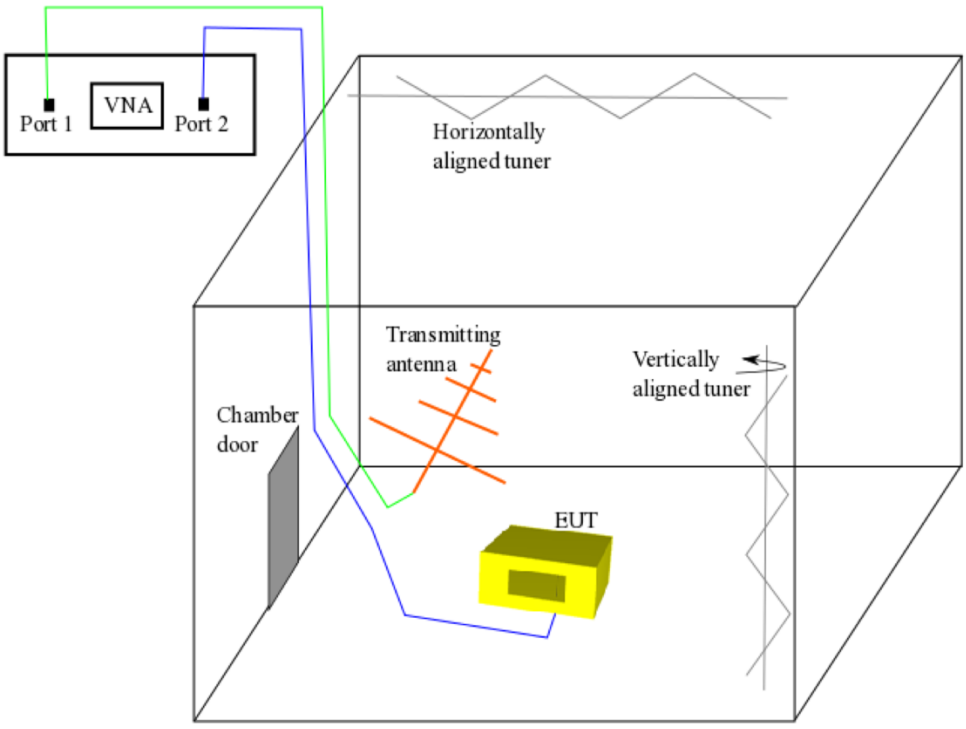

Figure 6.1. Measurement setup in SMART^{TM} 80 reverberation chamber.

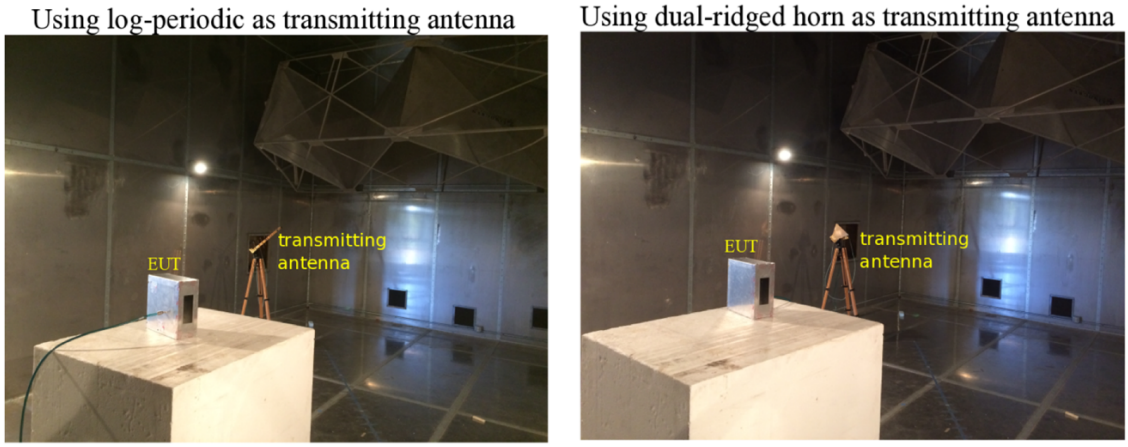

Figure 6.2. Experimental configuration using log-periodic and dual-ridged horn source antennas.

The magnitude of the current induced on the EUT at the test point (attachment point between the wire and cavity) by a random field was averaged over 70 tuner positions. As discussed in Section

5.2, the induced current at the test point can be obtained from the measured scattering parameters (S_{21}) between the transmitting antenna and the EUT measurement port. The measured S_{21} was obtained by connecting Port 1 of VNA to transmitting antenna and Port 2 of VNA to wire inside the aperture box (EUT) through SMA connector. The measurement was performed over a frequency range from 300 MHz to 6 GHz sampled at 14.12 MHz, giving 401 frequency sample points.

Both the match efficiency of the transmitting antenna and of the quality factor of the chamber were also measured. These quantities are used to find the power transmitted into the chamber that maintains the desired RMS chamber field of 1 V/m, as described below. The measured random samples were collected from 70 different vertical tuner positions. Final validation of the model is performed by comparing the mean induced current magnitude found from the 70 measurements with the mean current predicted from the numerical model using 70 independent samples of the random chamber field. The comparisons were performed for the three different wire positions of Figure 5.5.

6.2. Formulation for calculating EUT response to a stirred, random field

Hill [15] showed that the magnitude of the current induced on the test object due to an ideally random, mechanically stirred reverberation chamber field follows the Rayleigh distribution. As discussed in the previous section, the mean induced current magnitude due to a random field at the attachment point between the wire and the cavity floor was considered as the EUT response. This section is split into two parts. Section 6.2.1 describes the approach for representing the random field within a reverberation chamber. The procedure for obtaining the induced current statistics due to a random field was discussed in Section 6.2.2.

6.2.1. Modeling of random field within a reverberation chamber

Hill [15] shows that the ideal random field can be represented by the integral of continuous plane wave spectrum over the sphere, which is given by

$$\mathbf{E}(\mathbf{r}) = \iint \mathbf{F}(\Omega) e^{j\mathbf{k}\cdot\mathbf{r}} d\Omega \,, \tag{6.1}$$

where $\mathbf{E}(\mathbf{r})$ is the electric field at a point $\mathbf{r}$ inside the chamber, $\mathbf{k} = k\,(\hat{a}_x \sin\theta \cos\phi + \hat{a}_y \sin\theta \sin\phi + \hat{a}_z \cos\theta)$ is the vector wave number and k is the scalar wavenumber, $d\Omega$ is the solid angle, θ and ϕ are the elevation and azimuth coordinates in spherical coordinate system, respectively. $\mathbf{F}(\Omega)$ is the angular spectrum given by

$$\mathbf{F}(\Omega) = \hat{a}_\alpha F_\alpha + \hat{a}_\beta F_\beta \,, \tag{6.2}$$

where $\hat{a}_\alpha$ and $\hat{a}_\beta$ are the unit vectors that are orthogonal to each other and to $\mathbf{k}$, F_α and F_β are the complex numbers. As discussed in Section 1.2.2, the approach used by West *et al.* [19] for approximating Equation (6.1) using a finite number of plane waves is computationally efficient compared to the approach used by Musso [17] and Moglie [18]. Equation (6.1) can be discretized into a fixed sampling of integral with θ sampled at L zeros of the Legendre polynomial $P_L(\cos\theta)$ and ϕ sampled at 2L uniformly spaced points [19]. Thus, equation (6.1) can be written in a discretized form as [19]

$$\mathbf{FE}(\mathbf{r}) = \sum_{l=1}^{L} \sum_{m=1}^{2L} \mathbf{F}_{lm} e^{j\mathbf{k}_{lm}\cdot\mathbf{r}} \,, \tag{6.3}$$

where $\mathbf{k}_{lm} = k\,(\hat{a}_x \sin\theta_l \cos\phi_m + \hat{a}_y \sin\theta_l \sin\phi_m + \hat{a}_z \cos\theta_l)$, $\cos\theta_l$ is the l^{th} zero of $P_L(\cos\theta)$ and $\phi_m = m\pi/L$. $\mathbf{F}_{lm}$ is the complex and vector random variable given by

$$\mathbf{F}_{lm} = \hat{a}_\alpha \tilde{F}_{lm,\alpha} + \hat{a}_\beta \tilde{F}_{lm,\beta} \,, \tag{6.4}$$

where $\tilde{F}_{lm,\alpha}$ and $\tilde{F}_{lm,\beta}$ are the randomly assigned complex numbers. Their real and imaginary part follows the normal distribution for an ideally stirred reverberation chamber [19]. This normal distribution N (μ, ν) has a mean value (μ) of zero and a variance given by

$$\nu = w_l \frac{{E_0}^2}{16L}, \tag{6.5}$$

where $E_0 = \sqrt{\langle |\mathbf{E}(\mathbf{r})|^2 \rangle}$ is the desired RMS field within the chamber and w_l is the Gauss-Legendre quadrature weighting associated with θ_l.The statistics of the random field are met over the EUT when the plane-wave spectrum sampling parameter meets [19]

$$L \geq k(D + \lambda)/2\,, \tag{6.6}$$

where D is the maximum dimension of the EUT and λ is the wavelength. The induced current at test point q in EUT can be obtained using [19]

$$I_q = \mathbf{L_q}[\mathbf{E}(\mathbf{r})]\,, \tag{6.7}$$

where $\mathbf{L_q}[\,]$ is an admittance operator which is linear when the EUT contains no nonlinear material. Substituting equation (6.3) into (6.7), current at test point q is given by

$$I_q = \sum_{l=1}^{L} \sum_{m=1}^{2L} \left\{ \tilde{F}_{lm,\alpha} \mathbf{L_q}[\hat{a}_\alpha e^{j\mathbf{k}_{lm}\cdot\mathbf{r}}] + \tilde{F}_{lm,\beta} \mathbf{L_q}[\hat{a}_\beta e^{j\mathbf{k}_{lm}\cdot\mathbf{r}}] \right\}, \tag{6.8}$$

$$= \sum_{l=1}^{L} \sum_{m=1}^{2L} \left\{ \tilde{F}_{lm,\alpha} I_{lm,\alpha} + \tilde{F}_{lm,\beta} I_{lm,\beta} \right\}, \tag{6.9}$$

where $I_{lm,\alpha}$ and $I_{lm,\beta}$ are the currents induced at the test point q due to single uniform planes wave of unity magnitude having a polarization vector along the direction $\hat{a}_\alpha$ and $\hat{a}_\beta$, respectively. For simplicity, we set $\hat{a}_\alpha = \hat{a}_\theta$ (giving a plane wave with "vertical polarization") and $\hat{a}_\beta = \hat{a}_\phi$ (giving a plane wave with "horizontal polarization").

6.2.2. Induced current statistics due to a random field

In the previous chapter, the induced current at the test point due to a single uniform plane wave was obtained by solving the electric field integral equation (EFIE) using MLFMA with the plane wave as the source, i.e. the "forward problem". However, (6.9) requires that the induced current at the test point be calculated due to all plane waves having direction determined by Legendre/uniform

sampling for each polarization. This requires the EFIE to be solved $4L^2$ times, once for each plane wave excitation. Hence, calculating the induced current at the test point due to a random field by solving the forward problem will be computationally expensive. For this reason, the reciprocal approach of [20] was used to calculate the induced currents at the test point. By exploiting the principle of reciprocity, the current response at a test point due to individual plane wave can be computed by placing a voltage $V_t = 4\pi/jk\eta$ at the test point and then computing $\mathbf{E}_{far}.\hat{a}_p$, where E_{far} is the far-field electric field in the direction from which the plane wave originated, $\hat{a}_p$ is the polarization of the plane wave, k is the wave number, and η is the intrinsic impedance of the medium filling the chamber (air in this case). Using this principle, the simulation needs to be run only once, considerably reducing the computational time. A test case was first considered to ensure the validity of the reciprocal approach. In this test case, a single, vertically polarized uniform plane wave of 1 V/m magnitude was normally incident on the EUT face containing the aperture (the same case described in Section 5.1). The induced current was calculated at the test point over a frequency range from 300 MHz to 6 GHz. The test point is the wire attachment point at position 2 of Figure 5.5. Figure 6.3 shows the induced current obtained by solving both the forward problem and the reciprocal problem. Excellent agreement is achieved at all frequencies. This confirms the validity of reciprocal approach of calculating induced current. Hence, the reciprocal approach will be used hereafter to calculate the induced currents at the test points.

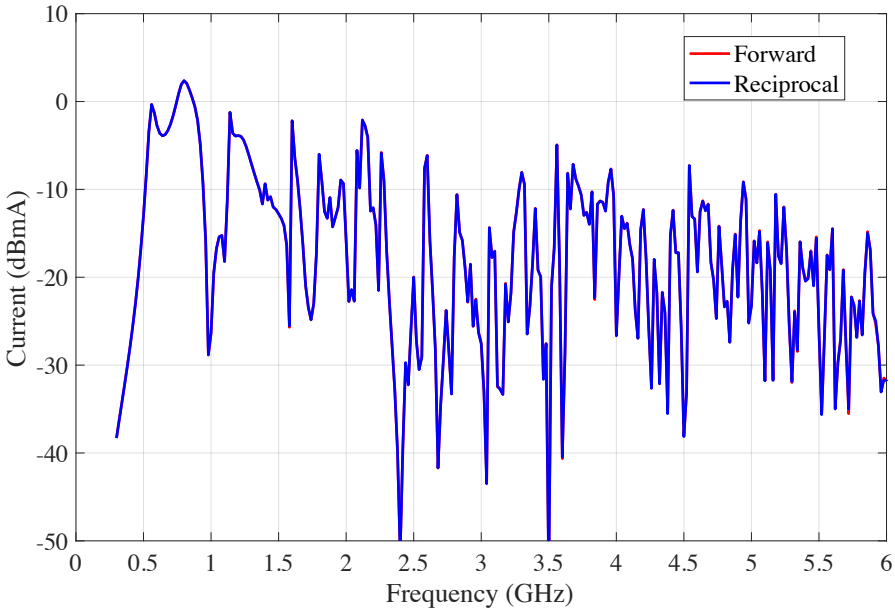

Figure 6.3. Current induced on the wire at position 2 using forward and reciprocal approach.

The current at the test point induced by unity magnitude uniform plane waves incident from the $2L^2$ Legendre/uniform sampling angles and at both vertical and horizontal polarization (for a total of $4L^2$ responses) was found at each frequency. The sampling parameter L in equation (6.6) varied from 5 at 300 MHz to 31 at 6 GHz. The sample current responses at the test point due to the random chamber field were obtained by the superposition of all plane wave responses, individually weighted by the coefficient, $\tilde{F}_{lm,\alpha}$ and $\tilde{F}_{lm,\beta}$, as shown in equation (6.9). In [20], Monte-Carlo simulation was performed to generate the independent current samples by randomly assign a complex Gaussian random number to the coefficients of plane wave response. Using Monte-Carlo simulation, 70 random samples of the current induced at the test point were obtained and the mean induced current magnitude was found from the average of all current sample magnitudes.

6.3. Calculation of EUT response using measured S_{21}

The VNA used to perform the measurements within the reverberation chamber finds the S_{21} scattering parameter between the source antenna feed the SMA measurement port on the VNA. These measurements can be used to find the current induced at the wire probe base by a random chamber field as follows. As discussed in Section 5.2, the induced current at the attachment point between the wire and the cavity floor with a load impedance Z_L at the feed point due to an incident single plane wave can be written as

$$I_L = \frac{S_{21}\sqrt{Z_0 P_{VNA}}}{Z_L}, \tag{6.10}$$

where Z_0 is the characteristic impedance of the cable in VNA and P_{VNA} is the power supplied from VNA. Similarly, the mean induced current magnitude at same test point is obtained by

$$\langle |I_L| \rangle = \frac{\langle |S_{21}| \rangle \sqrt{Z_0 P_{VNA}}}{Z_L}, \tag{6.11}$$

where $|S_{21}|$ is the magnitude of S_{21}, and $\langle |S_{21}| \rangle$ is the ensemble average (or mean) of $|S_{21}|$ measured over 70 different tuner positions. The power transmitted into the chamber (P_t) is related to the power supplied by the VNA (P_{VNA}) by

$$P_t = P_{VNA}\left(1 - |S_{11}^{FS}|^2\right), \tag{6.12}$$

where S_{11}^{FS} is the reflection coefficient of the transmitting antenna in free space. The chamber RMS field is found from the transmitted power through [15]

$$E_0 = \sqrt{\frac{QP_t}{\omega \epsilon V}}, \tag{6.13}$$

where Q is the chamber quality factor, P_t is the power transmitted into a chamber, V is the volume of the chamber, ϵ is the permittivity of a medium within the chamber and ω is the angular frequency. Therefore, an RMS field level (E_0) equal to 1 V/m requires a transmitter power of

$$P_t = \frac{\omega \epsilon_0 V}{Q}. \tag{6.14}$$

Substituting equation (6.14) and (6.12) into equation (6.11), the mean induced current due to a 1 V/m RMS random chamber field is given by

$$\langle |I_L| \rangle = \frac{\langle |S_{21}| \rangle}{Z_L} \sqrt{\frac{Z_0 \omega \epsilon_0 V}{Q\left(1 - |S_{11}^{FS}|^2\right)}}. \tag{6.15}$$

Equation (6.15) requires two additional measured terms, the input reflection coefficient of the source antenna S_{11}^{FS} and the chamber quality factor Q.

6.3.1. Reflection coefficient of the transmitting antenna

The reflection coefficient (S_{11}^{FS}) of the log-periodic and dual-ridged horn transmitting antennas used in the measurements were measured in the anechoic chamber. Figure 6.4 shows the measured reflection coefficient of both antennas. The operating frequency bands of the log-periodic and dual-ridge horn antennas are 290 MHz – 2 GHz and 700 MHz – 18 GHz. Better match efficiency was observed with the dual-ridge horn antenna above 900 MHz. Therefore, the measured S_{11}^{FS} from the antennas were spliced at this frequency to cover the full frequency band from 300 MHz to 6 GHz.

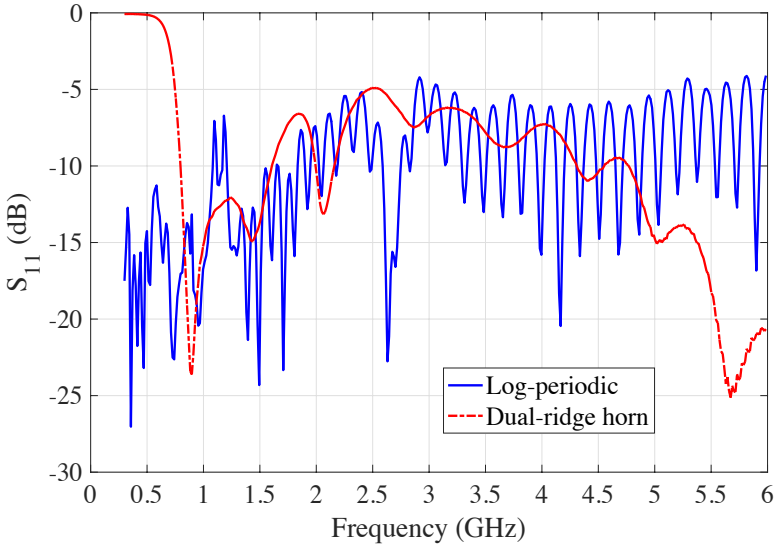

Figure 6.4. Measured free space reflection coefficient of the transmitting antenna

6.3.2. Quality factor measurement of the reverberation chamber

The quality factor of a chamber is defined as the total energy stored over total energy dissipated in a cycle within the chamber. Figure 6.5 shows the Q measurement setup with two dual-ridged horn antennas in the SMART^{TM} 80 reverberation chamber. S_{21} between the two antennas was measured at 70 different tuner positions. The quality factor (Q) of the reverberation chamber at each frequency is typically calculated by [55]

$$Q = \frac{16\pi^2 V}{\lambda^3}\langle|S_{21}|^2\rangle\,, \tag{6.16}$$

where V is the volume of the reverberation chamber, λ is the wavelength and $\langle|S_{21}|^2\rangle$ is the ensemble average of magnitude square of the measured S_{21} over the 70 tuner positions. Holloway *et al.* [14] suggested that the antenna efficiency due to impedance mismatch must be taken into an account while characterizing the Q of the chamber. Hence equation (6.16) is modified as

$$Q = \frac{16\pi^2 V}{\lambda^3}\frac{\langle|S_{21}|^2\rangle}{\eta_t\eta_r}, \tag{6.17}$$

where η_t and η_r are the mismatch efficiencies of the transmitting and receiving antennas, respectively. The transmitting antenna and received antennas were connected to port 1 and port 2 of the VNA, so these efficiencies are given by

$$\eta_t = 1 - \left|S_{11}^{FS}\right|^2, \tag{6.18a}$$

$$\eta_r = 1 - \left|S_{22}^{FS}\right|^2, \tag{6.18b}$$

where S_{11}^{FS} and S_{22}^{FS} are the measured reflection coefficients of antennas in free space. Q was measured over the frequency range of 300 MHz to 6 GHz at 14.12 MHz increments, giving 401 frequency sample points. Both the transmitting and receiving antennas must be within their operating frequency bands when performing the Q measurement. When two identical antennas are used to perform the measurement, $\eta_t = \eta_r$ and equation (6.17) can be written as

$$Q = \frac{16\pi^2 V}{\lambda^3}\frac{\langle|S_{21}|^2\rangle}{{\eta_t}^2}\,, \tag{6.19}$$

The Q measurement was performed with two identical dual-ridge horn antennas for frequencies above 900 MHz. At the time of measurement, only a single log-periodic antenna was available, so a quality factor measurement using two identical antennas could not be performed below 900 MHz. Hence, the quality factors measured in earlier work [13], shown in Table 6.1, was used in this frequency range. Linear interpolation was used at frequencies between those shown in the table. The measured quality factor ($Q_{measured}$) as a function of frequency is shown in Figure 6.6.

Table 6.1. Measured quality factor using time domain method, presented in [13]

Frequency (MHz)	Quality factor (dB)
400	40.29
500	41.9
600	43.06
700	43.52
800	44.36

Figure 6.5. Quality factor measurement using two dual-ridged horn antennas

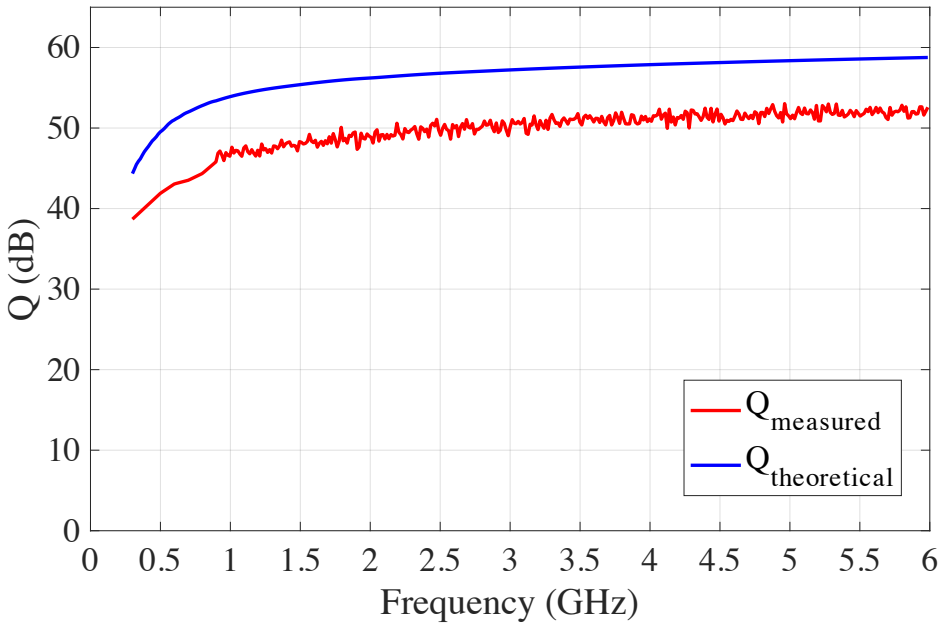

Figure 6.6. Quality factor (Q) of SMART™ 80 reverberation chamber

Hill [35] theoretically derived the quality factor of a cavity associated with the wall losses and antenna loading. The quality factor of a cavity due to a circular aperture and the presence of absorbing material was also discussed. The quality factor associated with the losses highly conducting walls is given by [35]

$$Q_1 = \frac{3V}{2\mu_r S\delta}\,, \tag{6.20}$$

where S is the cavity surface area, δ is the wall skin depth, and μ_r is the wall relative permeability. The walls of the SMART™ 80 reverberation chamber are made up of galvanized steel, so the conductivity of zinc was used. The quality factor associated with the antenna loading is given by [35]

$$Q_2 = \frac{16\pi^2 V}{\eta_A \lambda^3}\,, \tag{6.21}$$

where η_A is the antenna mismatch efficiency. For two identical transmitting and receiving antenna within a cavity, equation (6.21) can be modified as

$$Q_2 = \frac{8\pi^2 V}{\eta_A \lambda^3}. \tag{6.22}$$

The overall theoretical quality factor ($Q_{theoretical}$) due to antenna loading and wall losses is given by [35]

$$\frac{1}{Q_{theoretical}} = \frac{1}{Q_1} + \frac{1}{Q_2}. \tag{6.23}$$

Figure 6.6 shows the overall theoretical quality factor ($Q_{theoretical}$). The steep slope in both $Q_{measured}$ (obtained by using equation (6.19)) and $Q_{theoretical}$ at lower frequencies is due to antenna loading. $Q_{measured}$ is approximately 6 dB lower than the $Q_{theoretical}$. A possible reason is the losses associated with tuner structure, which was not incorporated into theoretical quality factor, Additionally, uncertainties in the conductivities of chamber wall and leakage of energy through imperfectly shielded points on the chamber enclosure prevent exact knowledge of the theoretical quality factor. Both curve shows a similar amplitude trend over the entire frequency band. Thus, $Q_{measured}$ was considered to derive the current response at the EUT measurement port.

6.4. Transmitting antenna used in the measurements

The overlap of the operating bands of the two antennas allows the responses to be spliced together to yield a continuous measurement of the mean induced current across the full frequency band. Figure 6.7 shows the mean current induced at the measurement port, given by (6.15), as measured using both the log-periodic and dual-ridge horn antennas. Very good agreement is achieved over the frequency band from 700 MHz to 2 GHz where the antenna operating bands overlap. Therefore, the two measurements were spliced together at 900 MHz, using log-periodic antenna results below 900 MHz and the dual-ridged horn antenna results above 900 MHz.

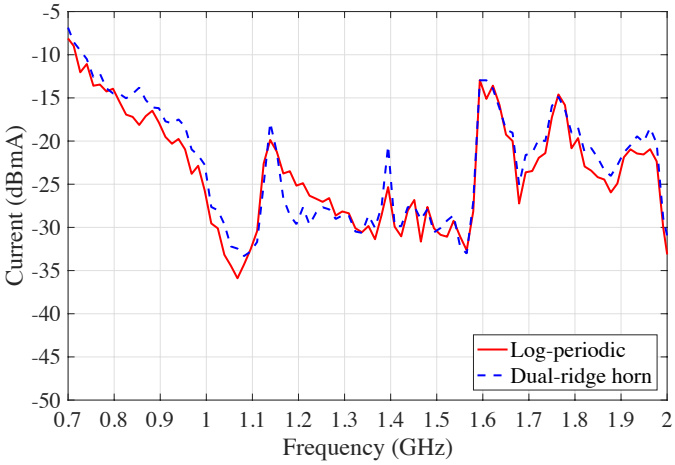

(a) Wire position 1

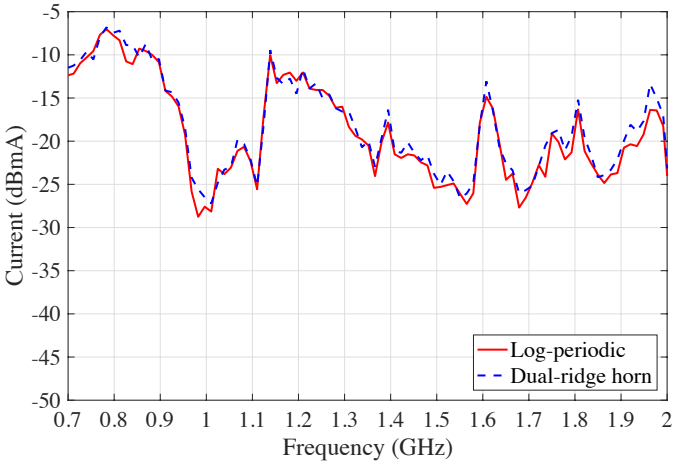

(b) Wire position 2

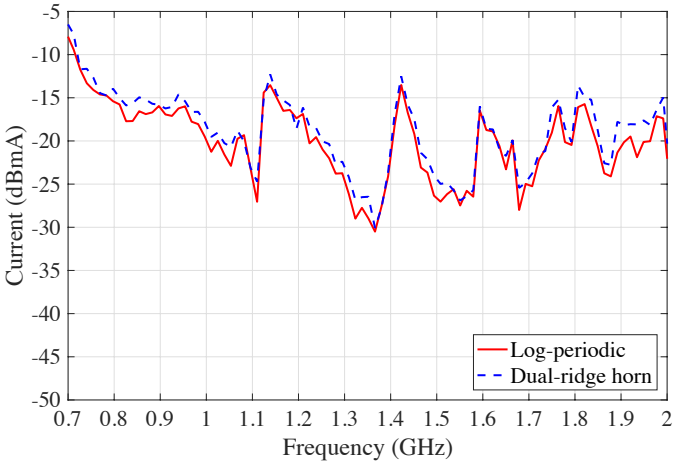

(c) Wire position 3

Figure 6.7. Measured mean current at the wire base obtained with two different source antennas.

6.5. Repeatability of the measured EUT response

The EUT response was measured for three different aperture box orientations, as shown in Figure 6.8. “EUT Orientation 2” in Figure 6.8 was similar to the orientation of the EUT in Figure 6.2. Referring to Figure 6.1, the aperture face of the EUT was pointed toward the chamber door for “EUT Orientation 1” and toward the vertical tuner for “EUT Orientation 3”. Figure 6.9 shows the measured induced current at position 2 for three different EUT orientations. Very good agreement is observed, showing that the measured EUT response is not significantly affected by the orientation of EUT. This confirms that the chamber field is sufficiently stirred when rotating only the vertical tuner within the measured frequency band.

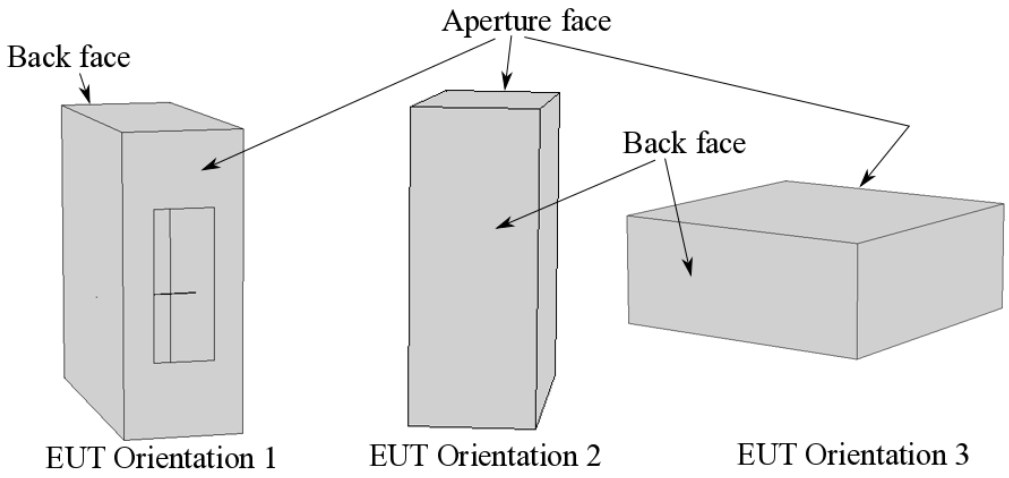

Figure 6.8. EUT orientation considered in the measurement repeatability test.

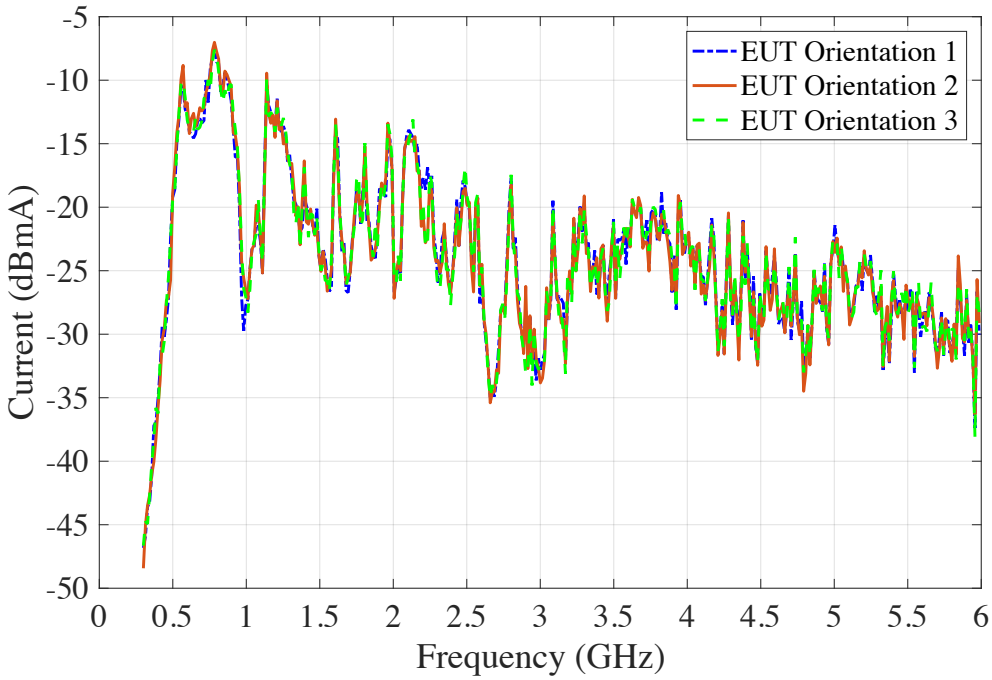

Figure 6.9. Measured induced current at the wire base for three different EUT orientations.

6.6. Comparison of simulated and measured results

Figure 6.10 shows a comparison of measured and simulated mean induced current magnitudes at the wire base for all three different wire positions. The measured and simulated currents show good agreement across the frequency band for all wire positions, including at the frequencies of all resonant peaks and nulls. The primary observed differences between the measured and simulated currents are the strengths of the resonant peaks. For example, the resonant peaks appear more strongly in the measurements than in the simulation from 4 GHz to 4.5 GHz with wire position 2 (Figure 6.10 (b)), and the converse is true (resonant peaks appear stronger in the simulation than in the measurements) from 4.7 GHz to 5 GHz with wire positions 1 (Figure 6.10 (a)) and 2 (Figure 6.10 (b)) and from 3 GHz to 3.5 GHz with wire position 3 (Figure 6.10 (c)). Chapter 3 shows that the resonant response magnitudes and frequencies are extremely sensitive to small change in the EUT geometry. Therefore, such magnitude differences are expected due to the geometrical differences between the physical model and the simulation model of EUT.

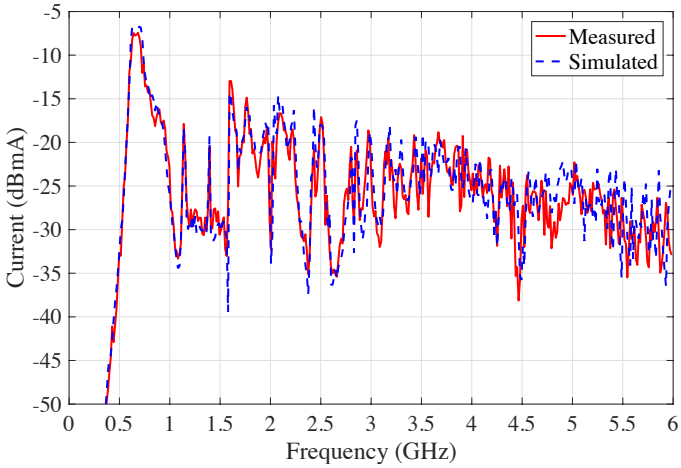

(a) Wire position 1

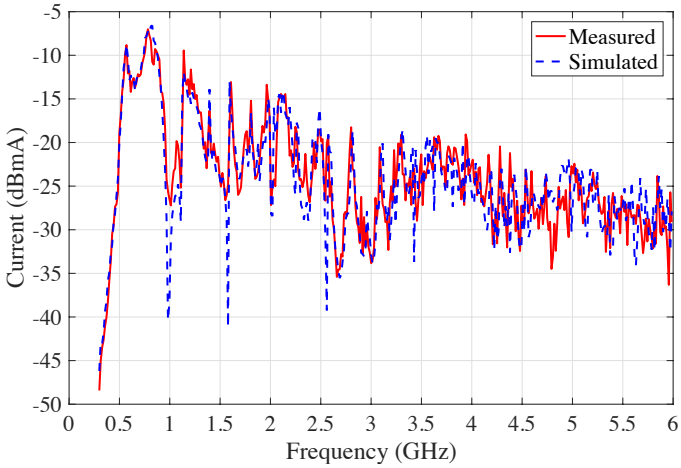

(b) Wire position 2

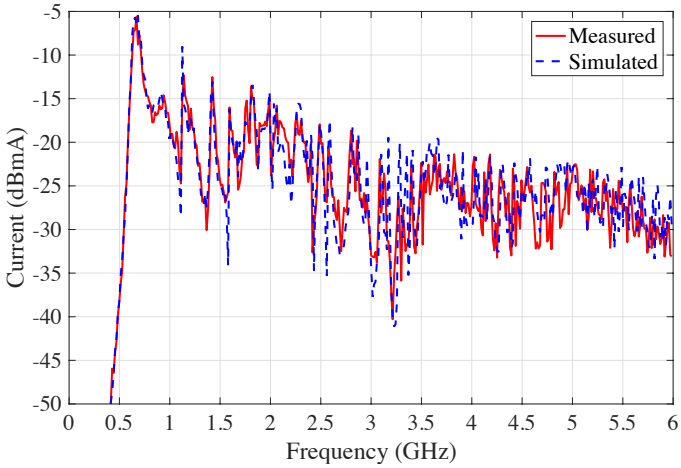

(c) Wire position 3

Figure 6.10. Mean current magnitude induced at the wire base when EUT is placed in a random field having 1 V/m RMS field level.

Other possibilities for the discrepancies between the measured and the simulated results are imperfect knowledge of the measured quality factor (obtained by taking the average of measurements at 70 tuner positions) and the measured input reflection coefficient of the transmitting antenna. Considering all such possible factors, very good agreement between the measured mean current and the simulated mean current is observed for all three wire positions.

FSV was used to further assess the agreement between the measured and the simulated results in Figure 6.10. Figure 6.11 shows the FSV analysis for all three wire positions. The overall FSV assessment is shown in Table 6.2. ADM shows very good agreement, and FDM and GDM showed good agreement for all three positions. FSV consistently assigns poorer agreement (higher value) with wire at position 2 than with position 1 and position 3 in Table 6.2. FSV gives higher GDM values at 982.3 MHz and 1.58 GHz with wire position 2 due to the differences in the depths of nulls the measured and the simulated results at these frequencies, which leads to a higher overall FSV value at wire position 2 than with positions 1 or 3. As discussed, these null differences are expected due to slight differences in the modeled and fabricated EUT geometry. Hence, the validity of numerical approach for calculating the EUT response due to a random field has been confirmed experimentally based on GDM score of "good".

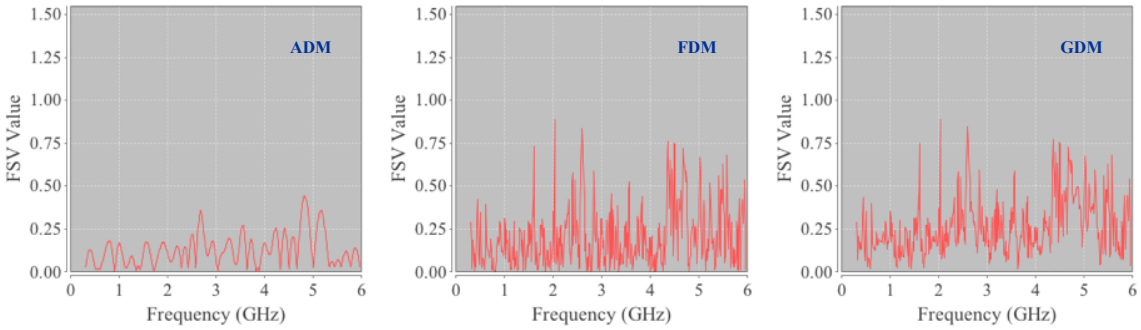

(a) Wire position 1

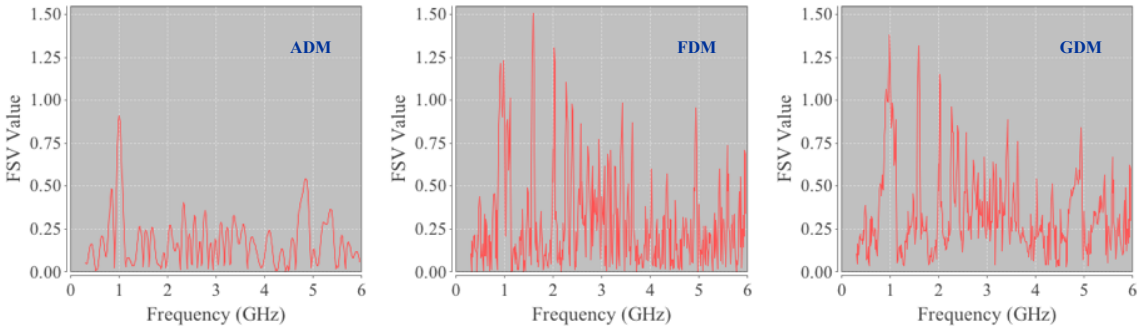

(b) Wire position 2

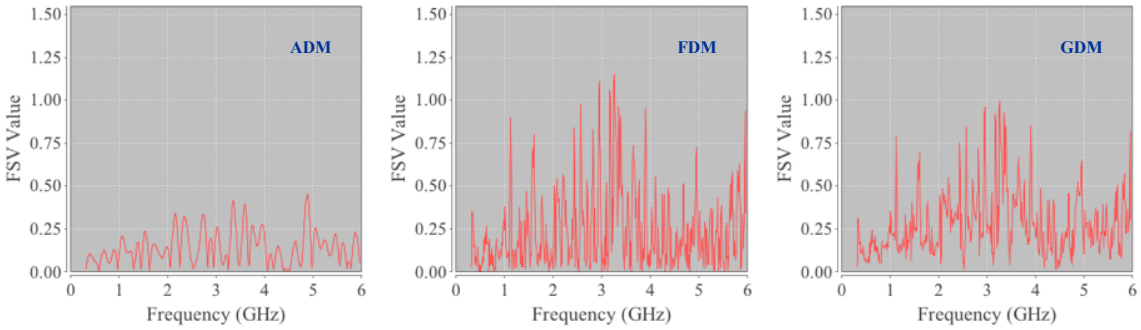

(c) Wire position 3

Figure 6.11. FSV analysis of the comparison between the measured and the simulated mean current, shown in Figure 6.10.

Table 6.2. Overall FSV assessment between the measured and the simulated mean current

FSV measures	Considered wire positions		
	Position 1	Position 2	Position 3
ADM	0.1303 (Very Good)	0.1779 (Very Good)	0.1431 (Very Good)
FDM	0.2036 (Good)	0.2875 (Good)	0.2439 (Good)
GDM	0.2654 (Good)	0.3359 (Good)	0.2815 (Good)

Figure 6.10 shows that the strength and frequencies of the resonances change with the change in the wire position, especially at 570 MHz and 800 MHz. However, the decreasing amplitude trend of mean current magnitude with increasing frequencies is similar for all three wire positions. This behavior may be due to the aperture dimensions. The largest aperture dimension is smaller than a wavelength below 2 GHz but three times the wavelengths at 6 GHz. So, the EUT cavity walls are sufficiently closed at lower frequencies to establish high Q factor resonant modes. At higher frequencies, energy more freely traverses the aperture and the established modes are of lower quality factor. Figure 5.10 suggests that the cavity modes are sparsely populated at lower frequencies and densely populated at higher frequencies. The lower quality factors at higher frequencies allow the cavity modes to be overlap, preventing sharp peaks and deep nulls from occurring in the frequency response.

6.7. Conclusion

In this chapter, the numerical simulation of the response of an EUT to a random field performed using an enhanced in-house CEM code was validated against reverberation chamber measurements. The mean induced current magnitude at the wire base was considered as the EUT response. A discrete representation of the plane wave spectrum was used in the numerical simulation to model

a field within a reverberation chamber. The measured mean induced current magnitudes at the EUT measurement port were obtained from the measured S_{21} between the source antenna and the EUT measurement port using the measured reverberation chamber quality factor and source antenna's free space reflection coefficient. The differences in the measured and the simulated mean current magnitude induced on a wire were consistent with that expected due to a finite number of samples used in the measurement and the geometrical differences between the physical and simulation model of the EUT. Overall, very good agreement between the numerical simulation and the measurements was achieved. An FSV comparison of the simulations and measurements gave very good agreement in ADM and good agreement in FDM and GDM. Hence, the numerical approach for calculating the EUT response to a random reverberation chamber field has been experimentally validated. This numerical approach is used in next chapter to repeat the simulation for different aperture positions and shapes on the EUT front face.

CHAPTER 7

ARTIFICIAL NEURAL NETWORK

The enhancement of an electromagnetics package developed in-house to use first-order basis functions was validated by measurement within the reverberation chamber in Chapter 6. Thus, this numerical simulation tool can be used to accurately predict the mean induced current at any test point within the EUT enclosure due to a random field. However, the coupling of a random external field into the EUT enclosure depends on various geometrical configurations such as the enclosure dimension, number of apertures and its dimension. Other parameters of EUT geometrical configuration which might affect the current at an EUT test point are the position of the aperture or the cable bundle within the EUT. Any change in any parameter of the geometrical configuration will give a different electromagnetic field within the enclosure and hence a different mean induced current magnitude. There is a need for a tool that can predict the sharp resonant peaks often encountered when the EUT geometry is slightly changed. The resonant peaks can cause failure in electronic devices so must be predicted. Therefore, various possible geometrical configurations must be considered. Numerical simulation can accurately characterize any geometrical configuration of the EUT, but due to its high computational cost, an only limited number of geometrical configuration can be directly analyzed.

This necessitates modeling the transfer function that gives a relationship between the geometrical parameters of the EUT as inputs and the mean induced current magnitude as the output. A technique for approximating such a transfer function is nonlinear regression [56], which gives a nonlinear mapping between the input and output parameters. The artificial neural network (ANN) is one technique based on nonlinear regression. The ANN has the ability to recognize the patterns in the output parameters for arbitrary input parameters. Thus, it was hoped that ANN modeling could identify the sharp resonances and nulls in the EUT induced current responses that might be missed by other interpolative and predictive schemes. In this work, an ANN is used to model the relationship between aperture configuration and position and the induced probe current, eliminating the need to repeat the numerical simulation under all possible frequencies of operation and aperture shapes, areas and positions.

7.1. Overview of Artificial Neural Network (ANN)

An ANN is trained to model the response of the EUT under various aperture and frequency conditions by providing it with a fixed set of input and output data. Once the system is trained, it can serve as an alternative to direct numerical simulation with specific input parameters, yielding an almost instantaneous response of that modeled structure. A higher number of input-output training pairs results in a more accurate prediction by the neural network. The concept of building the ANN system is inspired by a nervous system of a human brain, which contains interconnected neurons [57]. Neurons in an ANN are a nonlinear or linear functional block that processes the input signal into an output signal. Figure 7.1 shows a block diagram of a single neuron that accepts two inputs, x_1 and x_2, and gives y as the output. The output y of the neuron is

$$y = f\left(b + \sum_{i=1}^{2} w_i x_i\right), \tag{7.1}$$

where w_i is the weighting associated with the input x_i, b is the bias associated with the neurons, and f is the activation function. Commonly used activation functions are linear, hyperbolic tangent, logistic or sigmoid, threshold, and Gaussian [58].

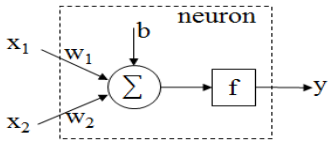

Figure 7.1. Block diagram of a single neuron with two input parameters.

These neurons are organized into layers that consist of one or more hidden layer and an output layer. The number of neurons in the output layer is equal to the number of output parameters. Usually, sigmoid functions are used as the activation functions in neurons in a hidden layer and linear functions are used for the neurons in an output layer [58].

Figure 7.2 shows the structure of an ANN using L hidden layers, the input layer, and the output layer. The input layer contains k parameters and output layer contains n parameters. The number of neurons in layer p is given by m_p, where p = 1, 2, 3, …., L. The number of neurons in the output layer (or Layer L+1) is equal to n. In Figure 7.2, $w_{i,j}^{(p)}$ is the weighting factor between the output of the i^{th} neuron in layer (p-1) (or i^{th} input parameter when p is equal to 1) to the input of the j^{th} neuron in layer p, $b_i^{(p)}$ is the bias associated with i^{th} neuron in layer p, and f_{hidden} and f_{output} are the activation function associated with the neuron in the hidden layer and the output layer, respectively. The input of each training data set is represented by

$$X = [x_1 \; x_2 \; x_3 \ldots\ldots\ldots \; x_k]^T, \tag{7.2}$$

and the output of each training data set is represented by

$$Y = [y_1 \; y_2 \; y_3 \ldots\ldots\ldots y_n]^T. \tag{7.3}$$

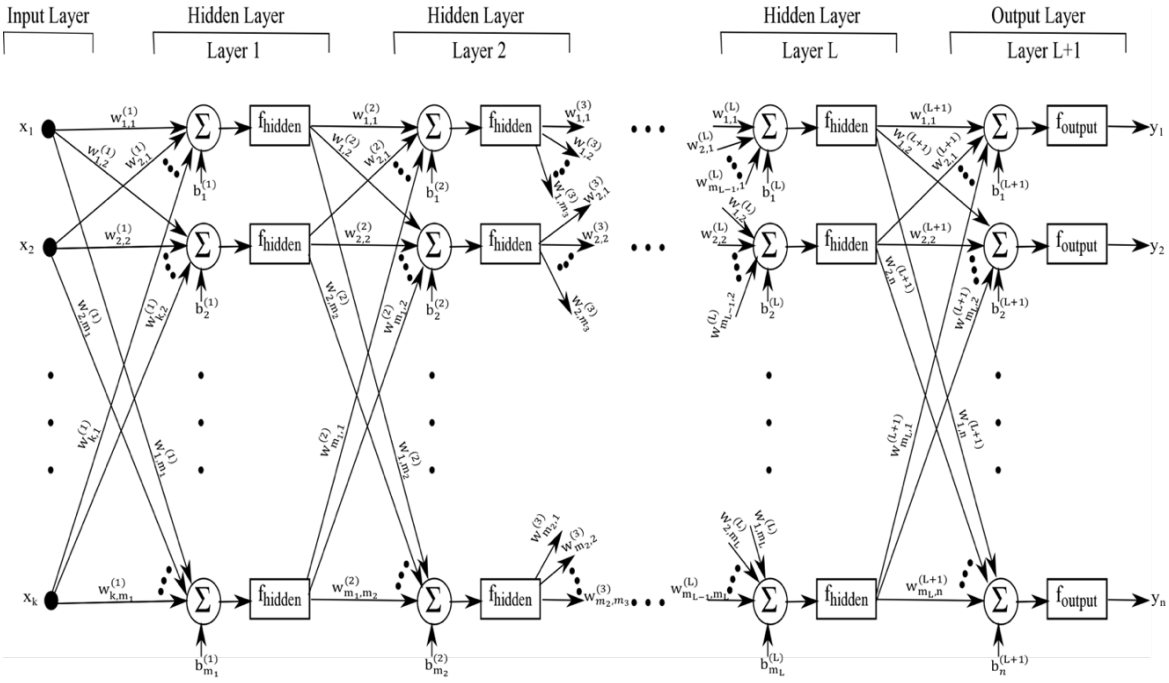

Figure 7.2. Structure of ANN using L hidden layers.

The goal of the neural network training is to minimize the mean squared error (MSE) between the target output and the output generated by the ANN for all training data. MSE is given by

$$\mathrm{MSE} = \frac{1}{\mathrm{N}} \sum_{\mathrm{i}=1}^{\mathrm{N}} (\mathrm{Y_i} - \mathrm{Y_i^s})^2 \,, \tag{7.4}$$

where $\mathrm{Y_i}$ is the output predicted by ANN and $\mathrm{Y_i^s}$ is the numerical simulation output due to the input parameter of the i^{th} training data, N is the total number of training data. The RMS (root mean square) error is given by

$$\text{RMS error} = \sqrt{\mathrm{MSE}} \,. \tag{7.5}$$

Generalization is the ability of ANN to estimate the output with input not used in training samples. Using too few neurons gives an under-learning problem while too many neurons gives overlearning problems [58]. With under-learning, the ANN has difficulty learning the training samples, possibly due to insufficient number of hidden neurons or insufficient training of the ANN. Over-learning is a situation where the ANN memorizes the training samples but does not generalized the output

well. Over learning may occur when a large number of hidden neurons or insufficient number of training samples are used. Hence, the number of neurons and the number of hidden layers was adjusted manually to achieve the desired accuracy in the ANN computations. Training is initialized by assigning random weighting factors and biases to the neurons. The training algorithm then adjusts the weighting factors and bias associated with the neurons in the hidden and output layers to minimize the MSE. The process is repeated until the desired MSE is achieved. Figure 7.3 shows the ANN training process. Foresee *et al.* [60] shows that the Bayesian regularization training algorithm [59] may reduce over-learning in the ANN training. Hence, the MATLAB neural network toolbox [61] implementation of this training algorithm was used in this work.

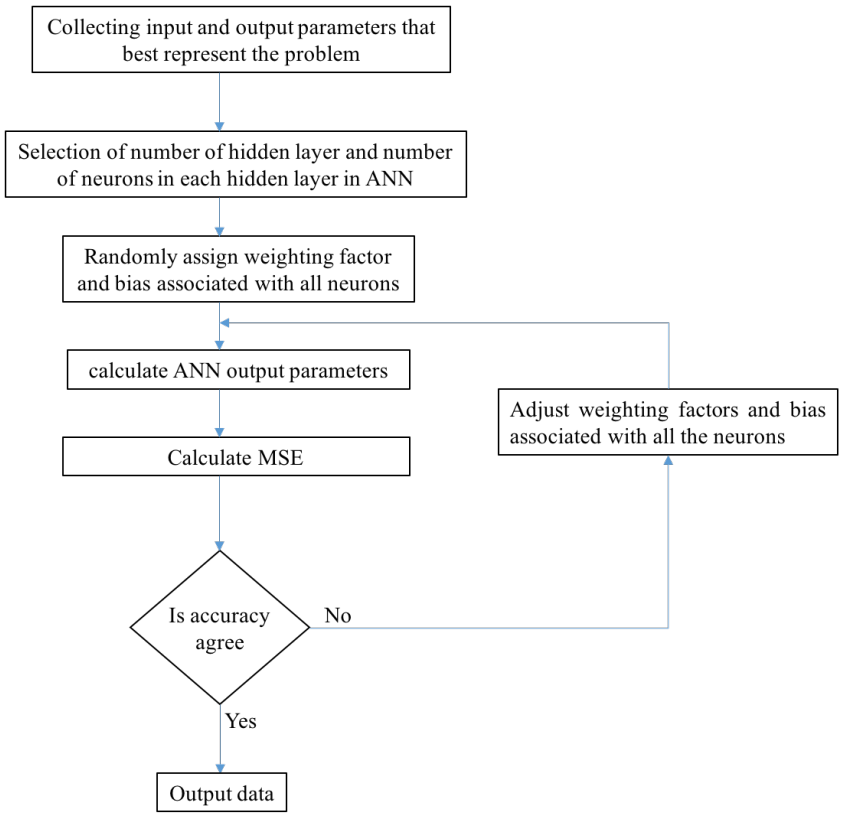

Figure 7.3. Procedure for training the artificial neural network (ANN).

7.2. Numerical simulation setup for collecting ANN training datasets

Hill [15] showed that the statistics of the current induced on the test object due to an ideally random, mechanically stirred reverberation chamber field follows the Rayleigh distribution. In the previous chapter, a large number of independent samples was needed to accurately estimate the statistics of the distribution at each frequency. West *et al.* [62] showed an alternative technique that gives the exact mean or variance of the Rayleigh-distributed current magnitude at a given test point from the current responses to $4L^2$ plane waves, where L is a sampling parameter in a discrete plane wave spectral model of the random chamber field that is proportional to the electrical size of the EUT. The plane wave directions were determined from discrete plane wave spectrum model with θ coordinate sampled at L zeros of the Legendre polynomial $P_L(\cos\theta)$ and ϕ coordinate sampled at 2L uniformly spaced points, each with two polarizations, as discussed in Chapter 6. Hence, no Monte-Carlo simulations need to be performed, considerably reducing the computational workload. Using this model, mean current magnitude is given by [62]

$$\langle |I| \rangle = \sqrt{\frac{\pi}{4} \langle |I|^2 \rangle}, \tag{7.6}$$

where $\langle |I|^2 \rangle$ is the mean of magnitude square of current samples given by

$$\langle |I|^2 \rangle = \frac{{E_0}^2}{8L} \sum_{l=1}^{L} w_l \sum_{m=1}^{2L} \left\{ \left| I_{lm,\alpha} \right|^2 + \left| I_{lm,\beta} \right|^2 \right\}, \tag{7.7}$$

E_0 is the desired RMS field within the chamber, w_l is the Gauss-Legendre quadrature weighting associated with θ_l, θ_l is the θ coordinate associated with l^{th} zero of the Legendre polynomial, $I_{lm,\alpha}$ and $I_{lm,\beta}$ are the currents induced at the test point due to single uniform planes wave of unity magnitude having a polarization vector along the direction $\hat{a}_\theta$ and $\hat{a}_\phi$, respectively. Substituting equation (7.7) into equation (7.6), the mean induced current magnitude is

$$\langle |I| \rangle = \sqrt{\frac{\pi {E_0}^2}{32L} \sum_{l=1}^{L} w_l \sum_{m=1}^{2L} \left\{ \left| I_{lm,\alpha} \right|^2 + \left| I_{lm,\beta} \right|^2 \right\}}. \tag{7.8}$$

For a 1 V/m RMS field level within the chamber ($E_0 = 1$), the mean induced current magnitude is given by

$$\langle |I| \rangle = \sqrt{\frac{\pi}{32L} \sum_{l=1}^{L} w_l \sum_{m=1}^{2L} \left\{ \left| I_{lm,\alpha} \right|^2 + \left| I_{lm,\beta} \right|^2 \right\}}. \tag{7.9}$$

The mean of the current induced on the wire of the EUT in Fig. 5.4, with the wire at position 2, by a random field ($E_0 = 1$) was calculated by using both Monte-Carlo simulation and the exact mean using equation (7.9). Figure 7.4 compares the exact mean with the Monte-Carlo results with N = 5, 10, 50, and 1000 independent samples. As observed, the mean estimated by Monte-Carlo simulation converged to the ideal mean for large N. Hence, equation (7.9) is used hereafter to obtain the current responses on the wire for different aperture shape, area and positions.

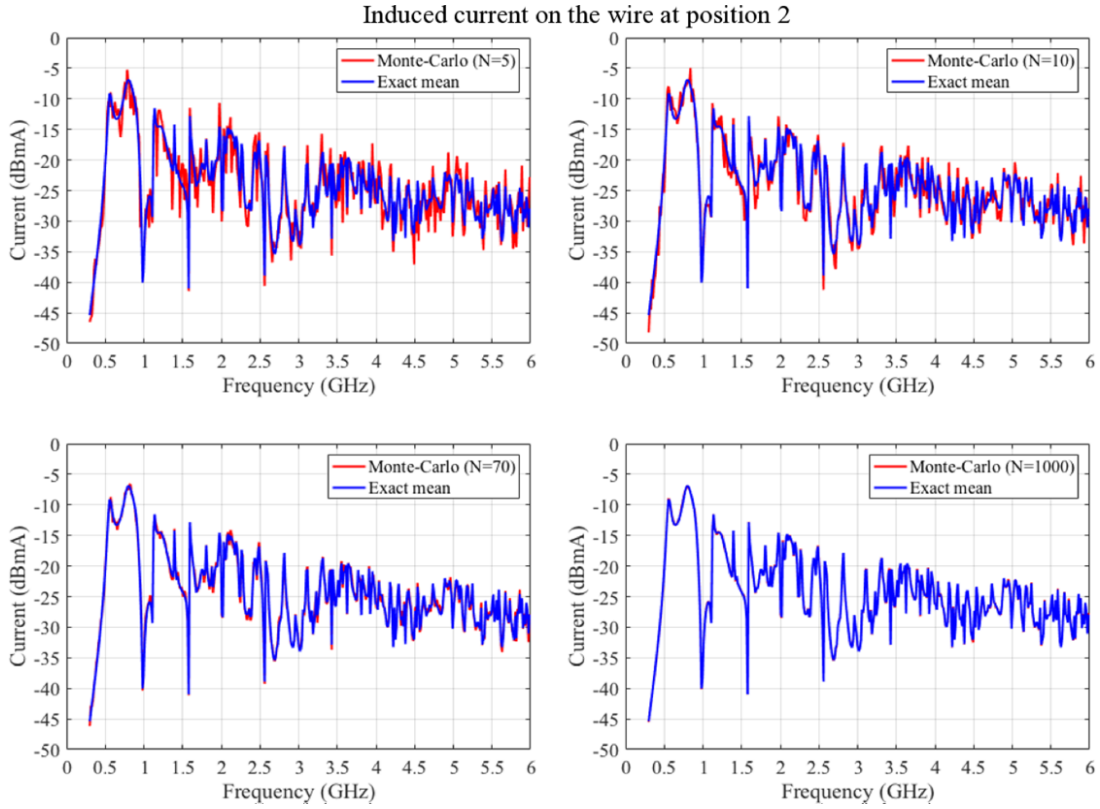

Figure 7.4. Simulated mean current for 15 cm × 6 cm aperture positioned at the center of the front face of the EUT.

7.3. Test case used for modeling ANN

In this work, the mean of the Rayleigh distributed induced current magnitude at the wire base was calculated using the trained ANN in the frequency range from 300 MHz to 2 GHz. The ANN was trained for arbitrary aperture positions with the aperture configurations shown in Table 7.1. Figure 7.5. shows the EUT with aperture configuration 1 centered on the aperture face. Aperture configurations 1 and 3 have almost equal aperture areas but different shapes. Aperture configurations 2 and 4 have areas approximately half the areas of configurations 1 and 3. Initially, 40 MHz frequency stepping was used to train the ANN, which giving 43 frequency samples. However, it was found that the desired accuracy in the training was achieved with 20 MHz frequency steps. Hence, the ANN training was performed using 20 MHz steps from 300 MHz to 2 GHz, giving 86 frequency samples.

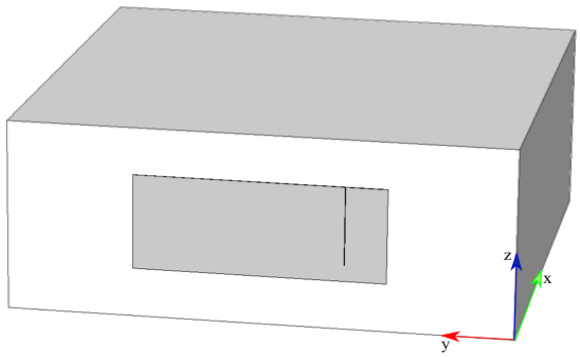

Figure 7.5. EUT with aperture configuration 1 and 30 × 30 × 12 cm cavity dimensions.

Table 7.1. Aperture configurations considered for training ANN

Aperture configuration number	Aperture dimensions	Aperture shape	Aperture area
1	15 cm × 6 cm	Rectangle	90 cm^2
2	15 cm × 3 cm	Rectangle	45 cm^2
3	9.5 cm × 9.5 cm	Square	90.25 cm^2
4	6.7 cm × 6.7 cm	Square	44.89 cm^2

The aperture in Figure 7.5 is centered at (0, 15 cm, 6 cm) from the lower right corner of the EUT front face. The front face of the EUT lies in the x = 0 plane. Hence, the input vector, X, contains three parameters for each aperture configuration, represented by

$$X = [y_a \;\; z_a \;\; f]^T, \tag{7.10}$$

where y_a and z_a are the y and z coordinate of the center position of aperture (in cm), respectively and f is the excitation frequency in GHz. The induced mean current magnitude on the wire, the output of the ANN, was calculated for the three different wire positions, same as in Chapters 5 and 6. Instead of training ANN separately for different wire positions, three parameters in the output vector were used in the ANN. This output vector is given by

$$Y = [I_1 \;\; I_2 \;\; I_3]^T, \tag{7.11}$$

where I_1, I_2, and I_3 are the Rayleigh distributed mean current induced on the wire at position 1, position 2 and position 3, respectively. This way, the ANN was trained one time for each aperture configuration. The input and output parameters in a training data set were scaled to a [-1, 1] range before providing it for training ANN, as suggested in [60]. After training, the ANN was validated against the numerical simulation for apertures centered at arbitrary points on the EUT front face that were not used in training. The coordinates of the aperture center positions that were used for training and validation are given in Appendix B.

7.4. ANN modeling and validation against numerical simulation

7.4.1. 15 cm × 6 cm aperture

It is not known *a priori* how many aperture positions are required in the training data set to accurately train the ANN. Fewer aperture positions give lower accuracy in the ANN output. For this reason, the ANN was separately trained with 9, 17 and 29 aperture positions as shown in Figure 7.6. These apertures are centered at T_i, where i = 1, 2, 3, ..., 29. After training, the ANN output with apertures centered at points A_1 and A_2 (shown in Appendix B) was validated against direct

numerical simulation. In this section, a single rectangular aperture configuration with dimensions 15 cm × 6 cm was considered.

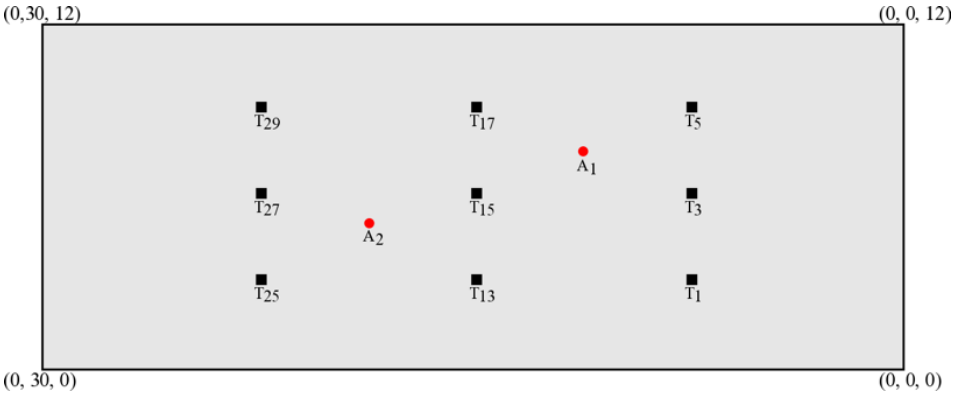

(a) 9 training points

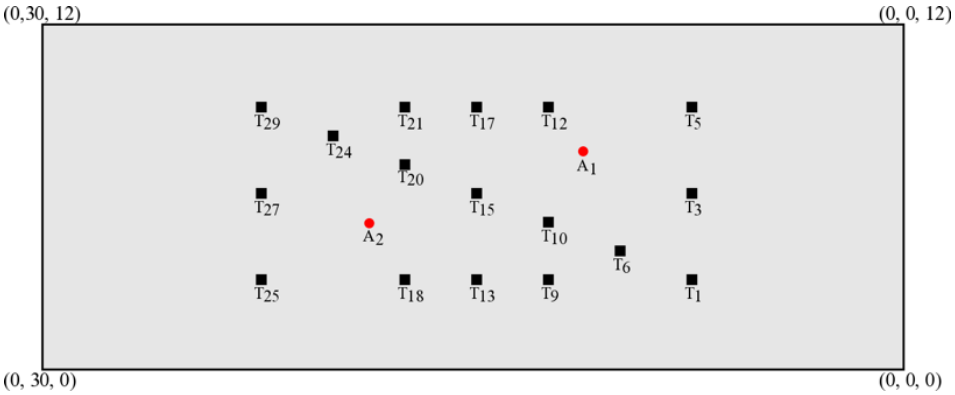

(b) 17 training points

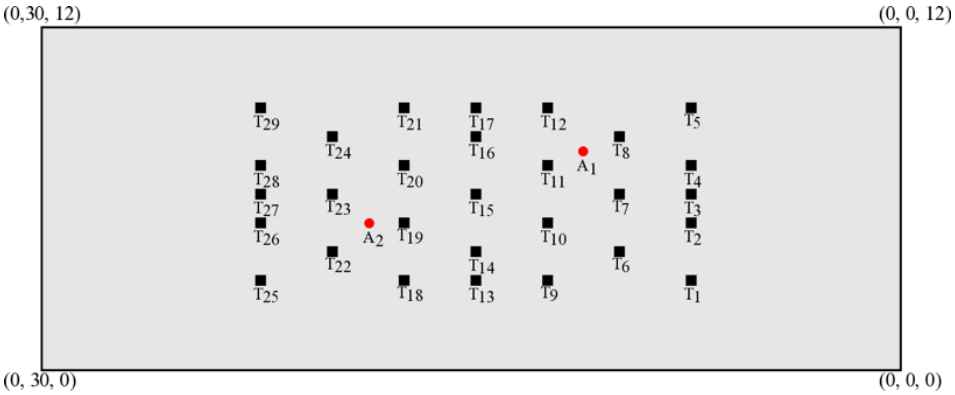

(c) 29 training points

Figure 7.6. Center positions of 15 cm × 6 cm aperture used as training (shown by black square) and testing (shown by red circles).

7.4.1.1. ANN training performance

As discussed, the goal of ANN training is to minimize MSE between the output of numerical simulation and the ANN output. If the MSE is above the user specified tolerance limit, the weights and biases associated with the neurons are adjusted. The MSE reduces after each iteration. Training is stopped when the MSE does not decrease after several iterations. As discussed, all input and output parameters are scaled to a [-1, 1] range prior to training. Figure 7.7 shows the MSE between normalized output of the generalized ANN and the normalized output of numerical simulation across the different aperture positions used in training. Two MSEs are shown in Figure 7.7, one that includes all training aperture positions, labeled as "training datasets", and another that includes the aperture positions used for validation, labeled as "testing datasets". Table 7.2 shows a summary of the ANN performance for different numbers of training aperture positions used. As expected, the number of training aperture positions increases, the final values of both the MSE and mean percentage error among the training and testing datasets decreases.

Table 7.2. Summary of ANN performance with 15 cm × 6 cm aperture.

Number of training aperture positions	Total training samples	Total testing samples	Mean percentage error	
			Training datasets	Testing datasets
9	774	172	11.87 %	13.75 %
17	1462	172	4.25 %	4.57 %
29	2494	172	2.57 %	2.9 %

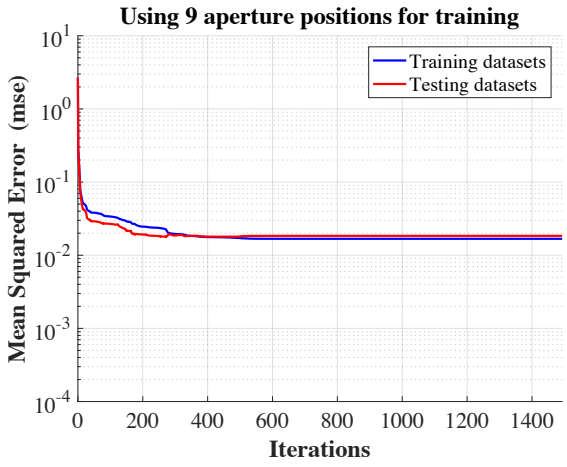

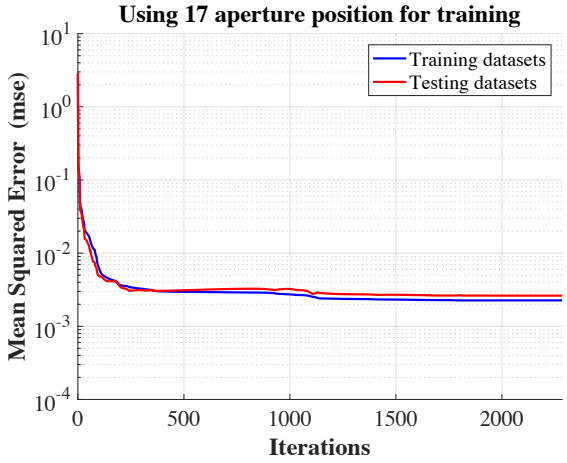

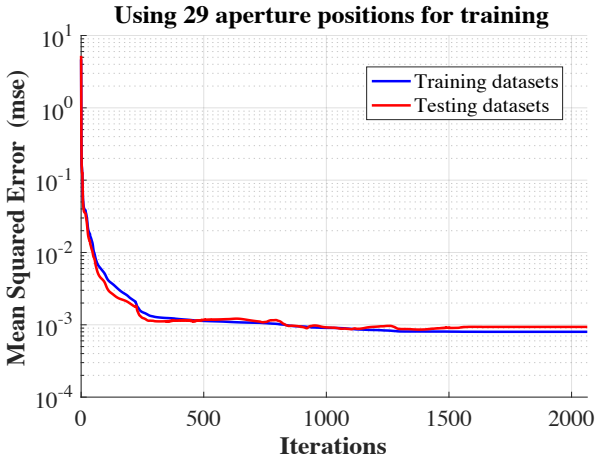

Figure 7.7. ANN performance for various aperture training points.

7.4.1.2. Comparison of the results between ANN and numerical simulation.

In this section, the estimates of the mean current induced on the wire provided by the trained ANN are compared with direct numerical simulation. Figures 7.8 and 7.9 show the comparisons when the aperture is centered at points A_1 and A_2, respectively, for the three different wire positions. Figures 7.8 and 7.9 show that the ANN mean current better approximates the numerically simulated mean current as the number of training aperture positions increases. Table 7.3 and Table 7.4 gives the RMS error between the ANN approximated and numerically simulated mean induced currents over the frequency range from 300 MHz to 2 GHz for aperture positions A_1 and A_2, respectively.

The RMS error reduces with an increasing number of training aperture positions. With 29 training positions, the maximum RMS error observed is 1.04 dB, and the largest peak magnitude difference of 3.13 dB occurs at 1.42 GHz with wire position 2 in Figure 7.8 (c). Overall, Figure 7.8 (c) and Figure 7.9 (c) shows that the agreement between the ANN and the numerical simulation are better than that typically observed between the measurements and the numerical simulation. For example, consider Figure 6.10 that shows the comparison between the measurements and the numerical simulation. In frequency range from 300 MHz to 2GHz, the maximum RMS error observed was 3.06 dB, and the largest peak magnitude difference of 6.2 dB occurred at 1.08 GHz, all with wire position 2. As discussed in Chapter 3, such differences are expected due to the geometrical differences between the fabricated prototype and an ideal numerical simulation model. The ANN with 29 training aperture positions is therefore accepted as validated. It is used to analyze the dependence of the induced wire current with a variation in the aperture position in the next section.

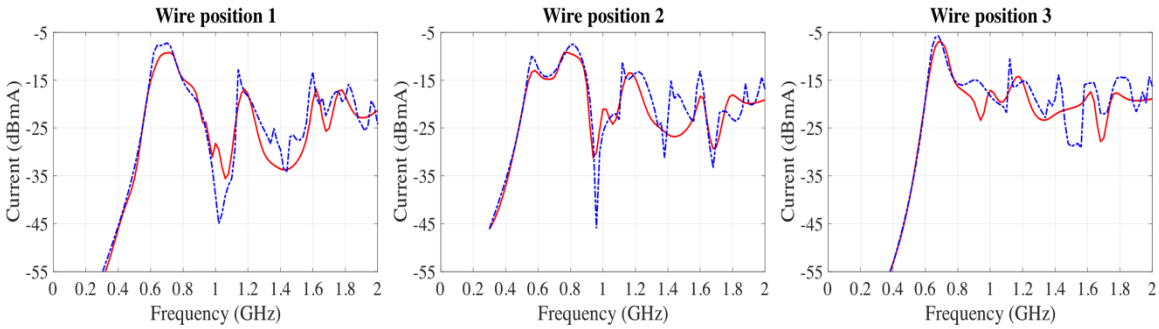

(a) 9 training aperture positions

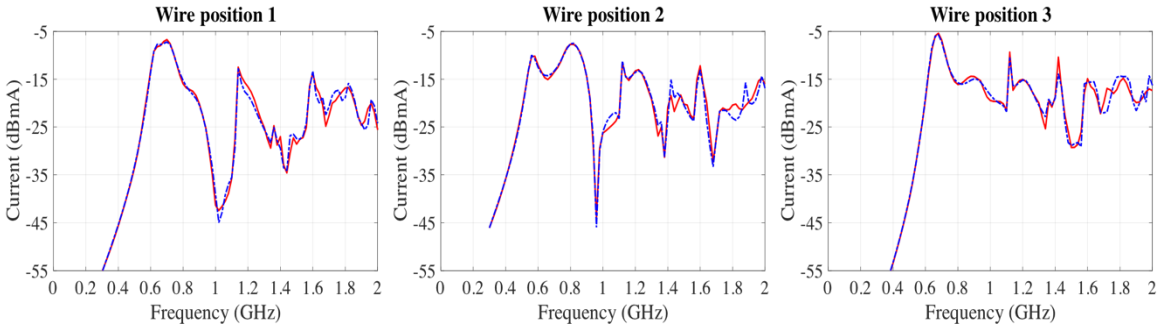

(b) 17 training aperture positions

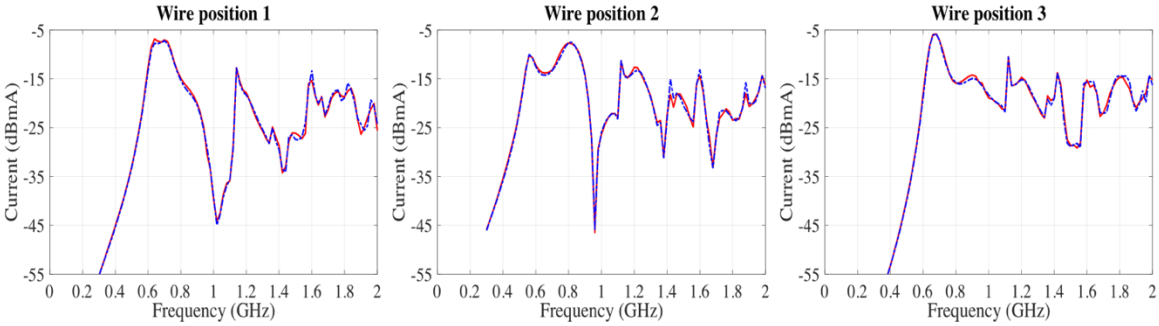

(c) 29 training aperture positions

Figure 7.8. Comparison of ANN (solid red line) and the numerical simulation (dash-dot blue line) current responses on the wire with 15 cm × 6 cm aperture at test position A_1.

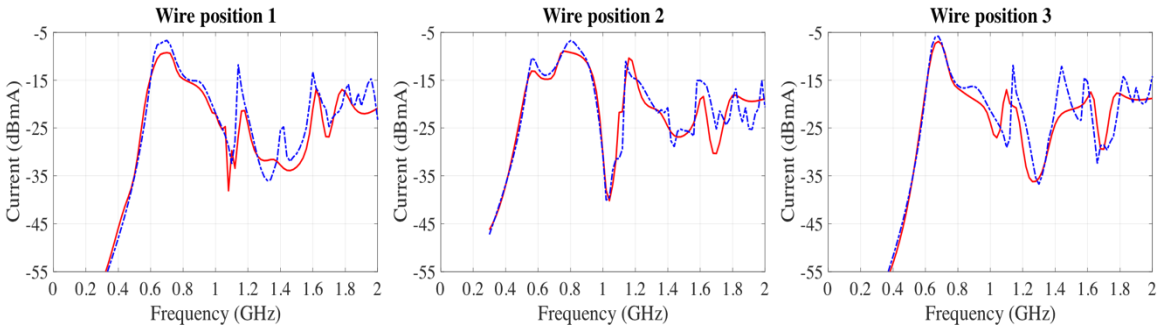

(a) 9 aperture positions

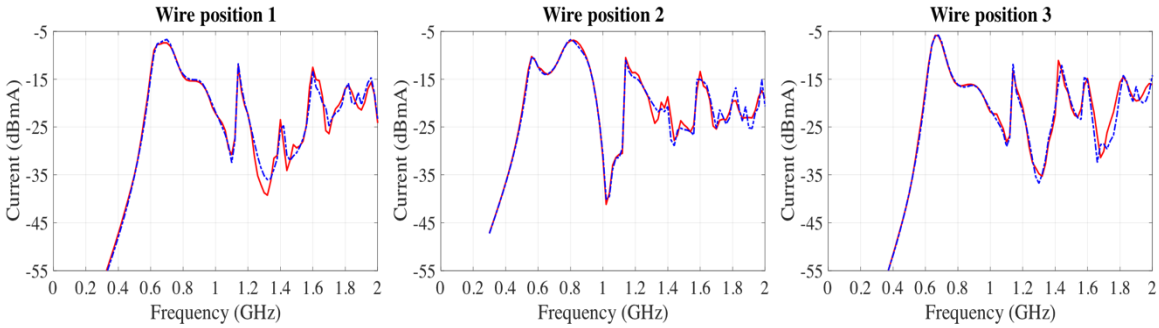

(b) 17 aperture positions

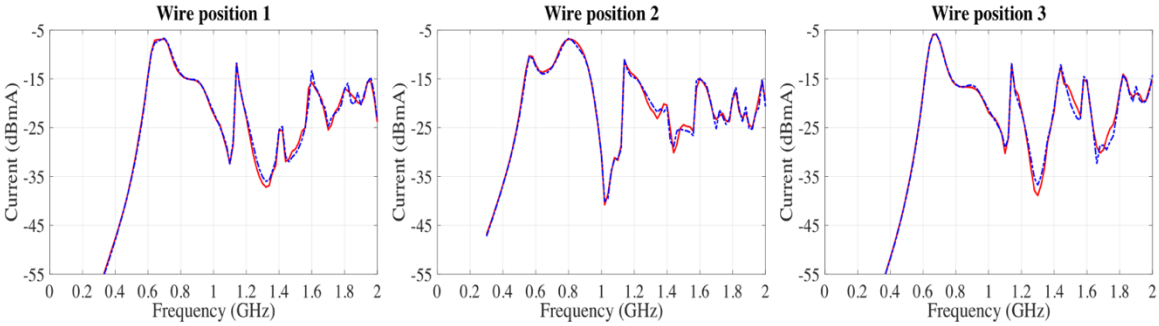

(c) 29 aperture positions

Figure 7.9. Comparison of ANN (solid red line) and the numerical simulation (dash-dot blue line) current responses on the wire with 15 cm × 6 cm aperture at test position A_2.

Table 7.3. RMS error (in dB) between ANN and numerical simulation results in Figure 7.8

Number of training aperture positions	Wire position 1	Wire position 2	Wire position 3
9	3.81	3.77	3.45
17	1.21	1.33	1.21
29	0.74	0.7	0.63

Table 7.4. RMS error (in dB) between ANN and numerical simulation results in Figure 7.9

Number of training aperture positions	Wire position 1	Wire position 2	Wire position 3
9	3.54	3.06	3.8
17	1.5	1.24	1.62
29	0.87	0.83	1.04

7.4.1.3. Variability in EUT response due to aperture movement

Figure 7.10 shows the change in the frequency response of the current induced on a wire probe at position 2 as the 15 cm × 6 cm aperture is moved over the aperture face of the EUT. The top part of the figure shows the dependence when the aperture position is varied in the y direction, orthogonal to the alignment of wire probe (horizontally), and bottom part of the figure shows the change when the aperture is moved in the z direction, parallel to the alignment of wire probe (vertically). The color scale in the figure represents the induced current value in dBmA. Dark red represents strong resonant peaks and dark blue represents deep nulls in the current responses. The aperture dimensions limit the range of the center position to 7.5 cm to 22.5 cm in the y direction and to 3 cm to 9 cm in the z direction.

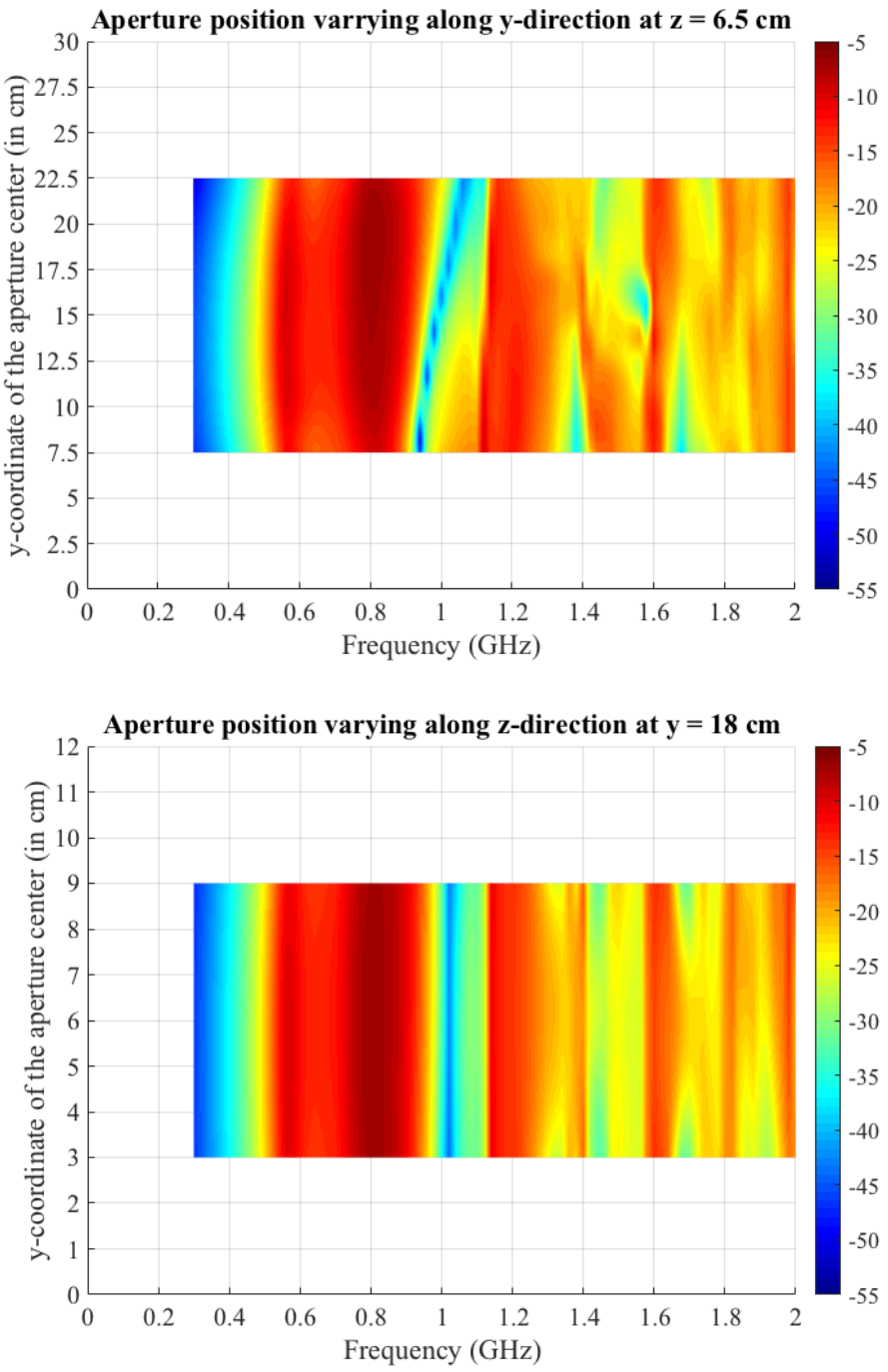

Figure 7.10. Current responses induced on the wire at position 2 with the variation in the center position of 15 cm × 6 cm aperture.

Figure 7.10 shows that the current response is very sensitive to the y position of the aperture, especially at higher frequencies. This was expected since, as discussed in Chapter 3, the magnitudes

of the current responses are highly sensitive to small changes of the EUT geometry. However, they show only a small dependence on the z-dimension aperture position, which was not expected. This might be due to fewer training aperture positions used in the z direction. Hence, this analysis was repeated in the next section using the 15 cm × 3 cm aperture, allow for more z-dimension training points with same sampling density.

7.4.2. 15 cm × 3 cm aperture

The ANN was trained to find the current induced on the wire probe when the 15 cm × 3 cm aperture was moved on the EUT aperture face. The aperture positions used in training are shown in Figure 7.11. Part (a) of the figure shows that more training positions, 47, are available with this smaller aperture than with the 15 cm × 6 cm aperture. The ANN was also trained with fewer aperture positions, as shown in Figure 7.11 (b) and (c). Figure 7.11 (b) was obtained by removing the aperture positions at z = 3, 6, 9 (in cm), giving a sparser sampling in the z direction. Similarly, Figure 7.11 (c) was obtained by removing the aperture positions at y = 10, 15, 20 (in cm), giving sparser sampling in the y direction. For convenience, sparse sampling in the z direction is named "sparse-z aperture positions", and sparse sampling in the y direction is named "sparse-y aperture positions". The ANN induced current responses are compared with direct numerical simulation for aperture positions A_5, A_6, and A_7 in Figure 7.11. The total testing samples listed are associated with 3 aperture positions at A_5, A_6 and A_7 and 86 test frequencies.

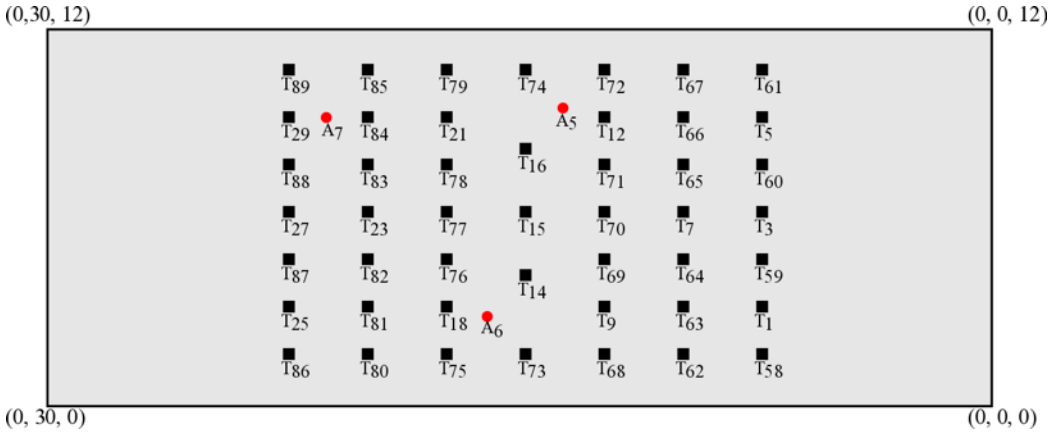

(a) 47 training aperture positions

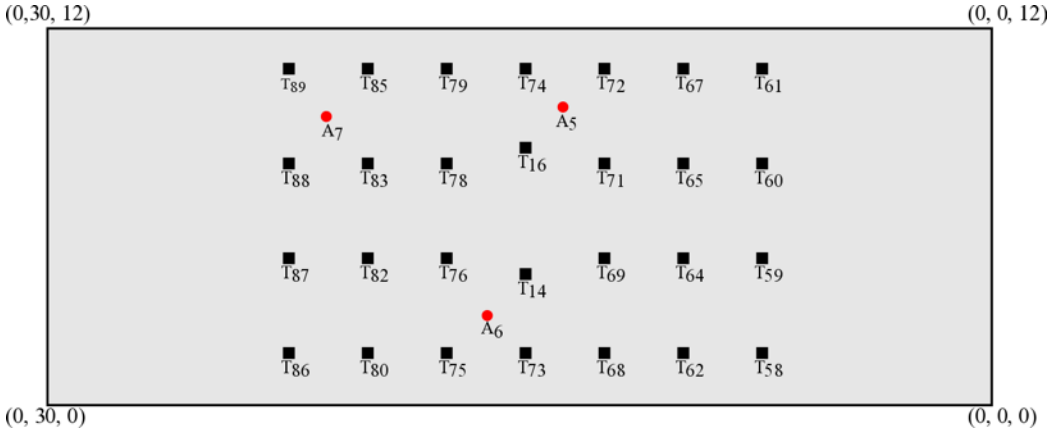

(b) 28 training positions (sparse in z-direction)

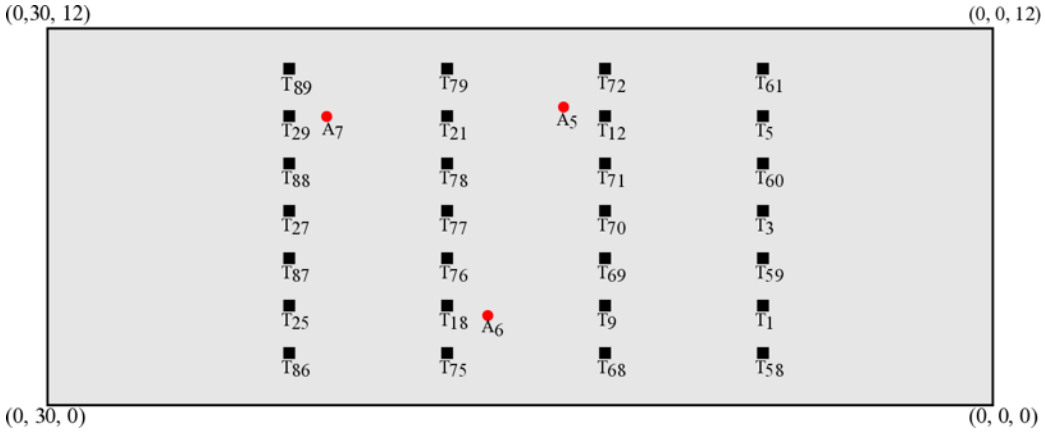

(c) 28 training positions (sparse in y-direction)

Figure 7.11. Center positions of 15 cm × 3 cm aperture used as training (shown by black squares) and testing (shown by red circles).

Table 7.5. Summary of ANN performance with 15 cm × 3 cm aperture.

Number of training aperture positions	Total training samples	Total testing samples	Mean percentage error	
			Training datasets	Testing datasets
47	4042	258	2.8 %	2.93 %
28 (sparse in z-direction)	2408	258	4.42 %	4.24 %
28 (sparse in y-direction)	2408	258	5.97 %	6.46 %

7.4.2.1. Comparison of the results between ANN and numerical simulation.

Figure 7.12 compares the ANN estimation of the induced current with direct numerical simulation when the aperture is centered at point A_5. Similarly, Figure 7.13 and 7.14 shows the comparison when the aperture is centered at positions A_6 and A_7, respectively. Tables 7.6, 7.7, and 7.8 gives the RMS error between the ANN and numerically simulated mean induced currents associated with aperture positions A_5, A_6, and A_7, respectively. Figures 7.12, 7.13, and 7.14 show that the ANN currents obtained with 47 trained aperture positions closely approximate the numerically simulated results for all wire positions and test aperture positions. The RMS error varies from 0.61 to 1.36 dB among all the cases, which is smaller than the 3.06 dB error observed experimentally. The largest peak magnitude difference of 4.4 dB occurred at 1.16 GHz with wire position 1 in Figure 7.12 (a), smaller than the 6.2 dB magnitude difference in the peak which was observed experimentally.

The figures also show that the ANN results are only slightly degraded when the sparse-z aperture-position sampling is used. However, sparse-y sampling gives a much greater loss of accuracy. This behavior occurs with all wire positions and test aperture positions. With sparse-z sampling in the

ANN training, the RMS error among all cases varies from 1.04 to 1.87 dB. Whereas, with sparse-y ANN training, the RMS error increases to from 1.48 to 3.26 dB.

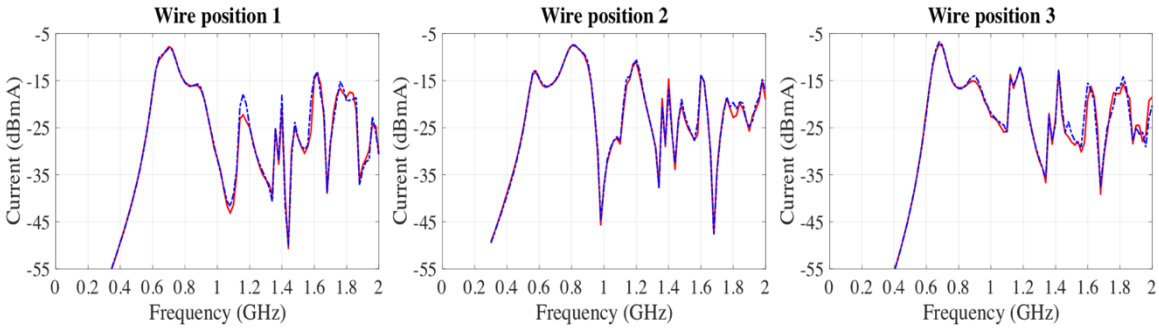

(a) 47 training aperture positions

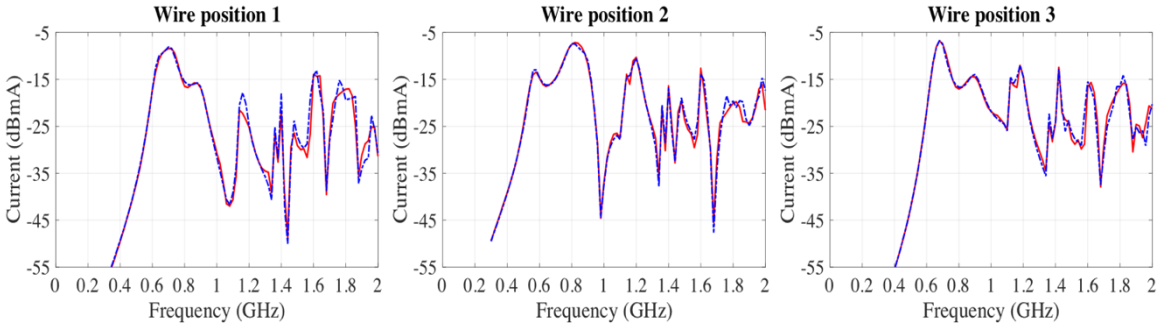

(b) Sparse-z aperture positions

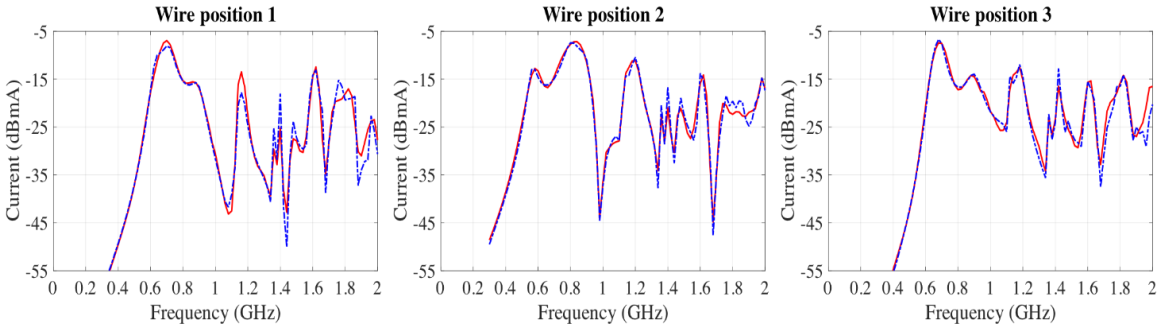

(c) Sparse-y aperture positions

Figure 7.12. Comparison of ANN (solid red line) and the numerical simulation (dash-dot blue line) current responses on the wire with 15 cm × 3 cm aperture at test position A_5.

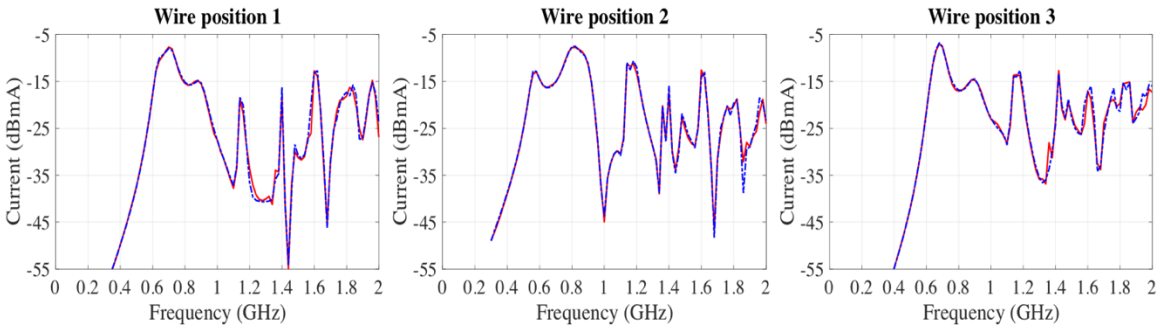

(a) 47 training aperture positions

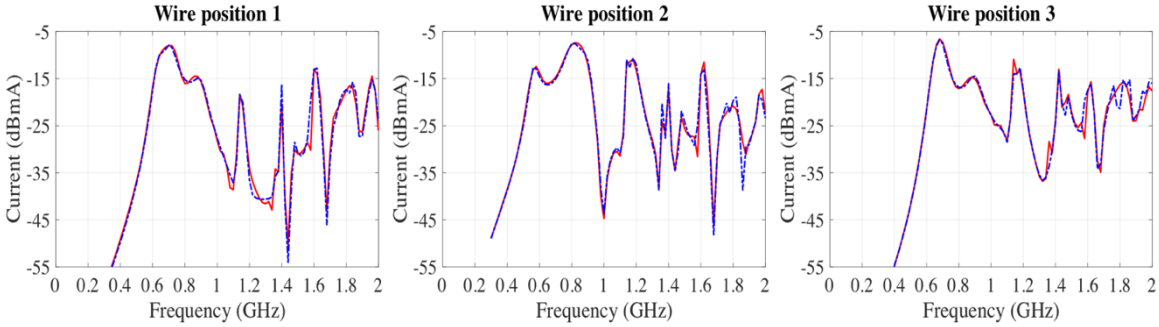

(b) 28 aperture positions (sparse in z-direction)

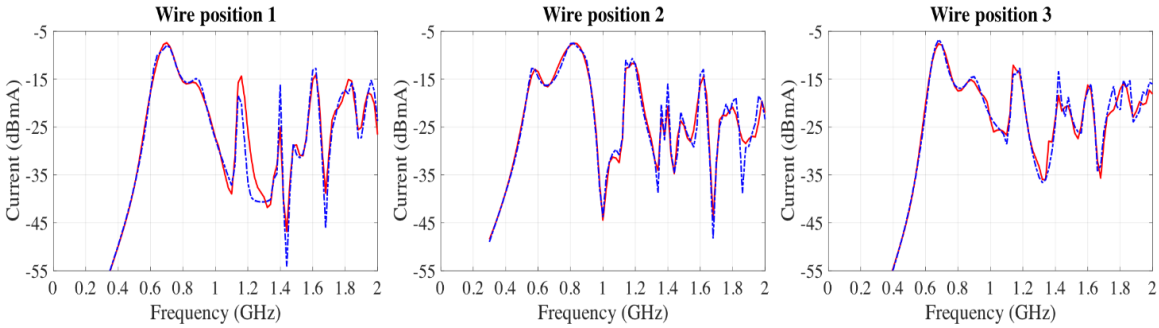

(c) 28 aperture positions (sparse in y-direction)

Figure 7.13. Comparison of ANN (solid red line) and the numerical simulation (dash-dot blue line) current responses on the wire with 15 cm × 3 cm aperture at test position A_6.

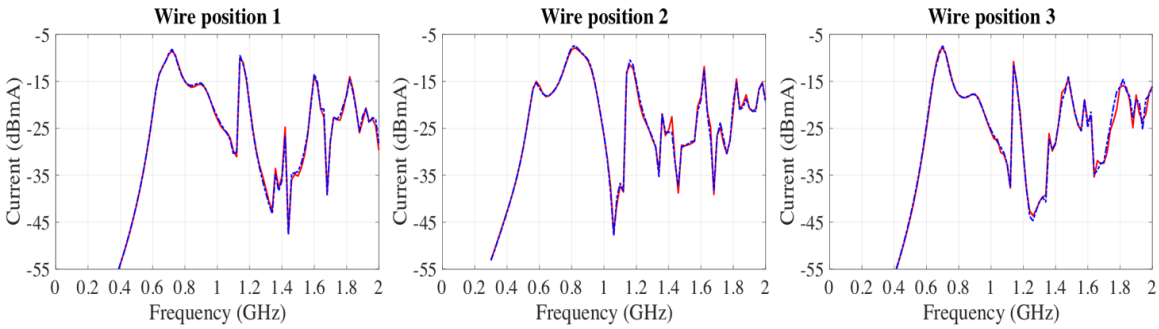

(a) 47 training aperture positions

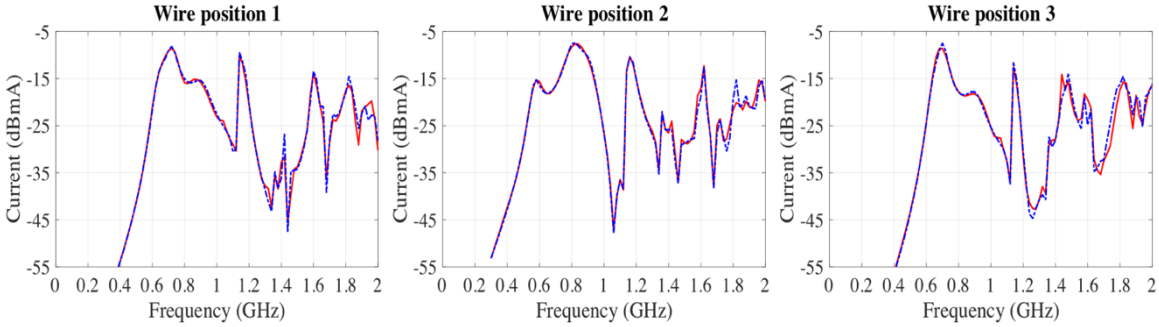

(b) 28 aperture positions (sparse in z-direction)

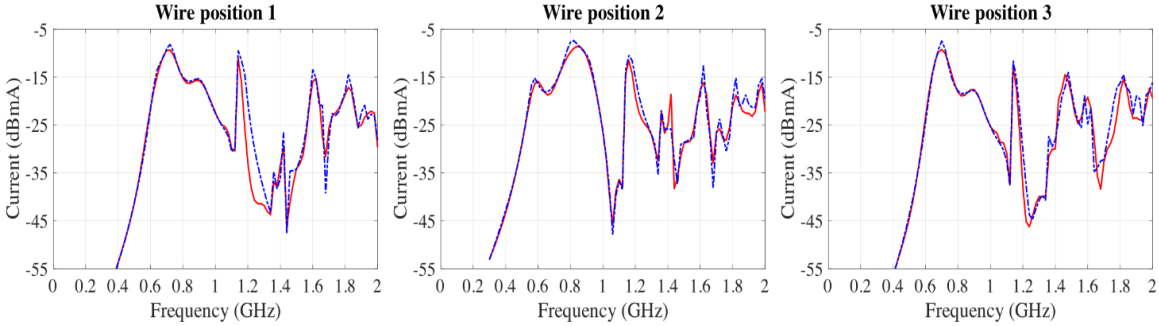

(c) 28 aperture positions (sparse in y-direction)

Figure 7.14. Comparison of ANN (solid red line) and the numerical simulation (dash-dot blue line) current responses on the wire with 15 cm × 3 cm aperture at test position A_7.

Table 7.6. RMS error (in dB) between ANN and numerical simulation results in Figure 7.12.

Number of training aperture positions	Wire position 1	Wire position 2	Wire position 3
47	1.36	0.78	1.35
28 (sparse in z-direction)	1.87	1.23	1.38
28 (sparse in y-direction)	2.4	1.48	1.86

Table 7.7. RMS error (in dB) between ANN and numerical simulation results in Figure 7.13.

Number of training aperture positions	Wire position 1	Wire position 2	Wire position 3
47	1.17	0.99	1.17
28 (sparse in z-direction)	1.74	1.69	1.57
28 (sparse in y-direction)	2.78	2.06	1.68

Table 7.8. RMS error (in dB) between ANN and numerical simulation results in Figure 7.14.

Number of training aperture positions	Wire position 1	Wire position 2	Wire position 3
47	0.61	0.71	0.98
28 (sparse in z-direction)	1.4	1.04	1.58
28 (sparse in y-direction)	3.26	1.88	2.47

7.4.2.2. Variability in EUT response due to aperture movement

The analysis of the previous section is now repeated with the wire probe placed at position 1. Figure 7.15, 7.16 and 7.17 shows the results with the 15 cm × 3 cm aperture. Again, the current responses

are much more sensitive to the changes in the aperture position in the y direction than in the z direction. The y-dimension dependence is greatest at frequencies above about 900 MHz. Figures 7.15 and 7.16 show that the ANN gives similar accuracy with either 47 aperture training positions or 28, sparse-z sampled aperture positions. However, the ANN results are again degraded when trained with 28 (sparse-y) positions. For example, in Figure 7.15 and 7.17, significant differences occur between the 47 position (dense sampling) and 28 sparse-y sampling ANN predictions in the 1.1 – 1.35 GHz frequency range when the aperture position is moved from y = 12.5 cm to 22.5 cm, and in the 1.55 – 1.65 GHz range when the aperture moves from y = 12.5 cm to 17.5 cm. Similarly, poor results occur with sparse-y sampling but moving the aperture in the z direction.

The variation in induced current due to aperture movement can be explained by the modal configurations of the field inside the EUT cavity. The excited field modes within the cavity can be transverse electric (TE) or transverse magnetic (TM). The electric vector potentials for discrete TE^Z modes are given by [51]

$$\begin{gathered} F_z(x,y,z) = A_{mnp}\cos\left(\frac{m\pi}{a}x\right)\cos\left(\frac{n\pi}{b}y\right)\sin\left(\frac{p\pi}{d}z\right) \\ m = 0,1,2,3,\ldots., n = 0,1,2,3,\ldots., p = 1,2,3,\ldots. \\ m = n \neq 0\,, \end{gathered} \tag{7.12}$$

where a, b, and d are the length, width and height of a cavity, respectively. In Figure 7.5, a = 30 cm, b = 30 cm and d = 12 cm. For TM^Z modes, the magnetic vector potential is given by [51]

$$\begin{gathered} A_z(x,y,z) = A_{mnp}\sin\left(\frac{m\pi}{a}x\right)\sin\left(\frac{n\pi}{b}y\right)\cos\left(\frac{p\pi}{d}z\right) \\ m = 1,2,3,\ldots., n = 1,2,3,\ldots., p = 0,1,2,3,\ldots., \end{gathered} \tag{7.13}$$

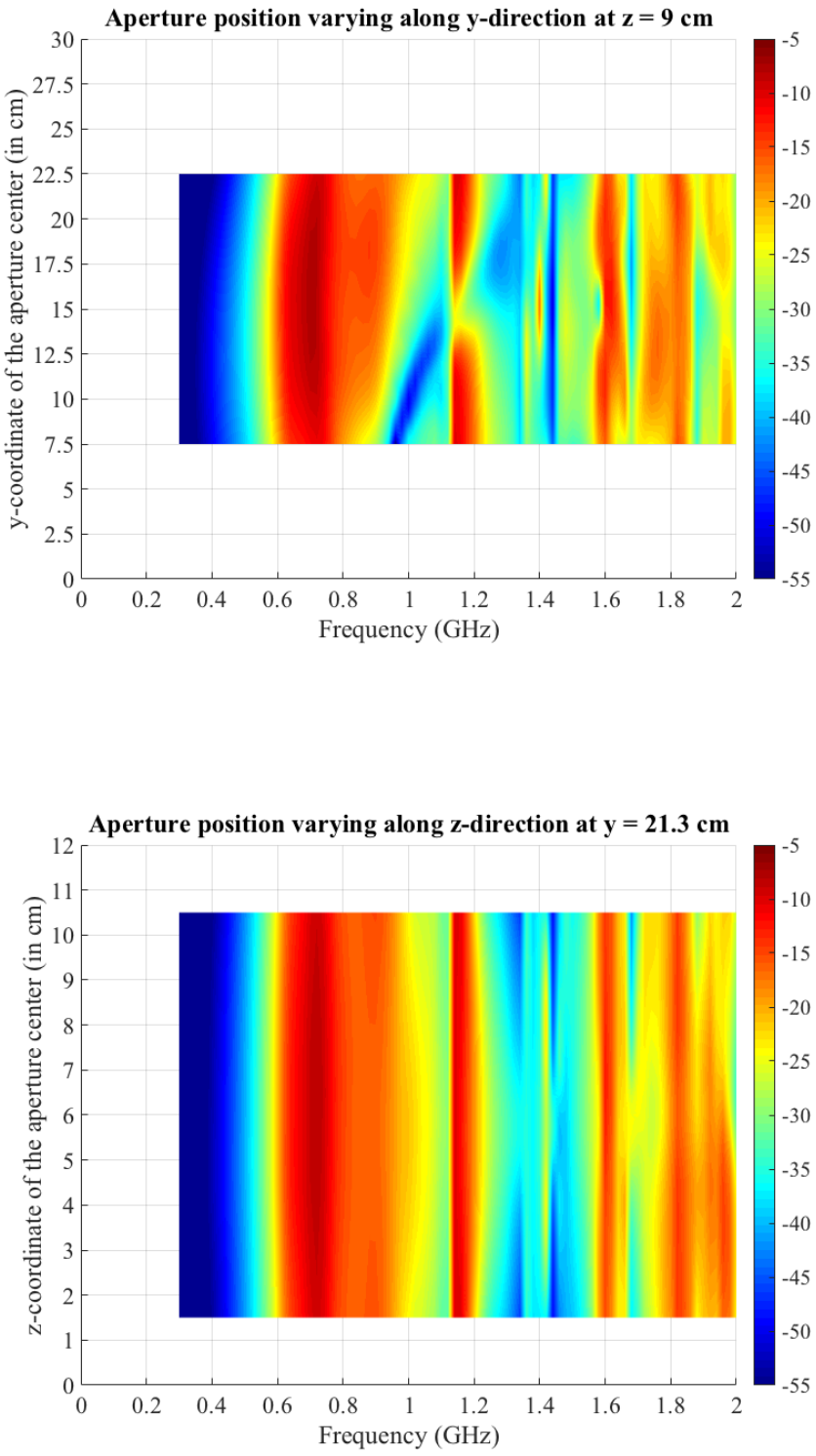

Figure 7.15. Current responses induced on the wire at position 1 using 47 positions of 15 cm × 3 cm aperture in ANN training.

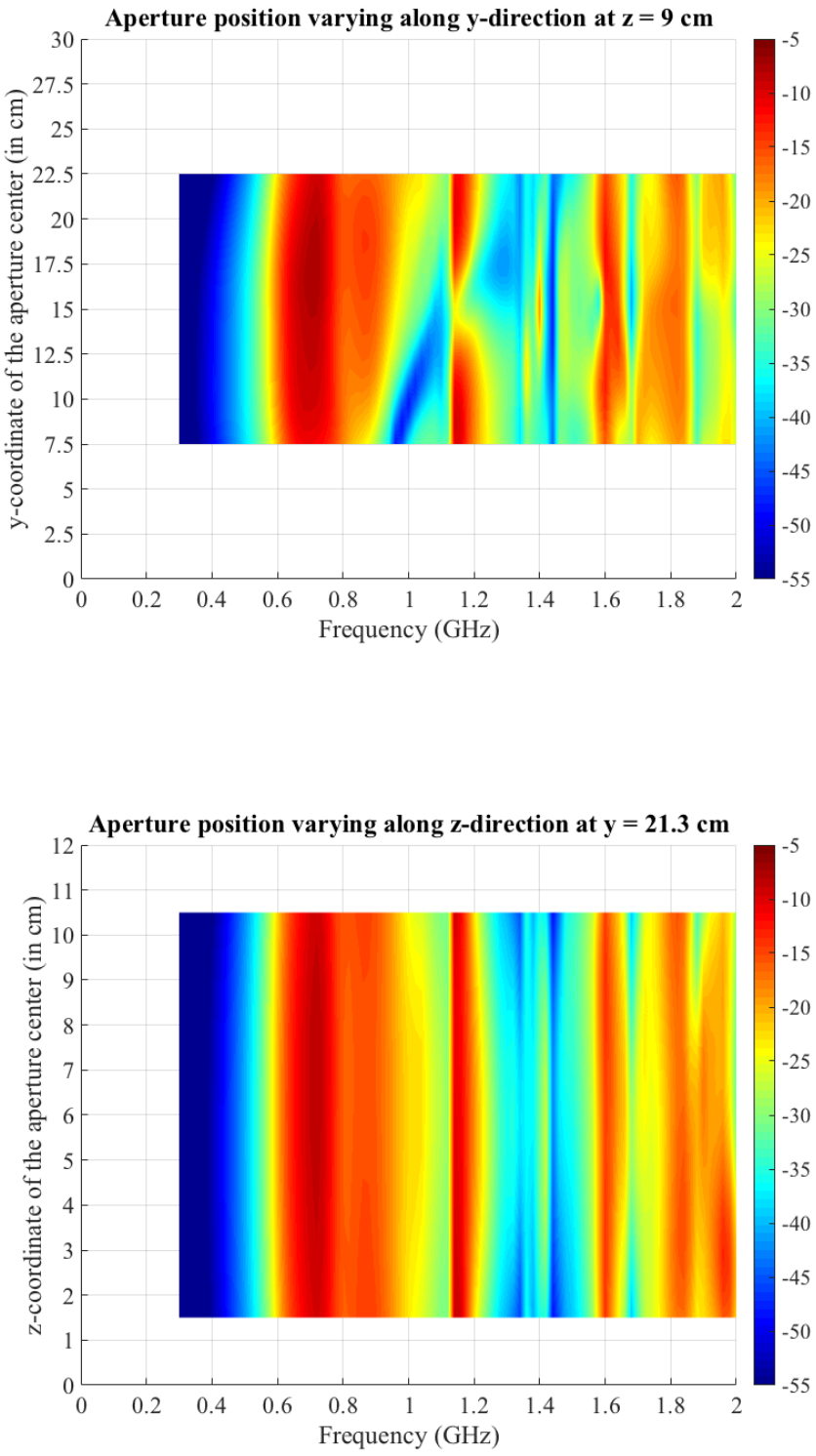

Figure 7.16. Current responses induced on the wire at position 1 using 28 (sparse-z) positions of 15 cm × 3 cm aperture in ANN training.

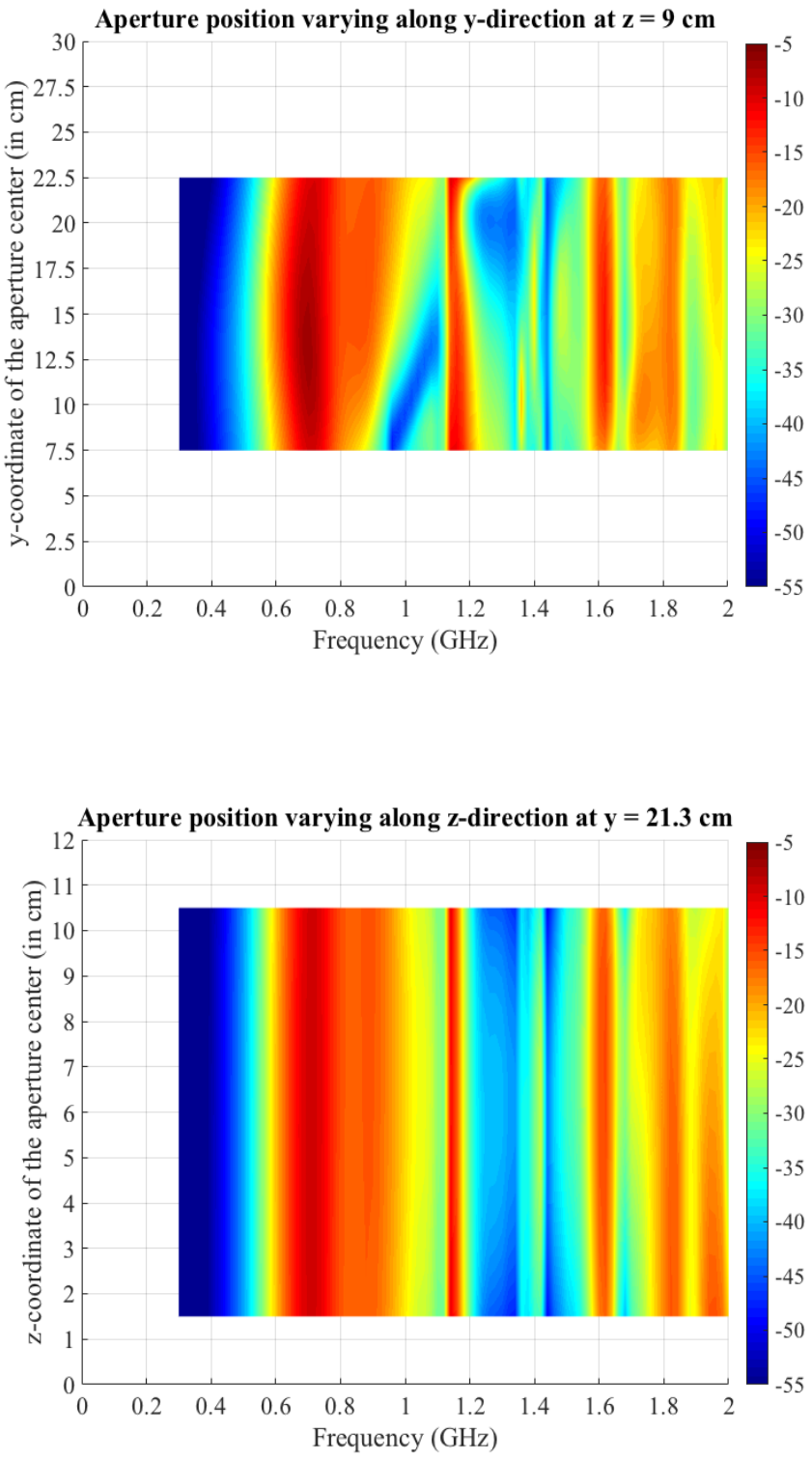

Figure 7.17. Current responses induced on the wire at position 1 using 28 (sparse-y) positions of 15 cm × 3 cm aperture in ANN training.

x varies from 0 to 30 cm, y varies from 0 to 30 cm and z varies from 0 to 12 cm in equation (7.12) and (7.13). The resonant frequencies of the cavity modes (either TE or TM) are given by equation (5.8) in Chapter 5. Cavity modes with n = 0, 1, 2, 3, and p = 0, 1 have resonant frequencies below 2 GHz. The sinusoidal variation of the fields within the cavity are therefore overall greater in the y-dimension than in z-dimension. For example, the maximum of n = 3 gives 3 sinusoidal half cycles in the y dimension while p = 1 gives only a single have-cycle variation in the z dimension. Hence, a greater variation of induced current on the wire is expected when the aperture is moved in the y direction versus the z direction.

7.4.3. 9.5 cm × 9.5 cm aperture

The ability of the ANN to predict the sensitivity of the current induced on a wire probe to the position of a 9.5 cm × 9.5 cm aperture on the EUT front face is now considered. The aperture positions on the EUT front face used for training are shown by the black squares in Figure 7.18. Points A_3 and A_4 are the center positions of the aperture used for validating the trained ANN model against numerical simulations. Table 7.9 shows the performance of ANN training. Figure 7.19 compares the ANN estimation of the induced current and direct numerical simulation when the aperture is centered at point A_3 and A_4.

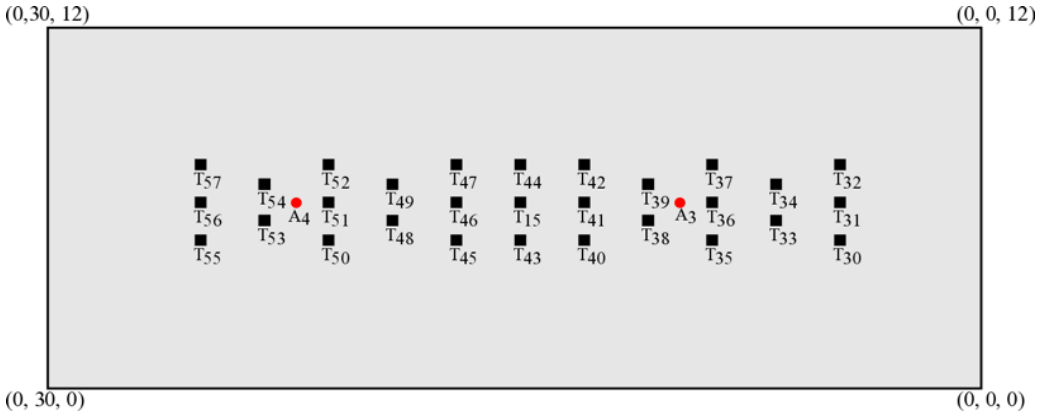

Figure 7.18. Center positions of 9.5 cm × 9.5 cm aperture used as training (shown by black square) and testing (shown by red circles).

Table 7.9. Summary of ANN performance with 9.5 cm × 9.5 cm aperture.

Number of training aperture positions	Total training samples	Total testing samples	Mean percentage error	
			Training datasets	Testing datasets
29	2494	172	1.77 %	1.91 %

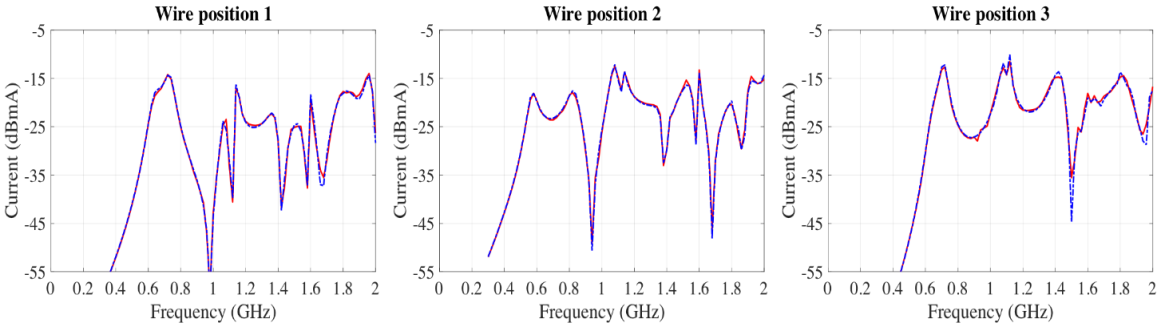

(a) Aperture at A_3

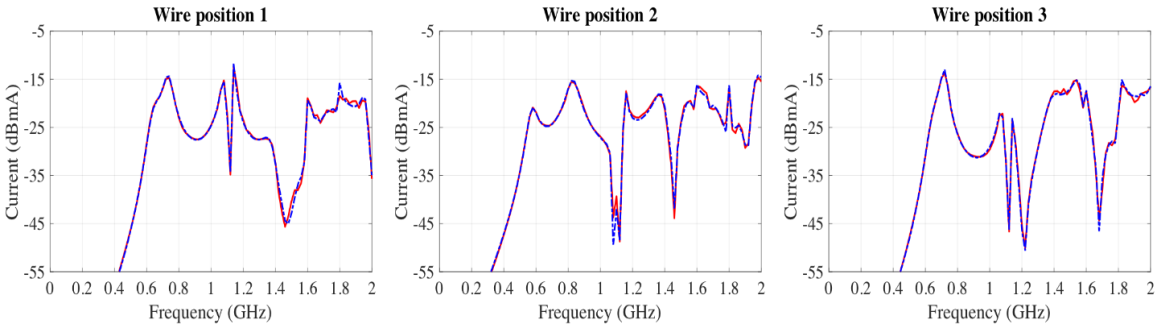

(b) Aperture at A_4

Figure 7.19. Comparison of ANN (solid red line) and the numerical simulation (dash-dot blue line) current responses on the wire with 9.5 cm × 9.5 cm aperture.

The RMS errors between the ANN estimates and numerical simulations are shown in Table 7.10 for all test aperture positions and wire positions. The errors vary from 0.52 to 1.26 dB among all cases. The error in the prediction of the deep null at 1.55 GHz is mainly responsible for the relatively high RMS error of 1.26 dB in Table 7.10. The largest difference in the peak magnitude

of 2.7 dB is observed at 1.8 GHz with wire position 1 and aperture position A_4. Overall, very good agreement between the ANN and numerical simulations is observed. Hence, the ANN model that was trained with this aperture configuration and sampling is accepted as validated.

Table 7.10. RMS error (in dB) between ANN and numerical simulation results with aperture centered at A_3 and A_4.

Aperture center position	Wire position 1	Wire position 2	Wire position 3
A_3	0.72	0.52	1.26
A_4	0.72	0.86	0.6

Figure 7.20 shows the dependence of the induced current on the wire to the aperture position. With these aperture dimensions, the aperture center position can be varied from 4.75 cm to 25.25 cm in the y direction and from 4.75 cm to 7.25 cm in the z coordinate. Again, the current is much more sensitive to y-dimension (perpendicular to the wire probe) changes in the aperture position than z-dimension (parallel to the wire) changes.

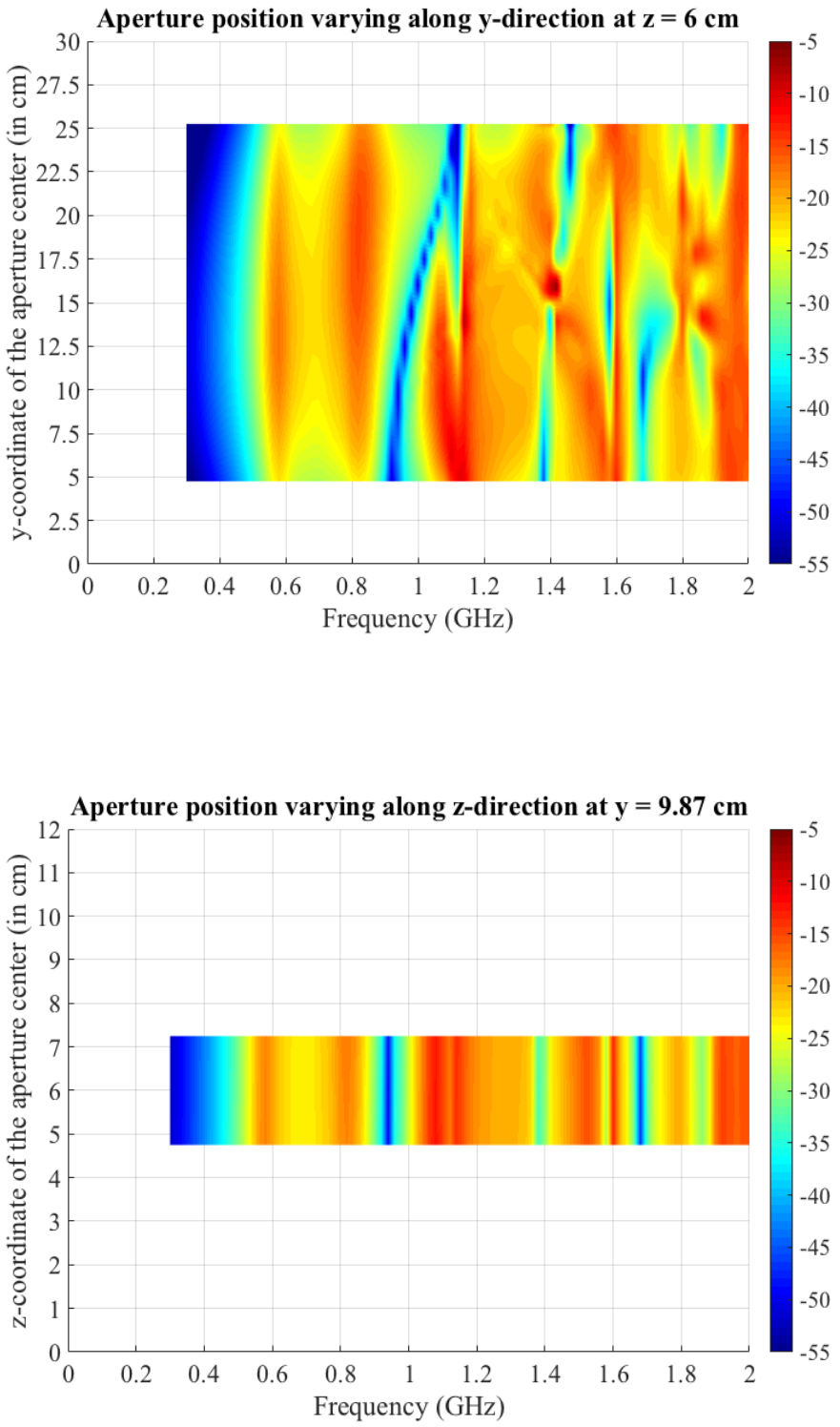

Figure 7.20. Current responses induced on the wire at position 2 with the variation in the center position of 9.5 cm × 9.5 cm aperture.

7.4.4. 6.7 cm × 6.7 cm aperture

Finally, the ability of the ANN to predict the dependence of the induced current on the positon of a 6.7 cm × 6.7 cm aperture on the EUT front face was evaluated. The aperture positions on the EUT front face used for training are shown by black squares in Figure 7.21. Points A_8, A_9 and A_{10} are the test aperture center positions used for validating the trained ANN model against numerical simulation. Figure 7.22 compares the ANN and numerically simulated current responses on the wire for all three wire positions and the aperture placed at position A_8, A_9, and A_{10}.

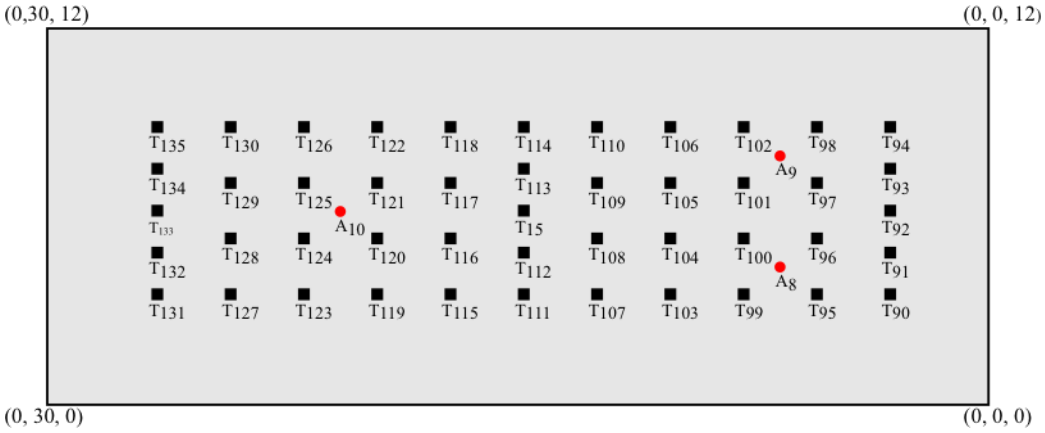

Figure 7.21. Center positions of 6.7 cm × 6.7 cm aperture used as training (shown by black square) and testing (shown by red circles).

Table 7.11. Summary of ANN performance with 6.7 cm × 6.7 cm aperture.

Number of training aperture positions	Total training samples	Total testing samples	Average percentage error	
			Training datasets	Testing datasets
47	4042	258	2.27 %	2.57 %

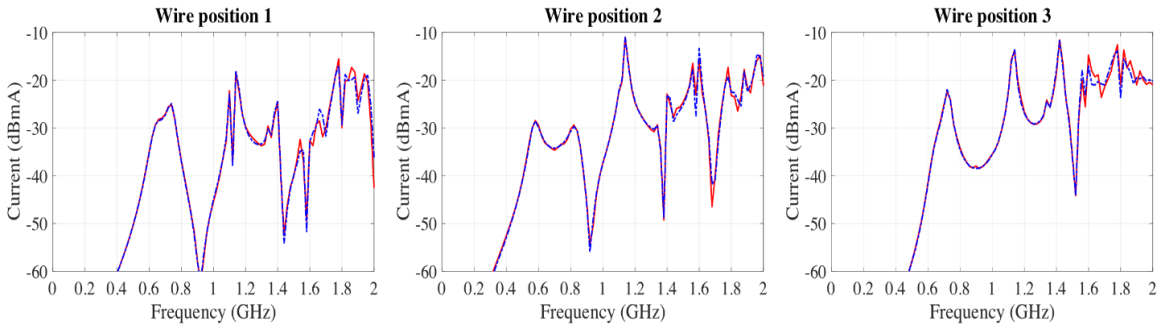

(a) Aperture at A_8

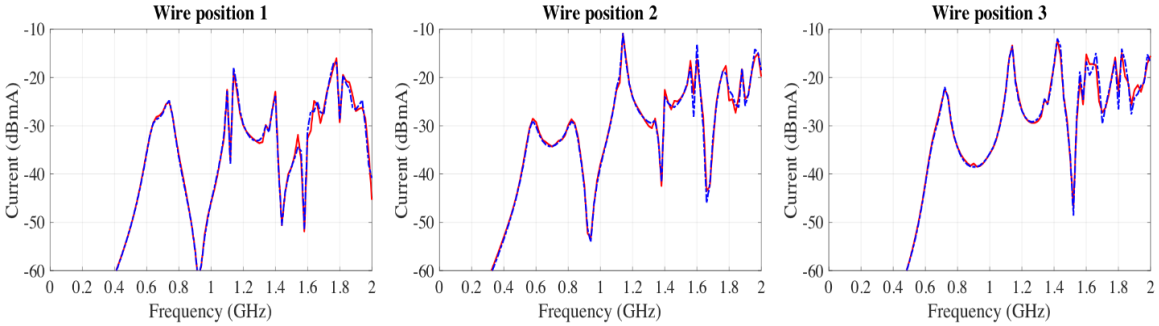

(b) Aperture at A_9

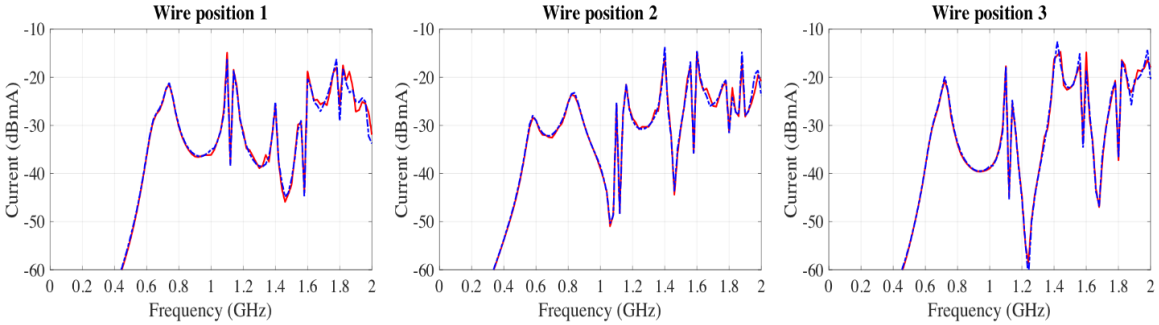

(c) Aperture at A_{10}

Figure 7.22. Comparison of ANN (solid red line) and the numerical simulation (dash-dot blue line) current responses on the wire with 6.7 cm × 6.7 cm aperture.

The RMS errors for all test aperture positions and wire positions are shown in Table 7.12. They vary from 0.84 to 1.31 dB across all cases. The RMS error is 1.31 dB with wire position 1 and aperture position at A_8. Figure 7.22 (a) shows that this high RMS error is mainly due to a slight frequency shift of the resonance at approximately 1.7 GHz and difference in null depth at 2 GHz. The maximum difference in the peak magnitude of 4.32 dB occurs at 1.86 GHz with wire position 1 and aperture position A_{10}. Overall, very good agreement between the ANN and numerical simulations is again observed. Hence, the ANN model that was trained with this aperture can be accepted as validated.

Table 7.12. RMS error (in dB) between ANN and numerical simulation results with aperture centered at A_8, A_9 and A_{10}.

Aperture center position	Wire position 1	Wire position 2	Wire position 3
A_8	1.31	1.07	0.96
A_9	1.05	1.01	1.09
A_{10}	1.07	0.84	1

Figure 7.23 shows the change in the induced wire current with changing aperture position. Here the aperture center position can be varied from 3.35 cm to 26.65 cm in the y dimension and from 3.35 cm to 8.65 cm in z-coordinate. Similar induced-current behavior to that with the 15 cm × 6 cm, 15 cm × 3 cm, and 9.5 cm × 9.5 cm apertures is observed here.

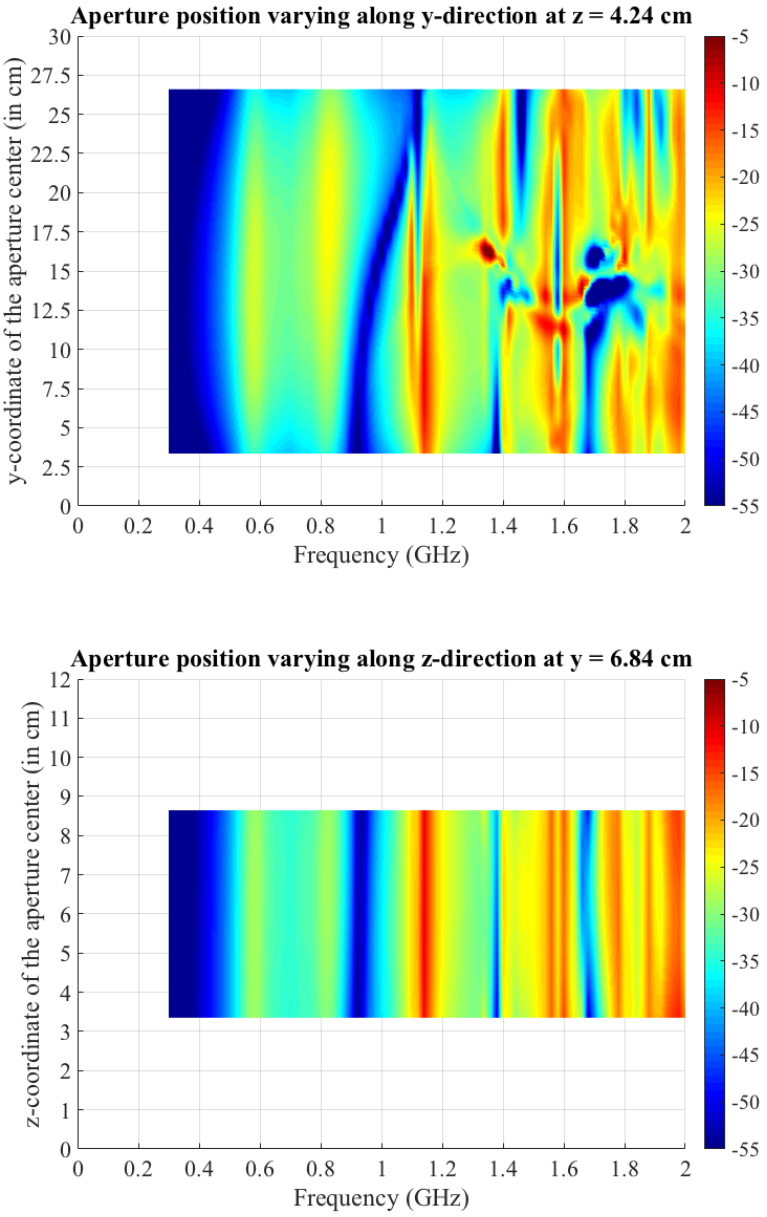

Figure 7.23. Current responses induced on the wire at position 2 with the variation in the center position of 6.7 cm × 6.7 cm aperture.

7.5. Current responses due to different aperture configuration using ANN

Figure 7.24 compares the induced current on the wire at position 2 with rectangular and square apertures of the same area. Stronger resonant responses occur with the rectangular aperture at frequencies below 1 GHz. Siah *et al.* [41] observed a greater shielding effectiveness by enclosures

with square apertures than with rectangular apertures of the same area with EUTs similarly sized to the one in Figure 7.5. (Note that shielding effectiveness is defined with a single uniform plane wave of magnitude 1 V/m normally incident on the aperture face.) The greater the shielding effectiveness of the EUT enclosure, the lower the strength of the field penetrating the aperture into the cavity and hence lower the resonant responses of the current induced on the wire. It was suggested in [41] that the greater shielding effectiveness of the EUT enclosure with square aperture is due to a shift in aperture resonance from lower frequencies to higher frequencies.

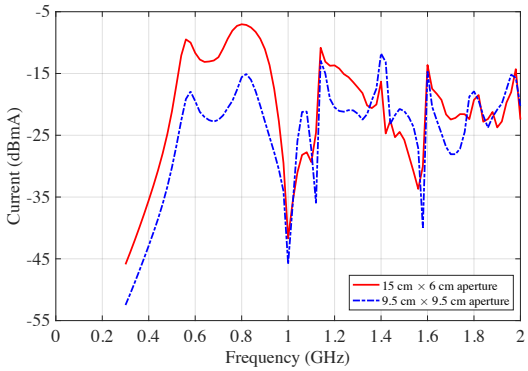

(a)

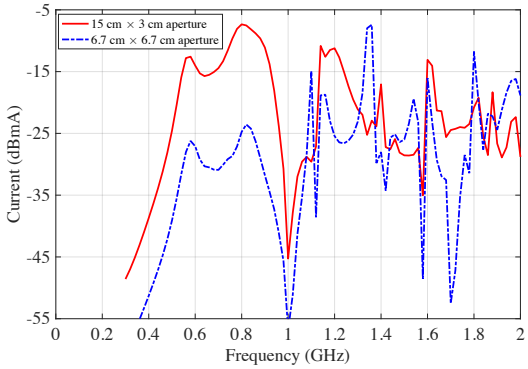

(b)

Figure 7.24. Current responses induced on the wire with the aperture position at point (0, 16.5, 6) in cm having aperture area of approximately (a) 90 cm^2 and (b) 45 cm^2.

It was discussed in Chapter 5 that the strong resonant responses in the induced current are due to a cavity formed by the EUT, wire probe, and the aperture. Figure 7.25 and 7.26 show the resonant frequencies due to the EUT cavity, the wire probe, and all the aperture configurations, when

considering each of them separately. The mutual interactions of the cavity, the wire probe, and the aperture perturb these resonances, as discussed in Chapter 5.

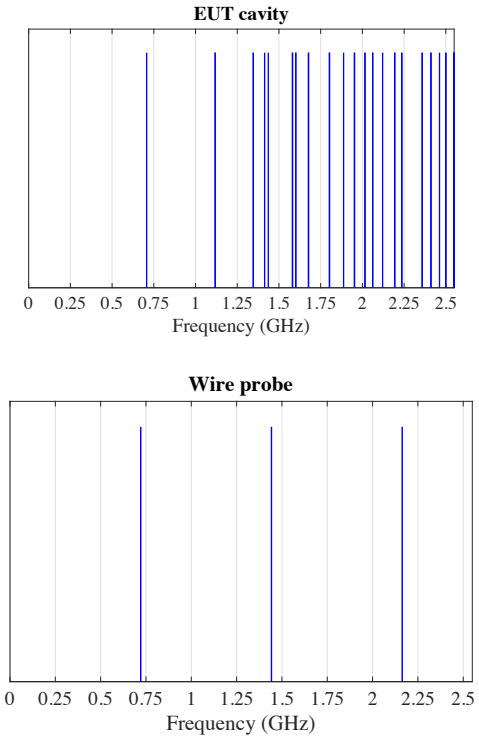

Figure 7.25. Resonant frequencies due to EUT cavity and wire probe

Figure 7.26 shows that the aperture resonances shift from 1 GHz to 1.58 GHz when rectangular aperture of dimension 15 cm × 6 cm is replaced by a square aperture of dimension 9.5 cm × 9.5 cm. Therefore, the aperture resonance due to 9.5 cm × 9.5 cm aperture is less to the resonant responses of induced current below 1 GHz than the 15 cm × 6 cm aperture. The contribution of aperture resonances towards the induced current responses below 1 GHz becomes smaller as the aperture resonance is shifted towards higher frequencies. With the 6.7 cm × 6.7 cm aperture, there are no aperture resonances at frequencies below 2 GHz. Thus, lowest induced current below 1 GHz occurred with the 6.7 cm × 6.7 cm aperture.

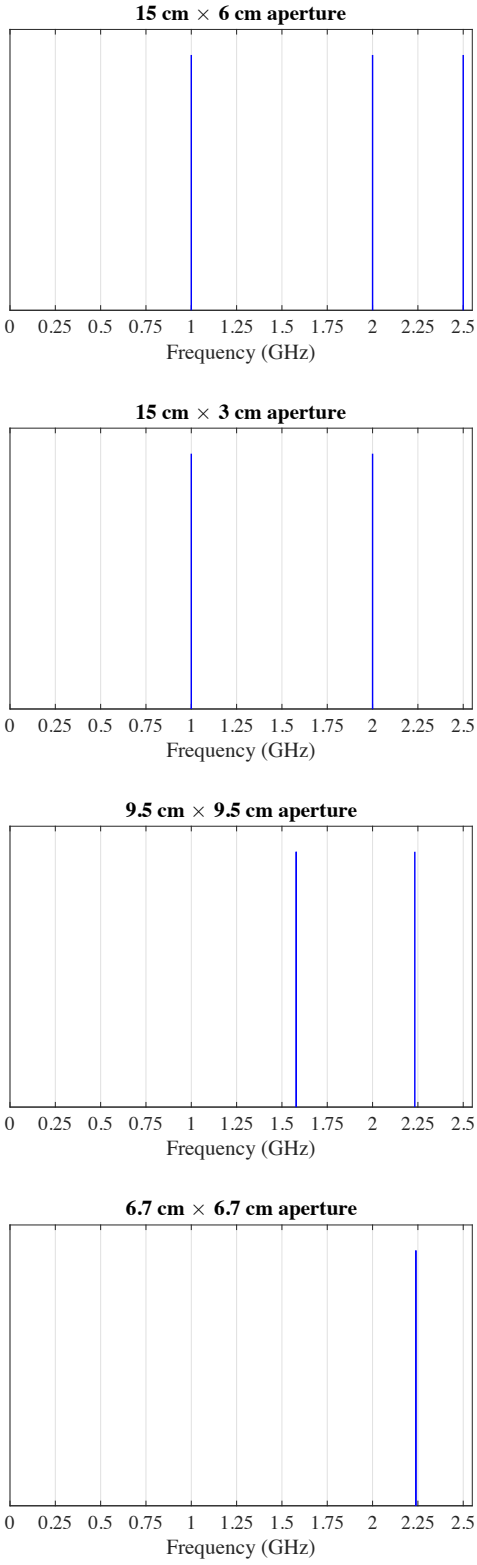

Figure 7.26. Resonant frequencies due to all aperture configurations

7.6. Specifications of ANN model

The ANN was trained for arbitrarily placement of the four aperture configurations shown in Table 7.1, over the frequency range from 300 MHz to 2 GHz. The induced current responses on the wire at three different positions can be obtained from the trained ANN almost instantly for any aperture position. It can therefore serve as an alternative to direct numerical simulation. Table 7.13 shows the test configurations at which the ANN is applicable for predicting the induced current responses.

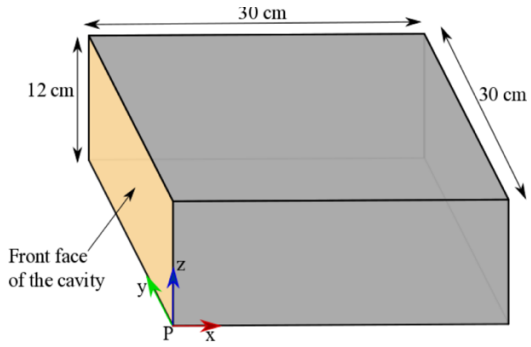

Figure 7.27. Cavity formed by the EUT geometry

Table 7.13. Test limits of ANN model

Cavity Dimension	30 cm × 30 cm × 12 cm
Wire diameter	0.82 mm
Wire length	10.4 cm
Aperture placement	Anywhere on front face of the cavity in Figure 7.27
Aperture dimensions	15 cm × 6 cm, 15 cm × 3 cm, 9.5 cm × 9.5 cm and 6.7 cm × 6.7 cm
Wire position on the cavity floor with reference to Point P (in cm) in Figure 7.27	Position 1(15.6, 4, 0), Position 2(12.5, 12, 0), and Position 3 (24.5, 24, 0)
Frequency range	300 MHz – 2 GHz

7.7. Comparison of ANN accuracy with linear interpolation method

The currents predicted by the ANN at all test aperture positions and wire positions were also compared with linear interpolation of the responses obtained at the training positions. The MATLAB implementations of the interpolation algorithms were used. Table 7.14 shows the RMS error in the induced currents with the wire at all three test positions when the 15 cm × 6 cm aperture was centered at the test aperture positions. Similarly, Table 7.15, 7.16 and 7.17 shows the errors when the 15 cm × 3 cm, 6.7 cm × 6.7 cm, and 9.5 cm × 9.5 cm apertures, respectively, were placed at their test positions. In linear interpolation method, the current response was linearly interpolated at positions other than the training aperture positions, but at the training frequencies from 300 MHz to 2 GHz stepping at 20 MHz. The RMS errors in all cases ranges from 0.52 to 1.36 dB with the ANN, and 0.28 to 1.85 dB with linear interpolation. Figure 7.28 shows the case where largest RMS error was observed with ANN. Figure 7.29 shows the case where largest RMS error was observed with linear interpolation. ANN shows smaller RMS error with 9.5 cm × 9.5 cm aperture in most cases. However, From Table 7.14, 7.15, and 7.16, there are many cases where the RMS error with ANN is greater than that of Linear interpolation. Therefore, the ANN performance in many cases is actually less effective compared to linear interpolation.

Table 7.14. RMS error (in dB) of all cases with 15 cm × 6 cm aperture in ANN and linear interpolation.

Test aperture position	Wire position	ANN	Linear Interpolation
A_1	1	0.74	0.81
A_1	2	0.7	1
A_1	3	0.63	0.28
A_2	1	0.87	0.46
A_2	2	0.83	0.58
A_2	3	1.04	0.6

Table 7.15. RMS error (in dB) of all cases with 15 cm × 3 cm aperture in ANN and linear interpolation.

Test aperture position	Wire position	ANN	Linear Interpolation
A_5	1	1.36	1.09
A_5	2	0.78	0.9
A_5	3	1.35	1.13
A_6	1	1.17	1.48
A_6	2	0.99	1.2
A_6	3	1.17	0.91
A_7	1	0.61	0.33
A_7	2	0.71	0.65
A_7	3	0.98	0.55

Table 7.16. RMS error (in dB) of all cases with 6.7 cm × 6.7 cm aperture in ANN and linear interpolation.

Test aperture position	Wire position	ANN	Linear Interpolation
A_8	1	1.31	1.25
A_8	2	1.06	0.52
A_8	3	0.96	0.79
A_9	1	1.05	1.24
A_9	2	1.01	0.64
A_9	3	1.09	0.88
A_{10}	1	1.07	1.28
A_{10}	2	0.84	0.81
A_{10}	3	1	1.54

Table 7.17. RMS error (in dB) of all cases with 9.5 cm × 9.5 cm aperture in ANN and linear interpolation.

Test aperture position	Wire position	ANN	Linear Interpolation
A_3	1	0.72	1.85
A_3	2	0.52	0.64
A_3	3	1.26	1.07
A_4	1	0.72	0.5
A_4	2	0.86	1.28
A_4	3	0.6	0.83

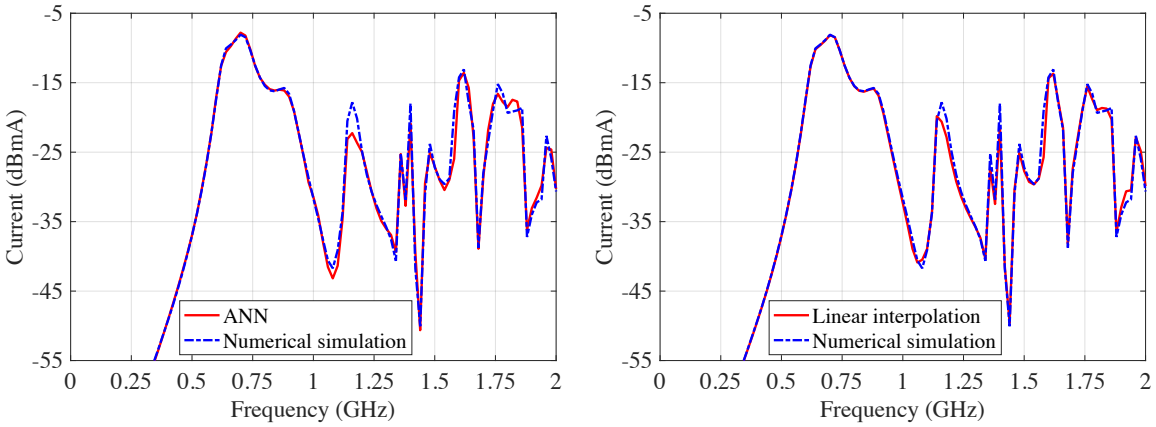

Figure 7.28. ANN interpolation versus linear interpolation with 15 cm × 3 cm aperture at A_5 and wire position 1.

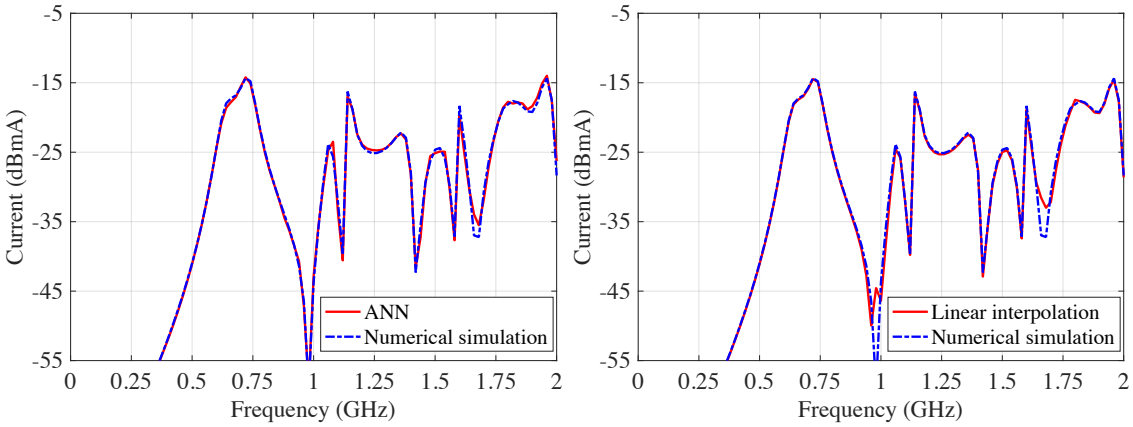

Figure 7.29. ANN interpolation versus linear interpolation with 9.5 cm × 9.5 cm aperture at A_3 and wire position 1.

7.8. ANN performance with finer frequency sampling

The ANN performance was also examined when interpolating the current responses to both new aperture positions and frequencies simultaneously from the existing training data. The left side of Figure 7.30 compares the ANN prediction of the current at wire position 2 and the 6.7 cm × 6.7 cm aperture at position A_8 with direct numerical simulation. Part (a) of the figure shows the

interpolation of the aperture position only at the training frequencies (20 MHz sampling) for reference. Part (b) shows the interpolation of both the aperture position and the frequency to an equivalent 10 MHz sampling rate. The agreement is worse with 10 MHz sampling than with 20 MHz sampling, especially at frequencies above 1.3 GHz. For example, the peak magnitude difference of 8.45 dB is observed at 1.41 GHz (more than the 6.2 dB maximum error that was observed experimentally) when 10 MHz frequency sampling was used. With no frequency interpolation (20 MHz sampling), the highest magnitude is less than 1.5 dB near the same frequency. Figure 7.30 (b) shows that the ANN failed to capture the sharp peak occurring at 1.43 GHz. Additionally, large magnitude differences of more than 13 dB were observed at 1.59 GHz and 1.67 GHz due to a shift in the resonant peaks and nulls.

The performance of linear interpolation with 10 MHz frequency sampling is shown in the right side of Figure 7.30. A peak magnitude error of 6.4 dB occurs at 1.43 GHz. Table 7.18 shows the RMS error for ANN and linear interpolation associated with 10 MHz and 20 MHz frequency sampling. It shows that the RMS error increases when frequency interpolation is used to increase the effective sampling rate is changed from 20 MHz to 10 MHz for both ANN and linear interpolation.

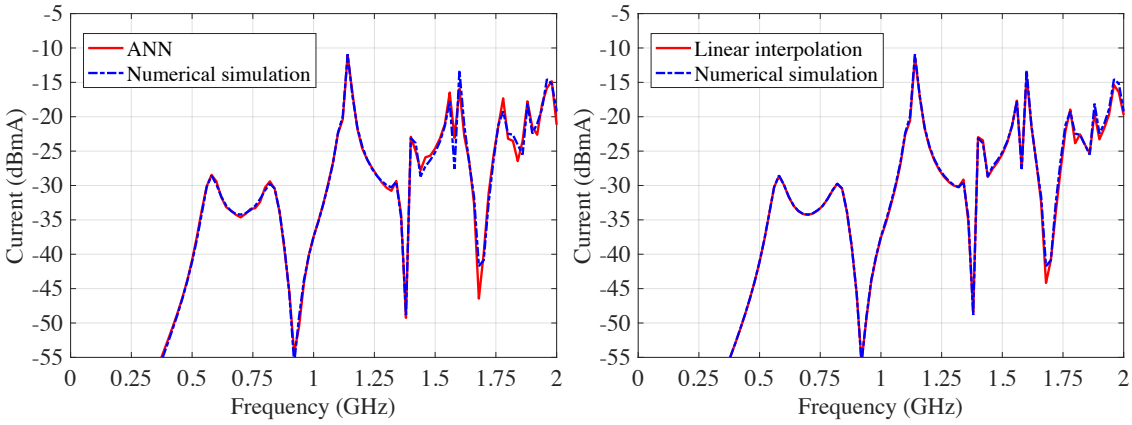

(a) 20 MHz sampling

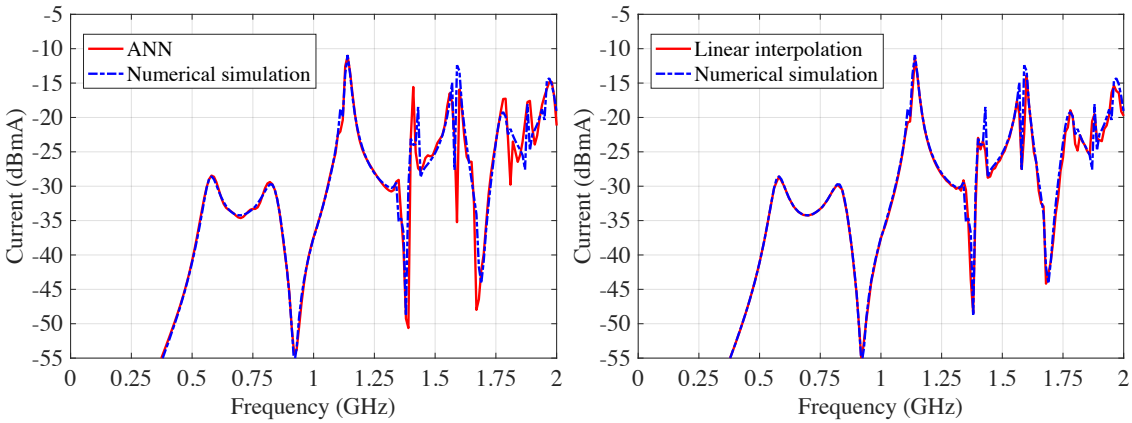

(b) 10 MHz sampling

Figure 7.30. ANN interpolation versus linear interpolation with 6.7 cm × 6.7 cm aperture at position A_8 and wire position 2.

Table 7.18. RMS error (in dB) with 10 MHz and 20 MHz frequency sampling results in Figure 7.30.

Frequency sampling	ANN	Linear interpolation
20 MHz	1.07	0.52
10 MHz	3.12	1.5

With ANN, the RMS error with 10 MHz sampling is 3.12 dB, slightly above the experimentally observed RMS error in Table 7.18. Figure 7.24 shows stronger resonances with high peak to null ratios in the current responses appear at frequencies above 1 GHz with the 6.7 cm × 6.7 cm aperture that with other aperture configurations. This is due to the high-quality factor (Q) established within an EUT with a small aperture size. In a high Q-cavity environment, the current responses are highly sensitive to a slight change in the frequency. Thus, the large RMS error in the ANN predictions in this case suggest that ANN performs poorly in capturing sharp resonant peaks and nulls.

The ANN performance was also observed with the 15 cm × 6 cm aperture, giving a lower Q within the EUT than the 6.7 cm × 6.7 cm aperture. Figure 7.31 compares ANN and the direct numerical simulation when the 15 cm × 6 cm aperture was placed at position A_2 with wire at position 1. The RMS error in ANN does not change significantly when interpolating the frequency sampling rate from 20 MHz to 10 MHz, as shown in Table 7.19. From Figure 7.31 (b) shows that resonances and nulls are less frequent than in Figure 7.30 (b). Moreover, a lower peak-to-null ratio occurs at frequencies above 1 GHz in Figure 7.31 (b) compared to that in Figure 7.30 (b). So, the current responses in this case are less sensitive to frequency changes than with the 6.7 cm × 6.7 cm aperture. Thus, both ANN and linear interpolation are better able to interpolate to new frequencies with the lower quality factor EUT with a 15 cm × 6 cm aperture.

Figure 7.30 and 7.31 show that ANN is not effective when predicting the current response of high Q EUTs. They also show that linear interpolation performs better than ANN when interpolating to new frequencies.

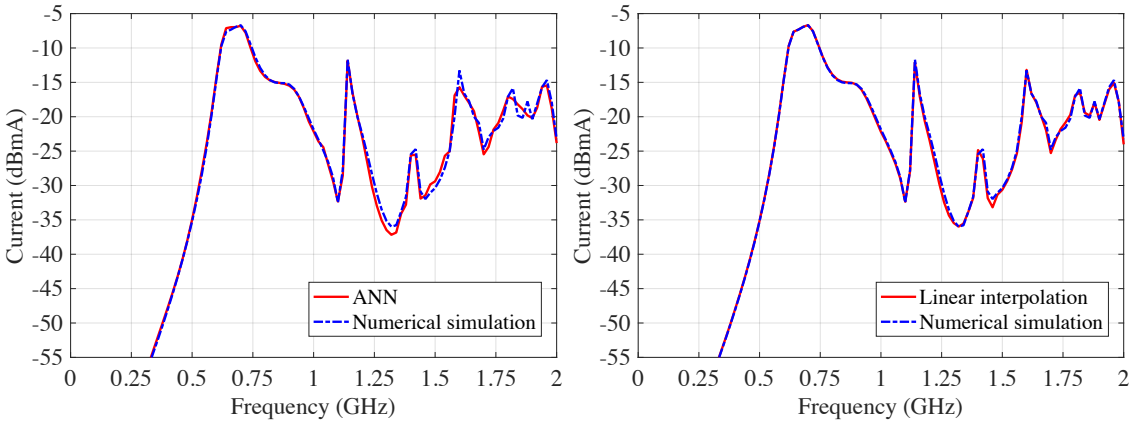

(a) 20 MHz sampling

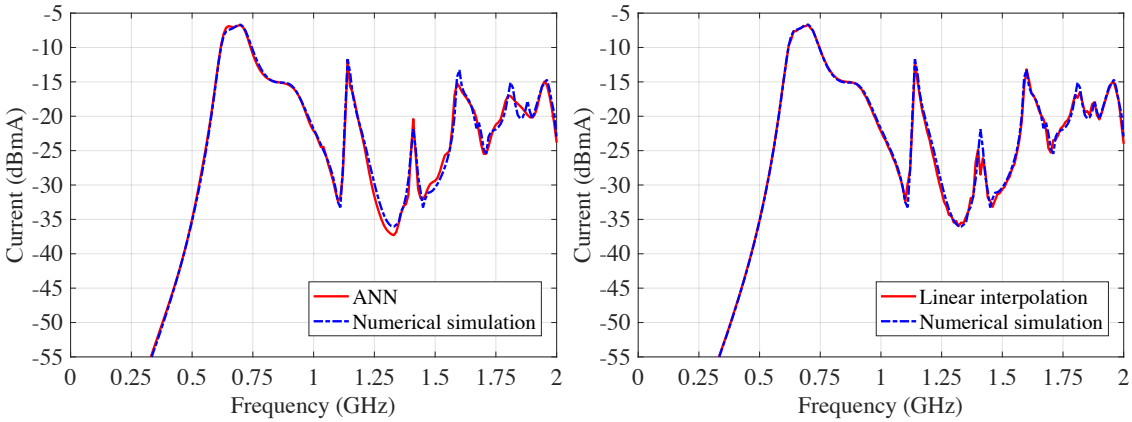

(b) 10 MHz sampling

Figure 7.31. ANN interpolation versus linear interpolation with 15 cm × 6 cm aperture at position A_2 and wire position 1.

Table 7.19. RMS error (in dB) with 10 MHz and 20 MHz frequency sampling results in Figure 7.31.

Frequency sampling	ANN	Linear interpolation
20 MHz	0.87	0.46
10 MHz	0.88	0.85

7.9. Conclusion

In this chapter, an artificial neural network (ANN) was trained in an attempt to predict the dependence of sharp resonant peaks in the current responses on the wires within partially shielded enclosures exposed to random reverberation chamber electromagnetic fields on small changes in the EUT geometry. The geometrical parameter considered was the position of the differently shaped apertures on the EUT front face. The ANN was trained for this geometrical parameter over the frequency range from 300 MHz to 2 GHz. The trained ANN model can nearly instantly calculate the induced current responses on the wire, thus serving as alternative to direct numerical simulations. This model is valid for calculating the resonant responses of the induced current on the test limits shown in Table 7.13. The ANN was used to study the dependency of the induced current responses on the aperture positions. The induced current responses vary significantly when the aperture is moved in the y dimension, very little when moved in z-dimension. This is due to the modal structure of the field within the cavity, which changes more in y dimension than in z dimension. The behavior of the induced current responses on different aperture shapes was also analyzed using the ANN. It was found that lowest frequency resonant responses are lower with a square aperture than with a rectangular aperture of the same area, due to a shift in the aperture resonance from lower to higher frequency. Finally, the accuracy of the ANN was also compared with that of linear interpolation. It shows that the ANN is less effective for predicting the resonant response of induced current compared to linear interpolation. An additional test including interpolation to a finer frequency sampling rate shows that ANN performs poorly in identifying the sharp resonances and deep nulls in the current responses, especially when a high Q cavity EUT environment is modeled.

The results of this chapter show that ANN can be trained to rapidly provide a prediction of the current response of an EUT that consists of a resonant enclosure containing an aperture and an internal measurement probe under changing aperture positions and frequency. However, an ANN

is not effective in recognizing the sharp resonant peaks and nulls in the current response at EUT configurations and frequencies away from training configuration. Additionally, ANN actually proved to be less effective than simple linear interpolation when the EUT induced strongly resonant responses. Thus, ANN is not a viable method for interpolating the current response in a highly resonant cavity environment despite its expected ability to directly recognize response patterns.

CHAPTER 8

CONCLUSIONS AND FUTURE WORK

8.1. Conclusions

An in-house CEM code was used to calculate the current response of an EUT (equipment under test) when it was exposed to a random electromagnetic field within a reverberation chamber. The EUT consisted of a single wire attached to the interior wall of a cavity with an aperture on one of its faces. This work first enhanced the in-house CEM code by implementing higher-order LN/QT vector basis functions. These basis functions allow the use of larger triangular patches in modeling the EUT conducting surfaces than the RWG basis functions used in earlier work [3] to achieve similar accuracy in the computed results. Hence, the required accuracy can be obtained with the less computational effort using LN/QT basis functions. This was confirmed by a comparison of the performance of LN/QT and RWG basis functions for three different test cases. One of the test cases considered was to calculate the current response on the EUT due to a single uniform plane wave excitation in the frequency range from 300 MHz to 1 GHz. In that test case, the total computational time was reduced by five times to achieve the same accuracy with LN/QT basis function than with RWG basis functions. The primary advantage of using LN/QT basis functions is that it gives the accurate results without refinement of the mesh near the aperture edges. Thus, the computational workload for simulating the response of an EUT can be significantly reduced using LN/QT basis functions.

Anechoic chamber measurement was performed in Chapter 5 to validate the induced currents on a wire probe within a partially shielded cavity given by the enhanced version of in-house CEM code. A test case was considered that exposes the EUT to a single, vertically polarized uniform plane wave that is normally incident on the face of the EUT that contains the aperture. The EUT was similar to the one considered in [3], but with the face containing the aperture replaced by a thinner aluminum plate. This change was made because the multi-level fast multipole algorithm (MLFMA) solver used for the numerical simulations is not able to model electrically thick walls, leading to an under-prediction of aperture resonances in the frequency range from 3.5 – 4.5 GHz in [3]. The measured and simulated results were compared with three different wire positions on the cavity floor in the frequency range from 300 MHz to 8.5 GHz. The measured and simulated currents at the resonances of the EUT enclosure agreed to within 3.6 dB with all three wire-probe positions considered. Such changes are consistent with that expected with the unavoidable small differences between the physical and simulated EUT geometries. Overall, very good agreement between the measured and simulated probe currents was achieved, especially in the frequency range from 3.5 – 4.5 GHz. An analysis using Frequency Selective Validation (FSV) package [25] showed good agreement between the measured and simulated currents with ADM and FDM and fair agreement with GDM. In Chapter 3, FSV was shown to be somewhat pessimistic in assessing agreement between signal responses that include strong nulls and resonance peaks. FSV rates better agreement in ADM, FDM, and GDM using the thin aperture face than when the thicker face was used in earlier work [3]. Thus, the validity of the numerically simulated results has been confirmed for this test case.

Further measurements were performed within a mechanically stirred reverberation chamber to validate the numerically simulated mean current induced on the EUT by a random field. In the numerical simulation, the random field was represented by a discrete spectrum of plane waves as given in [19]. The differences in the measured and the simulated mean current magnitude induced

on a wire were consistent with that expected due to a finite number of samples used to find the measurement mean and the geometrical differences between the physical and simulation model of the EUT. Overall, excellent agreement between the numerical simulation and the measurements was achieved. An FSV comparison of the simulations and measurements gave very good agreement in ADM and good agreement in FDM and GDM. As discussed, FSV understates the agreement when the current responses include strong resonances and nulls. Thus, the numerical approach for calculating the EUT response due to a random reverberation chamber field represented by discrete plane wave spectrum model has been experimentally validated. Additionally, a technique to extract the current induced at the EUT measurement port from the S_{21} measured between the source antenna and the EUT measurement port has also been confirmed as validated.

This work improves upon DREAM by rigorously defining the transmission loss parameter. An accurate prediction of the induced current response at a given test point within an EUT due to a random field can be obtained by using numerical simulation. The average power coupled by the aperture of an EUT due to a random field with RMS field level of E_0 can be obtained by

$$P_A = S_c\langle A_e\rangle = \frac{{E_0}^2}{\eta}\langle A_e\rangle \tag{8.1}$$

where S_c is the mean power density within the reverberation chamber as given in [35], η is the intrinsic impedance of the medium, and A_e is the effective aperture area. DREAM generates a statistical distribution of effective aperture area due to electromagnetic field randomly coupled over a uniformly distributed angle of incidence. The power received at test point q within an EUT due to a random field is $P_r = |I_q|^2 Z_q$, where I_q and Z_q is the induced current and load impedance, respectively, at test point q. Thus, the transmission loss at test point q for a particular EUT configuration can be determined by

$$L = \frac{P_r}{P_A} = \frac{|I_q|^2 Z_q \eta}{{E_0}^2 \langle A_e \rangle}. \tag{8.2}$$

There is a need to predict the changes in sharp resonant peaks in the current responses when EUT geometrical parameters are varied. Such resonant peaks can cause failures in electronic devices. Therefore, various possible geometrical configurations must be considered. In Chapter 7, an artificial neural network (ANN) was trained to eliminate the need to repeat the numerical simulation under all possible frequencies of operation and geometrical configurations. The changing geometrical parameter considered was the position of the differently shaped apertures on the EUT front face. The ANN was trained for changing position of an aperture of a given shape over the frequency range from 300 MHz to 2 GHz. It was shown that the trained ANN can nearly instantly give a prediction of the induced current under changing aperture positions and frequency. However, ANN proved to be less effective in estimating the changes in strong resonant responses induced on the wire with changing aperture position than simple linear interpolation. Overall, ANN performs poorly in recognizing the sharp resonances and nulls when interpolating the current responses when the EUT geometrical parameters and operating frequencies differ from the training configurations, especially when a high Q cavity EUT environment is modeled. Thus, ANN is not a promising method for interpolating the current response in a highly resonant cavity environment and reducing the computational workload needed to approximate under EUT configurations directly used for training.

8.2. Directions to the future work

In this work, the reverberation chamber measurement confirms that the statistics of a random field within a mechanically stirred reverberation chamber follows Rayleigh distribution. However, He and Marvin [63] concluded that a field coupled through a small aperture on an EUT follows a non-Rayleigh distribution in magnitude. In that work [63], the combination of mechanical and frequency

stirring method was used to collect the number of independent samples. West *et al.* [62] suggest that the current magnitude sampled at different frequencies were obtained from different Rayleigh distribution with their statistics given by equation (7.6) and (7.7), due to the frequency dependence of the linear operator in equation (6.7). Thus, overall distribution of the current samples is non-Rayleigh when frequency stirring is used. Whereas in the case of mechanical stirring, current samples are obtained from the same Rayleigh distribution at each frequency. West *et al.* [62] also performed statistical test using Anderson-darling goodness-of-fit [24] on the samples obtained from the combination of mechanical and frequency stirring with the same EUT as shown in Figure 5.4. The results of this statistical test show that the overall distribution deviates significantly from Rayleigh. Hence the expected distribution of the field or current samples is not Rayleigh when frequency stirring is used. Future work should be focused on exploring the field distribution within a reverberation chamber when frequency stirring is used.

As observed in Chapter 7 that the response of mean current magnitude on an EUT due to a random field changes significantly with the aperture shape, size and position, and wire position. Similar behavior in the shielding effectiveness of an EUT due to a single uniform plane wave was observed by Olyslagger [7] when changing the location of the internal radiating source (EUT viewed as a source of EMI via reciprocity) and internal metal objects within an EUT. The modeling with ANN was attempted in this work to eliminate the need for repeating the numerical simulation under different EUT geometrical parameters such as aperture shape, size and position, and different excitation frequencies. However, ANN proved to be an inappropriate method for interpolating the current response in a highly resonant environment. Therefore, the future work should be focused on developing a statistical model that can give a relationship between EUT geometrical parameters (including excitation frequency) as input parameters and the current responses on an EUT as the output parameter. The statistical model should be focused on predicting the sharp resonant peaks and nulls in the induced current response on an EUT. The quality factor established within an EUT

depends on the aperture size for fixed enclosure dimensions. As the aperture size decreases, the quality factor established within an EUT increases and thus increases the sensitivity of the current response with the change in the frequencies. Thus, the statistical model must at least consider aperture size and frequency of operation as an input parameter.

REFERENCES

[1] Air Force STTR 2015.A AF15-AT05 Title: “Tool to predict high-power electromagnetic effects on mobile targets”.

[2] J. Tatum, “DREAM: Operator’s Guide for DREAM; Directed RF Energy Assessment Model,” Technical Report, Army Research Laboratory, Adelphi MD, 1996.

[3] V. Rajamani, J. C. West, C. F. Bunting, "Measurement and Simulation of the Induced Current on a Wire Using S-Parameter Method," in *Electromagnetic Compatibility, IEEE Transactions on*, vol.56, no.2, pp.303-310, April 2014.

[4] C. A. Balanis, *Antenna theory: analysis and design*, 3rd ed. Hoboken, NJ: John Wiley, 2005.

[5] W. C. Gibson, *The Method of Moments in Electromagnetics*, 2nd ed., CRC Press, 2015.

[6] M. N. O. Sadiku, *Numerical techniques in electromagnetics with MATLAB*, 3rd ed., CRC Press, 2009.

[7] F. Olyslager *et al*., "Numerical and experimental study of the shielding effectiveness of a metallic enclosure," in *IEEE Transactions on Electromagnetic Compatibility*, vol. 41, no. 3, pp. 202-213, Aug 1999.

[8] Green, David L. "Analysis and evaluation of RF absorbing material in suppressing modes associated with a metallic cavity." (2014).

[9] G. J. Freyer, M. O. Hatfield and M. B. Slocum, "Characterization of the electromagnetic environment in aircraft cavities excited by internal and external sources," *Digital Avionics Systems Conference, 1996., 15th AIAA/IEEE*, Atlanta, GA, 1996, pp. 327-332.

[10] G. J. Freyer and M. O. Hatfield, "Aircraft test applications of reverberation chambers," *Electromagnetic Compatibility, 1994. Symposium Record. Compatibility in the Loop., IEEE International Symposium on*, Chicago, IL, 1994, pp. 491-496.

[11] C. F. Bunting, "Statistical characterization and the simulation of a reverberation chamber using finite-element techniques," in *IEEE Transactions on Electromagnetic Compatibility*, vol. 44, no. 1, pp. 214-221, Feb 2002.

[12] C. F. Bunting and Shih-Pin Yu, "Field penetration in a rectangular box using numerical techniques: an effort to obtain statistical shielding effectiveness," in *IEEE Transactions on Electromagnetic Compatibility*, vol. 46, no. 2, pp. 160-168, May 2004.

[13] V. Rajamani, C. F. Bunting, J. C. West, "Differences in quality factor estimation in frequency and time domain", *Proceedings of the 2012 Asia-Pacific Symposium on Electromagnetic Compatibility (APEMC)*, pp. 505-508, 2012.

[14] C. L. Holloway, H. A. Shah, R. J. Pirkl, W. F. Young, D. A. Hill and J. Ladbury, "Reverberation Chamber Techniques for Determining the Radiation and Total Efficiency of Antennas," in *IEEE Transactions on Antennas and Propagation*, vol. 60, no. 4, pp. 1758-1770, April 2012.

[15] D. A. Hill, "Plane wave integral representation for fields in reverberation chambers," in *IEEE Transactions on Electromagnetic Compatibility*, vol. 40, no. 3, pp. 209-217, Aug 1998.

[16] D. A. Hill, *Electromagnetic fields in cavities: deterministic and statistical theories*. Vol. 35. John Wiley & Sons, 2009.

[17] Musso L., Berat V., Canavero F.G., Demoulin B. (2002). A Plane Wave Monte Carlo Simulation Method for Reverberation Chambers. In: International Symposium on Electromagnetic Compatibility - EMC EUROPE 2002, Sorrento (Italy), September 9-13. pp. 45-50.

[18] F. Moglie and A. P. Pastore, "FDTD analysis of plane wave superposition to simulate susceptibility tests in reverberation chambers," in *IEEE Transactions on Electromagnetic Compatibility*, vol. 48, no. 1, pp. 195-202, Feb. 2006.

[19] J. C. West, C. F. Bunting, V. Rajamani, "Accurate and Efficient Numerical Simulation of the Random Environment Within an Ideal Reverberation Chamber," in *Electromagnetic Compatibility, IEEE Transactions on*, vol.54, no.1, pp.167-173, Feb. 2012.

[20] E. Assefa, J. C. West, V. Rajamani, C. F. Bunting, "Numerical study of currents induced on a partially shielded wire within an ideal reverberation test chamber," in *Electromagnetic Compatibility (EMC), 2012 IEEE International Symposium on*, vol., no., pp.150-155, 6-10 Aug. 2012.

[21] V. Rajamani, C. Bunting and G. Freyer, "Why consider EMC testing in a reverberation chamber," *Electromagnetic Interference & Compatibility, 2008. INCEMIC 2008. 10th International Conference on*, Bangalore, 2008, pp. 303-308.

[22] Freyer, G. J., and M. G. Backstrom, "Comparison of Anechoic & Reverberation Chamber Coupling Data as a Function of Directivity Pattern", IEEE Int. Symposium on EMC, Washington, DC, August 2000.

[23] G. Gradoni, F. Moglie, A. P. Pastore and V. M. Primiani, "Numerical and experimental analysis of the field to enclosure coupling in reverberation chamber and comparison with anechoic chamber," in *IEEE Transactions on Electromagnetic Compatibility*, vol. 48, no. 1, pp. 203-211, Feb. 2006.

[24] M. A. Stephens, Tests Based on EDF Statistics. New York: Marcel Dekker, Inc., 1986, ch. 4, pp. 97–193.

[25] A. M. Duffy, G. Antonini, A. Orlandi, C. Ritota, "The feature selective validation (FSV) method," in *Electromagnetic Compatibility, 2005. EMC 2005. 2005 International Symposium on*, vol.1, no., pp.272-277 Vol. 1, 8-12 Aug. 2005.

[26] FSV Tool User Manual Tool Version 2.0.9L Java, UAq EMC Laboratory, Dept. of Electrical and Information Engineering, University of L'Aquila, Italy.

[27] IEEE Standard for Validation of Computational Electromagnetics. Computer Modeling and Simulations, IEEE Std. 1597.1, 1597.2, 2009.

[28] S. M. Rao, D. R. Wilton, A. W. Glisson, "Electromagnetic scattering by surfaces of arbitrary shape," *IEEE Trans. Antennas Propagat*, vol. AP-30, pp. 409-418, May 1982.

[29] A. F. Peterson, S. L. Ray, and R. Mittra, *Computational Methods for Electromagnetics*. New York: IEEE Press, 1998.

[30] A. F. Peterson, "Mapped Vector Basis Functions for Electromagnetic Integral Equations," Morgan & Claypool Publishers, 2006.

[31] CONCEPT-II, Institut für Theoretische Elektrotechnik, Technische Universität Hamburg-Harburg (TUHH), Germany.

[32] A. F. Peterson, "Higher-order surface patch basis functions for EFIE formulations," in *Antennas and Propagation Society International Symposium, 1994. AP-S. Digest*, vol.3, no., pp.2162-2165 vol.3, 20-24 June 1994.

[33] K. R. Aberegg, A. Taguchi, and A. F. Peterson, Application of higher-order vector basis functions to surface integral equation formulations, *Radio Sci.*, 31(5), 1207–1213, 1996.

[34] M. P. Robinson *et al*., "Analytical formulation for the shielding effectiveness of enclosures with apertures," in *IEEE Transactions on Electromagnetic Compatibility*, vol. 40, no. 3, pp. 240-248, Aug 1998.

[35] D. A. Hill, M. T. Ma, A. R. Ondrejka, B. F. Riddle, M. L. Crawford and R. T. Johnk, "Aperture excitation of electrically large, lossy cavities," in *IEEE Transactions on Electromagnetic Compatibility*, vol. 36, no. 3, pp. 169-178, Aug 1994.

[36] J. De Moerloose, S. Criel, R. De Smedt, E. Laermans, F. Olyslager and D. De Zutter, "Comparison of FDTD and MoM for shielding effectiveness modelling of test enclosures," *IEEE 1997, EMC, Austin Style. IEEE 1997 International Symposium on*

Electromagnetic Compatibility. Symposium Record (Cat. No.97CH36113), Austin, TX, 1997, pp. 596-601.

[37] D. A. Hill, "Electronic mode stirring for reverberation chambers," in *IEEE Transactions on Electromagnetic Compatibility*, vol. 36, no. 4, pp. 294-299, Nov 1994.

[38] M. D. Deshpande, *Electromagnetic Field Penetration Studies*, NASA, 2000.

[39] Z. A. Khan, C. F. Bunting and M. D. Deshpande, "Shielding effectiveness of metallic enclosures at oblique and arbitrary polarizations," in *IEEE Transactions on Electromagnetic Compatibility*, vol. 47, no. 1, pp. 112-122, Feb. 2005.

[40] V. Rajamani, C. F. Bunting, M. D. Deshpande and Z. A. Khan, "Validation of modal/MoM in shielding effectiveness studies of rectangular enclosures with apertures," in *IEEE Transactions on Electromagnetic Compatibility*, vol. 48, no. 2, pp. 348-353, May 2006.

[41] Eng Swee Siah, K. Sertel, J. L. Volakis, V. V. Liepa and R. Wiese, "Coupling studies and shielding techniques for electromagnetic penetration through apertures on complex cavities and vehicular platforms," in *IEEE Transactions on Electromagnetic Compatibility*, vol. 45, no. 2, pp. 245-257, May 2003.

[42] M. A. Khayat and D. R. Wilton, "Numerical evaluation of singular and near-singular potential Integrals," in *IEEE Transactions on Antennas and Propagation*, vol. 53, no. 10, pp. 3180-3190, Oct. 2005.

[43] S. N. Makarov, *Antenna and EM Modeling with MATLAB*. New York, TX, USA; Wiley, 2002, pp. 66-70.

[44] C. Geuzaine and J. F. Remacle, A three-dimensional finite element mesh generator with built-in pre- and post-processing facilities [online], http://gmsh.info/ (Accessed: January 10, 2016).

[45] F. Hecht, Bidimensional anisotropic mesh generator, Technical Report, INRIA, Rocquencourt, 1997 [online], http://www.ann.jussieu.fr/hecht/ftp/bamg/bamg.pdf (Accessed: January 13, 2016).

[46] M. R. Johnson and E. L. Coffey, "Using FSV with far-field patterns," in *Electromagnetic Compatibility (EMC), 2012 IEEE International Symposium on*, vol., no., pp.696-701, 6-10 Aug. 2012.

[47] D. R. Wilton and S. Govind, "Incorporation of edge conditions in moment method solutions," in *Antennas and Propagation, IEEE Transactions on*, vol.25, no.6, pp.845-850, Nov 1977.

[48] Comsol multiphysics users guide: ver. 4.2 © 1998–2011 COMSOL.

[49] Mukherjee, Sovanlal. *An in-silico study of thermos-acoustic computed tomography for external and internal imaging geometry*. Diss. Oklahoma State University, 2013.

[50] D. M. Pozar, *Microwave engineering*, 2nd ed. New York: Wiley, 1997.

[51] C. A. Balanis, *Advanced engineering electromagnetics*, John Wiley & Sons, Inc, 1989.

[52] http://www.ahsystems.com/datasheets/SAS-510-2_Log_Periodic_Antenna_Datasheet.pdf

[53] http://www.ahsystems.com/datasheets/SAS-571_Horn_Antenna_Datasheet.pdf

[54] R. Bakore, V. Rajamani, J. C. West and C. F. Bunting, "Performance evaluation of feature selective validation in a highly resonant environment," *2016 IEEE International Symposium on Electromagnetic Compatibility (EMC)*, Ottawa, ON, 2016, pp. 100-105.

[55] "Electromagnetic compatibility (EMC) — part 4–21: Testing and measurement techniques — Reverberation chamber test methods", *International Electrotechnical Commission 3 rue de Varembé Case postale 131 CH-1211 Genève 20 Switzerland Tech. Rep. IEC 61000-4-21*, 2003.

[56] https://en.wikipedia.org/wiki/Nonlinear_regression

[57] https://en.wikipedia.org/wiki/Artificial_neural_network

[58] V. K. Devabhaktuni, M. Yagoub, Y. Fang, J. Xu, and Q. J. Zhang, "Neural networks for Microwave modeling: Model development issues and nonlinear modeling techniques," *Int. J. RF Microwave Computer-aided Eng.*, Vol. 11, 4-21, 2001.

[59] M. T. Hagan, H. B. Demuth, M. H. Beale, and O. De Jesús, *Neural Network Design*, 2nd ed, 2014.

[60] F. Dan Foresee and M. T. Hagan, "Gauss-Newton approximation to Bayesian learning," *Neural Networks,1997., International Conference on*, Houston, TX, 1997, pp. 1930-1935 vol.3.4.

[61] *Matlab neural network toolbox user's guide version 9. The MathWorks Inc (2016)*

[62] J. C. West, R. Bakore, and C. F. Bunting, "Statistics of the current induced within a partially shielded enclosure in a reverberation chamber," in *Electromagnetic Compatibility, IEEE Transactions*, 2017.

[63] Y. He and A. C. Marvin, "Aspects of field statistiscs inside nested frequency-stirred reverberation chambers," in Proc. 2009 IEEE Int.Symp. Electromag. Compat., 17-21 August, Austin, Texas, 2009, pp. 171–176.

APPENDIX A

A.1. Divergence conforming vector basis function

Divergence conforming basis function can be obtained by following step:

A.1.1. Mapping into simplex coordinate system

As the basis function defined in [29] [30] are in the simplex coordinates. So, each point within the triangular cell needs to be mapped into a simplex coordinate as shown in Figure A.1. Any point within the cell can be written in terms of simplex coordinate as

$$\mathbf{r} = \xi\mathbf{r_1} + \eta\mathbf{r_2} + (1 - \xi - \eta)\mathbf{r_3} \tag{A.1}$$

where $\mathbf{r_1}$, $\mathbf{r_2}$ and $\mathbf{r_3}$ are the position vector of the vertices of triangular patch in Cartesian coordinate system, as shown in Figure A.1. For example, $\mathbf{r_1}$ mapped to (1, 0), $\mathbf{r_2}$ mapped to (0,1) and $\mathbf{r_3}$ mapped to (0, 0) in (ξ, η) plane, where ξ and η are the simplex coordinates. l_{13}, l_{32} and l_{21} are the edge length. Procedure for mapping into simplex coordinate are explained in [29] [30] but only valid for the points in two-dimensional Cartesian coordinate system. In in-house code, point in three-dimensional coordinate system can be mapped to simplex coordinate.

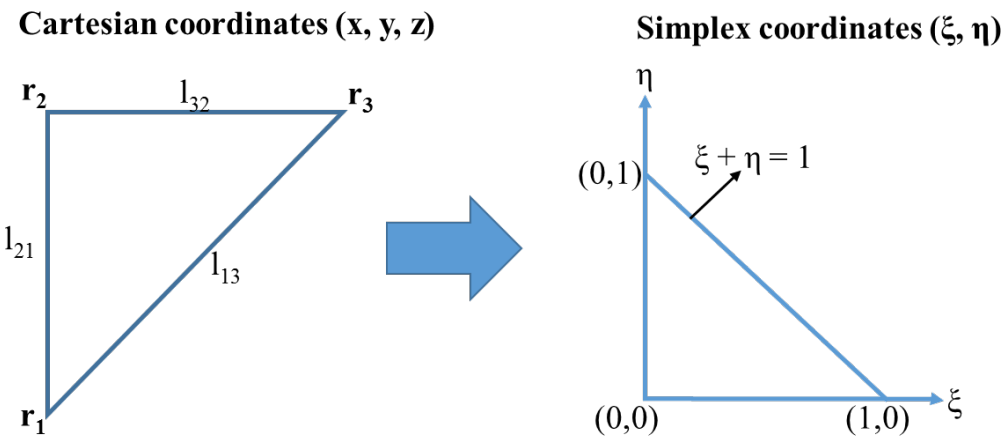

Figure A.1. Mapping of points from Cartesian coordinate to simplex coordinate

A.1.2. Defining the basis function in simplex coordinates

After mapping all the points within the triangular cell into a simplex coordinate system, following are the basis function obtained by using [29] [32]

(i) RWG or Constant Normal/ Linear Tangent (CN/LT) basis functions

Within a triangular cell, three RWG basis functions are assigned that can be written as

$$B(\xi,\eta) = l_{21}(\xi\hat{a}_\xi + \eta\hat{a}_\eta) \quad (A.2)$$

$$B(\xi,\eta) = l_{32}((\xi-1)\hat{a}_\xi + \eta\hat{a}_\eta) \quad (A.3)$$

$$B(\xi,\eta) = l_{13}(\xi\hat{a}_\xi + (\eta-1)\hat{a}_\eta) \quad (A.4)$$

These basis function (from Equation (A.2) to (A.4)) defined on the pair of two cell each sharing a common edge. It gives a constant normal component across the shared edge between the two cells and linear tangential component on the other two edges of the cell.

(ii) Linear Normal/ Quadratic Tangent (LN/QT) basis function

Within a triangular cell, eight basis functions are assigned. Six of these functions can be expressed as

$$B(\xi,\eta) = l_{21}\eta\hat{a}_\eta \tag{A.5}$$

$$B(\xi,\eta) = l_{32}(\xi+\eta-1)\hat{a}_\xi \tag{A.6}$$

$$B(\xi,\eta) = l_{13}(\xi\hat{a}_\xi - \xi\hat{a}_\eta) \tag{A.7}$$

$$B(\xi,\eta) = l_{21}\xi\hat{a}_\xi \tag{A.8}$$

$$B(\xi,\eta) = l_{32}(-\eta\hat{a}_\xi + \eta\hat{a}_\eta) \tag{A.9}$$

$$B(\xi,\eta) = l_{13}(\xi+\eta-1)\hat{a}_\eta \tag{A.10}$$

Like RWG, these basis functions (from Equation (A.5) to (A.10)) are also defined on the pair of two triangular cell each sharing a common edge. It gives a linear normal component across the shared edge of the triangular cell.

Remaining two basis function are confined to individual cell which can be written as

$$B(\xi,\eta) = l_{32}(\xi(\xi-1)\hat{a}_\xi + \xi\eta\hat{a}_\eta) \tag{A.11}$$

$$B(\xi,\eta) = l_{13}(\xi\eta\hat{a}_\xi + \eta(\eta-1)\hat{a}_\eta) \tag{A.12}$$

These basis function (from Equation (A.11) to (A.12)) gives a zero normal component on all three edges and quadratic tangent along the two edges of the cell.

A.1.3. Transforming the basis function

The basis function in Cartesian coordinate system can be obtained by [29] [30]

$$\begin{bmatrix} B_x \\ B_y \\ B_z \end{bmatrix} = \frac{1}{D}\begin{bmatrix} \frac{dx}{d\xi} & \frac{dx}{d\eta} \\ \frac{dy}{d\xi} & \frac{dy}{d\eta} \\ \frac{dz}{d\xi} & \frac{dz}{d\eta} \end{bmatrix}\begin{bmatrix} B_\xi \\ B_\eta \end{bmatrix} \tag{A.13}$$

And, the divergence of the basis function can be written as [29] [30]

$$\nabla\cdot\mathbf{B}(x,y,z) = \frac{1}{D}\left\{\frac{dB_\xi}{d\xi} + \frac{dB_\eta}{d\eta}\right\} \tag{A.14}$$

$$D = 2 \times \text{Area of the triangular cell} \tag{A.15}$$

Where **B** is the vector basis function in Cartesian coordinate system and D is the determinant of the Jacobian matrix. All the divergence conforming basis function ensures a continuous normal component across the shared edge of the triangular cell and assigned no basis function normal to the cell edges of the boundary where the surface current vanish.

APPENDIX B

B.1. Cartesian coordinates of the center aperture positions (in cm)

Table B.1. Coordinates of the center aperture position T_j (in cm), where j = 1, 2, ..., 42, used in ANN training.

Position	Cartesian coordinates	Position	Cartesian coordinates	Position	Cartesian coordinates
T_1	(0, 7.5, 3)	T_{15}	(0, 15, 6)	T_{29}	(0, 22.5, 9)
T_2	(0, 7.5, 5)	T_{16}	(0, 15, 8)	T_{30}	(0, 4.75, 4.75)
T_3	(0, 7.5, 6)	T_{17}	(0, 15, 9)	T_{31}	(0, 4.75, 6)
T_4	(0, 7.5, 7)	T_{18}	(0, 17.5, 3)	T_{32}	(0, 4.75, 7.25)
T_5	(0, 7.5, 9)	T_{19}	(0, 17.5, 5)	T_{33}	(0, 6.8, 5.4)
T_6	(0, 10, 4)	T_{20}	(0, 17.5, 7)	T_{34}	(0, 6.8, 6.6)
T_7	(0, 10, 6)	T_{21}	(0, 17.5, 9)	T_{35}	(0, 8.85, 4.75)
T_8	(0, 10, 8)	T_{22}	(0, 20, 4)	T_{36}	(0, 8.85, 6)
T_9	(0, 12.5, 3)	T_{23}	(0, 20, 6)	T_{37}	(0, 8.85, 7.25)
T_{10}	(0, 12.5, 5)	T_{24}	(0, 20, 8)	T_{38}	(0, 10.9, 5.4)
T_{11}	(0, 12.5, 7)	T_{25}	(0, 22.5, 3)	T_{39}	(0, 10.9, 6.6)
T_{12}	(0, 12.5, 9)	T_{26}	(0, 22.5, 5)	T_{40}	(0, 12.95, 4.75)
T_{13}	(0, 15, 3)	T_{27}	(0, 22.5, 6)	T_{41}	(0, 12.95, 6)
T_{14}	(0, 15, 4)	T_{28}	(0, 22.5, 7)	T_{42}	(0, 12.95, 7.25)

Table B.2. Coordinates of the center aperture position T_j (in cm), where j = 43, 44, ..., 105, used in ANN training.

Position	Cartesian coordinates	Position	Cartesian coordinates	Position	Cartesian coordinates
T_{43}	(0, 15, 4.75)	T_{64}	(0, 10, 4.5)	T_{85}	(0, 20, 10.5)
T_{44}	(0, 15, 7.25)	T_{65}	(0, 10, 7.5)	T_{86}	(0, 22.5, 1.5)
T_{45}	(0, 17.05, 4.75)	T_{66}	(0, 10, 9)	T_{87}	(0, 22.5, 4.5)
T_{46}	(0, 17.05, 6)	T_{67}	(0, 10, 10.5)	T_{88}	(0, 22.5, 7.5)
T_{47}	(0, 17.05, 7.25)	T_{68}	(0, 12.5, 1.5)	T_{89}	(0, 22.5, 10.5)
T_{48}	(0, 19.1, 5.4)	T_{69}	(0, 12.5, 4.5)	T_{90}	(0, 3.35, 3.35)
T_{49}	(0, 19.1, 6.6)	T_{70}	(0, 12.5, 6)	T_{91}	(0, 3.35, 4.67)
T_{50}	(0, 21.15, 4.75)	T_{71}	(0, 12.5, 7.5)	T_{92}	(0, 3.35, 6)
T_{51}	(0, 21.15, 6)	T_{72}	(0, 12.5, 10.5)	T_{93}	(0, 3.35, 7.33)
T_{52}	(0, 21.15, 7.25)	T_{73}	(0, 15, 1.5)	T_{94}	(0, 3.35, 8.65)
T_{53}	(0, 23.2, 5.4)	T_{74}	(0, 15, 10.5)	T_{95}	(0, 5.68, 3.35)
T_{54}	(0, 23.2, 6.6)	T_{75}	(0, 17.5, 1.5)	T_{96}	(0, 5.68, 5.12)
T_{55}	(0, 25.25, 4.75)	T_{76}	(0, 17.5, 4.5)	T_{97}	(0, 5.68, 6.88)
T_{56}	(0, 25.25, 6)	T_{77}	(0, 17.5, 6)	T_{98}	(0, 5.68, 8.65)
T_{57}	(0, 25.25, 7.25)	T_{78}	(0, 17.5, 7.5)	T_{99}	(0, 8.01, 3.35)
T_{58}	(0, 7.5, 1.5)	T_{79}	(0, 17.5, 10.5)	T_{100}	(0, 8.01, 5.12)
T_{59}	(0, 7.5, 4.5)	T_{80}	(0, 20, 1.5)	T_{101}	(0, 8.01, 6.88)
T_{60}	(0, 7.5, 7.5)	T_{81}	(0, 20, 3)	T_{102}	(0, 8.01, 8.65)
T_{61}	(0, 7.5, 10.5)	T_{82}	(0, 20, 4.5)	T_{103}	(0, 10.34, 3.35)
T_{62}	(0, 10, 1.5)	T_{83}	(0, 20, 7.5)	T_{104}	(0, 10.34, 5.12)
T_{63}	(0, 10, 3)	T_{84}	(0, 20, 9)	T_{105}	(0, 10.34, 6.88)

Table B.3. Coordinates of the center aperture position T_j (in cm), where j = 106, 107, 108, ..., 135, used in ANN training.

Position	Cartesian coordinates	Position	Cartesian coordinates	Position	Cartesian coordinates
T_{106}	(0, 10.34, 8.65)	T_{116}	(0, 17.33, 5.12)	T_{126}	(0, 21.99, 8.65)
T_{107}	(0, 12.67, 3.35)	T_{117}	(0, 17.33, 6.88)	T_{127}	(0, 24.32, 3.35)
T_{108}	(0, 12.67, 5.12)	T_{118}	(0, 17.33, 8.65)	T_{128}	(0, 24.32, 5.12)
T_{109}	(0, 12.67, 6.88)	T_{119}	(0, 19.66, 3.35)	T_{129}	(0, 24.32, 6.88)
T_{110}	(0, 12.67, 8.65)	T_{120}	(0, 19.66, 5.12)	T_{130}	(0, 24.32, 8.65)
T_{111}	(0, 15, 3.35)	T_{121}	(0, 19.66, 6.88)	T_{131}	(0, 26.65, 3.35)
T_{112}	(0, 15, 4.67)	T_{122}	(0, 19.66, 8.65)	T_{132}	(0, 26.65, 4.67)
T_{113}	(0, 15, 7.33)	T_{123}	(0, 21.99, 3.35)	T_{133}	(0, 26.65, 6)
T_{114}	(0, 15, 8.65)	T_{124}	(0, 21.99, 5.12)	T_{134}	(0, 26.65, 7.33)
T_{115}	(0, 17.33, 3.35)	T_{125}	(0, 21.99, 6.88)	T_{135}	(0, 26.65, 8.65)

Table B.4. Coordinates of the center aperture position used for validating the results of ANN against that of numerical simulation.

Position	Cartesian coordinates	Position	Cartesian coordinates
A_1	(0, 11.2, 7.5)	A_6	(0, 16.2, 2.7)
A_2	(0, 18.7, 5)	A_7	(0, 21.3, 9)
A_3	(0, 9.87, 6)	A_8	(0, 6.84, 4.24)
A_4	(0, 22.17, 6)	A_9	(0, 6.84, 7.76)
A_5	(0, 13.8, 9.3)	A_{10}	(0, 20.82, 6)

VITA

Rahul Bakore

Candidate for the Degree of

Doctor of Philosophy

Thesis: ANALYSIS AND VALIDATION OF THE FIELD COUPLED THROUGH AN APERTURE IN AN AVIONICS ENCLOSURE

Major Field: Electrical Engineering

Biographical:

Education:

Completed the requirements for the Doctor of Philosophy in Electrical Engineering at Oklahoma State University, Stillwater, Oklahoma in May, 2017.

Completed the requirements for the Master of Science in Electrical Engineering at Oklahoma State University, Stillwater, Oklahoma in 2012.

Completed the requirements for the Bachelor of Science in Electronics and Communication Engineering at University of Rajasthan, Jaipur, India in 2008.

Experience:

Teaching Assistant, Oklahoma State University, January 2013 – December 2016

Research Assistant at REFTAS Laboratory, Oklahoma State University, January 2015 - December 2016.

Instructor of Record, Oklahoma State University, August 2014 – December 2014.

Research Assistant at Mixed Signal VLSI Design Group, Oklahoma State University, April 2012 - August 2012.

Professional Memberships:

IEEE Student Member.
Member of Golden Key International Honor society.